Study of MOCVD grown AlGaAs/GaAs (100) spontaneous superlattice and its application for optoelectronic devices

By

ANWAY PRADHAN
Enrolment No- PHYS05201404003

Saha Institute of Nuclear Physics, Kolkata

A thesis submitted to the

Board of Studies in Physical Sciences

In partial fulfillment of requirements

for the Degree of

DOCTOR OF PHILOSOPHY

of

HOMI BHABHA NATIONAL INSTITUTE

February, 2020

Homi Bhabha National Institute[1]
Recommendations of the Viva Voce Committee

As members of the Viva Voce Committee, we certify that we have read the dissertation prepared by Anway Pradhan entitled "Study of MOCVD grown AlGaAs/GaAs (100) spontaneous superlattice and its application for optoelectronic devices" and recommend that it may be accepted as fulfilling the thesis requirement for the award of Degree of Doctor of Philosophy.

Chairman -Name & Signature with date
(Ex-Head, SPMS Division, SINP)
Prof. Satyaranjan Bhattacharyya. Email: satyar.bhattacharyya@saha.ac.in

Guide / Convener - Name & Signature with date
Prof. Satyaban Bhunia. SINP, Email: Satyaban.bhunia@saha.ac.in 14.07.2020

Co-guide - Name & Signature with date (if any)

Examiner - Name & Signature with date
Prof. K G Suresh, IIT Bombay. Email: suresh@phy.iitb.ac.in

Member 1- Name & Signature with date
Prof. Chandan Mazumdar. SINP, Email: chandan.mazumdar@saha.ac.in

Member 2- Name & Signature with date
Prof. Krishnakumar S. R. Menon. SINP, Email: krishna.menon@saha.ac.in

Member 3- Name & Signature with date
Dr. Paramita Mukherjee. VECC, Email: paramita@vecc.gov.in

Final approval and acceptance of this thesis is contingent upon the candidate's submission of the final copies of the thesis to HBNI.

I/We hereby certify that I/we have read this thesis prepared under my/our direction and recommend that it may be accepted as fulfilling the thesis requirement.

Date: 14.07.2020
Place: Kolkata

Signature
Co-guide (if any)

Signature
Guide

---

[1] This page is to be included only for final submission after successful completion of viva voce.

Subject: Report of PhD Defence seminar of Mr. Anway Pradhan
From: satya.bhattacharyya@saha.ac.in
Date: 27-Jul-20, 9:42 PM
To: satyaban.bhunia@saha.ac.in

To
Prof. Satyaban Bhunia
Saha Institute of Nuclear Physics, Kolkata

Dear Prof. Bhunia,

I was present in the PhD seminar talk entitled "Study of MOCVD grown AIGaAs/GaAs (100) spontaneous superlattice and its application for optoelectronic devices" delivered by Mr. Anway Pradhan, one of your PhD students, held on 14th July, 2020 in the google meet where a large number of experts and students were present.

Mr. Anway Pradhan explained the basic Physics of his findings in a very lucid way and his deliberation was very much informative and enjoyable. He carried out extensive works quite sufficient for a PhD thesis. He was asked a number of questions and queries by experts, faculties and students and he answered them quite satisfactorily. I was very happy with his presentation and answers to the questions.

I have also seen his progress of work in the capacity of the Chairman of his doctoral committee for the last few years and am well acquainted with his scientific exploration, understanding and research output.

Considering his high standard of research works, publications and presentation, I strongly recommend the acceptance of his PhD thesis for the award of PhD degree in his favour.

With best regards,
Satyaranjan Bhattacharyya.

Dr. Satyaranjan Bhattacharyya
Senior Professor H
Surface Physics & Materials Science Division
Saha Institute of Nuclear Physics
1/AF Bidhan Nagar, Kolkata 700064, India
Tel: +91-33-23375345 (to -49) (Ext. 4217, 4610)
FAX: +91-33-23374637
email: satya.bhattacharyya@gmail.com

Subject: Re: Thesis recommendation and report
From: suresh@phy.iitb.ac.in
Date: 25-Jul-20, 7:54 PM
To: "Satyaban Bhunia" <satyaban.bhunia@saha.ac.in>

Dear Prof. Bhunia:

In addition to the report sent earlier, I would like to mention the following about the work by Anway.

His thesis reported on the study of certain semiconductor nano-structures. This is a very important field of study in condensed matter physics in general and nanomaterials in particular and the findings are very significant. The candidate has been quite successful in achieving the targets, which were by no means easy to realize. The work has been carried out with utmost care and with the help of all necessary experimental tools and theoretical models. The data have been collected very systematically and the analysis done very meticulously. I appreciate the style of presentation of the thesis, which gives a clear picture of the complexity of the problem and the way it was addressed. The thesis is presented well with good details of introduction, literature survey and experimental techniques. The presentation of figures, sketches, graphs etc. has been really good. I am very happy to see that you have been quite successful in getting a very good piece of a very difficult implemented by the students. Therefore, I congratulate both of you and I am sure that many more such high impact contributions will come out of your group in the near future. I particularly like your interest in getting into the devices, thereby fully utilizing the understanding obtained from the study for real applications.

with best regards

suresh

> On 23-Jul-20 7:02 PM, suresh@phy.iitb.ac.in wrote:
>
> > attached.
> > Hope this will do.
> >
> > best regards
> >
> > suresh
> >
> > > Dear Suresh,
> > >
> > > Hope you are fine and I thank you again for being examiner of Ph.D. viva-voce of Anway. Now I request you to kindly send a feedback form which is necessary to complete the process. In normal circumstances, a form (attached herewith) is signed by all present during the viva-voce and a report is generated.
> > >
> > > While sending your feedback and recommendation, you may touch upon the following points.
> > >
> > > <1. Your feeling about being the thesis examiner of the student, his

> > > compliance report with your questionnaire on thesis>
> > >
> > > <2. Your feeling about becoming an external expert on his Ph.D.
> > > Viva-voce exam, that through a video conferencing mode>
> > >
> > > <3. Your evaluation of the viva-voce exam, and your recommendation
> > > whether the thesis can be accepted and the student be awarded the
> > > degree>
> > >
> > > With best regards,
> > >
> > > Satyaban
> > >
> > > --
> > > Dr. Satyaban Bhunia
> > > Professor
> > > Surface Physics and Material Science Division
> > > Saha Institute of Nuclear Physics
> > > 1/AF, Bidhannagar
> > > Kolkata - 700064
> > > Ph: +91 33 2337 5345 to 9 (5 lines) extn. 3320, 1226
> > > FAX: +91 33 2337 4637
>
> --
> Dr. Satyaban Bhunia
> Professor
> Surface Physics and Material Science Division
> Saha Institute of Nuclear Physics
> 1/AF, Bidhannagar
> Kolkata - 700064
> Ph: +91 33 2337 5345 to 9 (5 lines) extn. 3320, 1226
> FAX: +91 33 2337 4637

--
Dr. K. G. Suresh   Email:suresh@phy.iitb.ac.in
Professor   suresh@iitb.ac.in
Dept. of Physics   suresh.k.gopi@gmail.com
IIT Bombay   Phone: (O)+91-22-25767559
Mumbai 400 076   (H)+91-22-25768559
India   (Cell): 9869649706

Subject: Report on the PhD Defence seminar of Mr. Anway Pradhan
From: chandan.mazumdar@saha.ac.in
Date: 29-Jul-20, 12:47 AM
To: "Satyaban Bhunia" <satyaban.bhunia@saha.ac.in>

To
Prof. Satyaban Bhunia
Surface Physics and Material Science Division
Saha Institute of Nuclear Physics, Kolkata 700064

Dear Prof. Bhunia,

Below, please find my report on the PhD Defence seminar of Mr. Anway Pradhan

----

Mr. Anway Pradhan has presented his Ph.D thesis talk on the "Study of MOCVD grown AIGaAs/GaAs (100) spontaneous superlattice and its application foroptoelectronic devices" on 14th July, 2020. His mode of presentation was quite informative and bear the stamp of his authority and grasp on the subject. He has described the aim of his research and the final outcome of his work. He had answered all the questions effortlessly and was very much to the point. He also has quite a few good quality publications concerning his research work. His work is of very high standard, and as a member of his doctoral committee during last couple of years, I am quite knowledgeable about his gradual progress. Considering the high standard of research that he has presented and also his interaction with the audience during the question-answer season, I have no hesitation in recommending him for the award of Ph.D degree.

With best regards
Chandan Mazumdar

Professor, Condensed Matter Physics Division
Saha Institute of Nuclear Physics, Kolkata 700064

Subject: Report of Anway Pradhan
From: "Dr. Krishnakumar S. R. Menon" <krishna.menon@saha.ac.in>
Date: 07-Aug-20, 2:21 PM
To: satyaban.bhunia@saha.ac.in

Dear Prof. Bhunia,

This is to inform you that I was personally present in the PhD seminar talk entitled "Study of MOCVD grown AIGaAs/GaAs (100) spontaneous superlattice and its application for optoelectronic devices" delivered by Mr Anway Pradhan, held on 14th July 2020 in the google meet. I was impressed by his presentation and talk as he explained the basic Physics of his findings in a very lucid way. I think the amount of work, both in quality and quantity is quite sufficient for a PhD thesis. He was asked a number of questions and queries by experts, faculties and students and he answered to all of them satisfactorily. I was very happy with his presentation and answers.

I have also seen his progress of work in the capacity of a member of his doctoral committee for the last few years and am well acquainted with his scientific exploration, understanding and research output. Considering all these aspects and his journal publications, I strongly recommend the acceptance of his PhD thesis for the award of the PhD degree in his favour.

With best regards,

Krishnakumar Menon

****
Dr. Krishnakumar S. R. Menon
Professor-G,
Surface Physics & Material Science Division,
Saha Institute of Nuclear Physics,
1/AF, Bidhannagar,
Kolkata 700 064, INDIA.

Phone : +91 33 2337 5345-49 Ext. 3326
Fax : +91 33 2337 4637

e-mail: krishna.menon@saha.ac.in
****

Subject: Comments on Final PhD Viva Voce Examination for Shri Anway Pradhan
From: Paramita Mukherjee <paramita@vecc.gov.in>
Date: 30-Jul-20, 9:25 AM
To: satyaban.bhunia@saha.ac.in

Dear Dr. Bhunia,

I was present in the PhD seminar talk entitled " **Study of MOCVD grown AlGaAs/GaAs (100) spontaneous superlattice and its application for optoelectronic devices** " delivered by Shri **Anway Pradhan** , one of your PhD students, held on 14th July, 2020 in the google meet where many students and experts of the field were present.
Anway Pradahan has done a detail study on AlGaAs epilayer on (100) GaAs substrate which was grown on (100) GaAs substrate by MOCVD technique. He has used detailed characterisation techniques like low angle X-ray reflectivity (XRR) and high angle X-ray diffraction (XRD) to extract the composition and lattice parameter profile. He has also developed an MSM photodetector device based on the superlattice structures and showed an enhancement in performance, with respect to spectral and temporal response.
He has given a detailed and systematic presentation of his work in the viva voce examination. The work carried out by him is quite exhaustive and is converging to a particular goal. He has also published quite good number of publications in the peer reviewed journal. He has also answered the queries satisfactorily. Based on the quality of the thesis and also on the performance of Shri **Anway Pradhan** during Viva Voce examination**,** I , as a member of Doctoral Committee, strongly recommend the acceptance of PhD thesis for the award of PhD for him.

According to me, Video conferencing has helped to reduce the time of arranging PhD viva voce particularly for external members/examiners.
Best regards,

Paramita

डॉ.(श्रीमती) पारोमिता मुखर्जी/Dr.(Mrs) Paramita Mukherjee
प्रमुख, एम एस एस डी/Head, Materials Science Studies Division
Scientific officer H
भौतिकी समूह/Physics Group
वेरिएबल एनर्जी साइक्लोट्रॉन सेन्टर/Variable Energy Cyclotron Centre 1/ए एफ बिधाननगर/ 1/AF Bidhannagar,
कोलकाता/Kolkata-700064
Phone: 91 33 2318 2220
Fax. 91 33 2334 6871

STATEMENT BY AUTHOR

This dissertation has been submitted in partial fulfillment of requirements for an advanced degree at Homi Bhabha National Institute (HBNI) and is deposited in the Library to be made available to borrowers under rules of the HBNI.

Brief quotations from this dissertation are allowable without special permission, provided that accurate acknowledgement of source is made. Requests for permission for extended quotation from or reproduction of this manuscript in whole or in part may be granted by the Competent Authority of HBNI when in his or her judgment the proposed use of the material is in the interests of scholarship. In all other instances, however, permission must be obtained from the author.

Anway Pradhan

Anway Pradhan
Name & Signature
of the student

DECLARATION

I, hereby declare that the investigation presented in the thesis has been carried out by me. The work is original and has not been submitted earlier as a whole or in part for a degree / diploma at this or any other Institution / University.

Anway Pradhan

Anway Pradhan
Name & Signature
of the student

List of Publications arising from the thesis

Journal

1. "Spontaneous superlattice structures in $Al_xGa_{1-x}As/GaAs$ (100) grown by metalorganic vapor phase epitaxy", A. Pradhan, T. Maitra, S. Mukherjee, S. Mukherjee, A. Nayak, B. Satpati, S. Bhunia, *Materials Letters,* 2017, 210, 77-79.

2. "Interface intermixing and Interdiffusion characteristics in MOVPE grown spontaneous $Al_xGa_{1-x}As/GaAs$ (100) superlattice structures using high resolution X-ray diffraction", A. Pradhan, S. Mukherjee, T. Maitra, S. Mukherjee, A. Nayak, S. Bhunia, *Superlattices and Microstructures,* 2019, 126, 193–199.

3. "Improved spectral and temporal response of MSM photodetectors fabricated on MOCVD grown spontaneous AlGaAs superlattice", A Pradhan, T. Maitra, S. Mukherjee, S. Mukherjee, A. Nayak, and S. Bhunia, *Sensors and Actuators A: Physical,* 2019, 297, 111548-1-9.

Chapters in books and lectures notes

1.

2.

Conferences

1. "Observation of natural superlattice in $Al_xGa_{1-x}As$ layers grown by metalorganic vapor phase epitaxy". A. Pradhan, T. Maitra, S. Mukherjee, S. Mukherjee, A. Nayak, B. Satpati, and S. Bhunia, *AIP Conf. Proc.* 2016, 1728, 020243-1-6.

2. "Study of thermal stability of spontaneously grown superlattice structures by metalorganic vapor phase epitaxy in $Al_xGa_{1-x}As/GaAs$ heterostructure", A. Pradhan, T. Maitra, S. Mukherjee, S. Mukherjee, B. Satpati, A. Nayak, and S. Bhunia, *AIP Conf. Proc.,* 2018, 1942, 080038-1-4.

Others

Anway Pradhan

Anway Pradhan

Name & Signature

of the student

DEDICATIONS

To the memory of my maternal grandmother

“Late Ilarani Sareswari”

Acknowledgments

It's an honor for me to express my gratitude to the persons, who enriched the journey for these long five and a half years with their invaluable support. I apologize if I forget to mention anyone at this moment.

Firstly, I would like to acknowledge my supervisor Prof. Satyaban Bhunia for the continuous support of my Ph.D. study and related research. His guidance helped me in all the time of research and writing of this thesis. I would also like to acknowledge Prof. Arabinda Nayak for his contributions to collaborative research work. I am thankful to all of the members of my doctoral committee Prof. Satyaranjan Bhattacharyya, Prof. Chandan Mazumdar, Prof. K. S. R. Menon, Prof. Paramita Mukherjee for their support during this tenure. I would like to acknowledge Prof. M. K. Sanyal and Prof. M. K. Mukhopadhyay, and Dr. Arpan Bhattacharya regarding their contributions related to X-ray scattering, and Dr. Biswarup Satpati for TEM measurements.

I would like to acknowledge my family members and Manisha for being and bearing with me all the time. I would like to acknowledge Suman, Tamaghna, Sukhendu for their continuous support inside and outside the lab, being together as a family. I am thankful to my friends Aritra, Abhishek, Samrat, Shamik, Satyajit, Chayan for always being with me. I would like to thank Arghya, Gourab, Mantu for their enthusiastic and cheerful company at SINP. I thank my Post MSc batch mates for the time we have spent together. All the faculty members, the staff members and research fellows of the SPMS division are acknowledged. I want to thank the staff of Meghnad Saha Abasan-2 especially Shaymal da, Bishu da, Sanjib da. The SINP library staff members are also acknowledged for their support whenever needed.

Contents

List of figures

List of tables

Chapter 7

Conclusion

7.1 Summary of the work

The results of the work we have done so far through this tenure have been covered mainly in chapters 4, 5 and 6 of the thesis. In this work, we have concentrated on the natural superlattice ordering, its thermal stability, and the utilization of it in device fabrication, for the particular Al compositions of 0.3 and 0.15. As our idea was to utilize the material for the optoelectronic application, we look for the material with a direct bandgap. We have concentrated to grow AlGaAs with nominal Al content below 0.4 not only for the direct bandgap but also for the negligible lattice strain looking at the suitability of the material for optoelectronic device application. We have grown GaAs/AlGaAs MQW structures on GaAs (100) substrate for optoelectronic device applications using MOCVD technique [28]. We had observed a periodic compositional modulation in the AlGaAs barrier layer with a nominal Al fraction of 0.3 whose repetition length was about 5.4 nm, i.e., nearly around 20 monolayers of the material. To confirm the occurrence of such structures in the bulk, we have grown about 1132 nm thick AlGaAs epilayer with a targeted Al fraction of 0.15 on the conventional (100) GaAs substrate. Similar type of superlattice ordering was found in the bulk epilayer from TEM and X-ray analyses. The TEM and X-ray results were matched to confirm the periodicity. X-ray results were used to get the electron density and lattice parameter profile of the superlattice structure. Finally, we obtained the in-depth profile of composition through a combinatorial approach involving low angle XRR and high angle (004) XRD simulations. So, in the regime of our interest, the stability of ordering has been investigated for a low concentration as well as a high concentration under the similar growth conditions. Then we looked for the structural stability of such natural superlattice ordering for device application. We have studied the stability under thermal treatment by heating the as-grown sample up to a temperature of 900 ^{o}C. For temperature till 800 ^{o}C, the structures remained stable and showed a transformation into the disordered phase retaining its crystallinity intact at 900 °C of annealing, as confirmed by the high temperature (004) XRD measurements. Since the interface between the superlattice layers always plays an important role in the device characteristics, thermal diffusion in the spontaneously grown ultra-nanoscale ordered structures has been studied in detail. In absence of suitable direct experimental tools due to the physical resolution limit, we relied on the theoretical analysis of x-ray diffraction simulations coupled with a virtual diffusion experiment to arrive at the interdiffusion characteristics across the interfaces of spontaneously grown $Al_xGa_{1-x}As/Al_yGa_{1-y}As$ superlattice structures. The simulation approach presented here is a combination of an interdiffusion code and a code on x-ray diffraction around the (004) Bragg peak based on Born approximation. We have obtained the variation in the actual diffusion coefficient as a function of time at different temperatures from the decay rates of the integrated intensity of the first order satellite peak. We found the diffusion coefficient across the interface to be highly nonlinear and also composition dependent. The satellite decay equation could fit the experimental data taking the maximum Al composition alone at each time step. The pre exponential factor (D^o) and the activation enthalpy (H) values for interdiffusion were found out to be 0.17-0.25 cm^2/s and 0.5-0.6 eV for Al diffusion whereas 0.01-0.11 cm^2/s and 3.45-3.5 eV for Ga diffusion, respectively in the studied temperature range of 500 °C to 700 °C. The interdiffusivity increased with temperature from 500 °C to 625 °C and decreased for further rise in temperature as the compositional contrast between the two layers decreased significantly (reached a certain critical value) at higher temperatures. After studying the fundamental properties of the structures, we studied the effect of the natural superlattice ordering in such length scale on the optical and electrical properties of the material. Our aim was a systematic investigation of the effect of annealing on the microscopic structures of the spontaneous superlattice and also the optical properties and the device performance and to establish the correlation between the structural and the optical and electrical properties of the natural superlattice ordering. Besides, at the same time, we have done a comparative study using the ordered and thermally annealed disordered sample to understand the effect of the superlattice ordering on the optical and electrical properties of the material. Normally, high-temperature annealing can significantly modify the morphology of the materials and defects may be incorporated unintentionally. Keeping such possibilities in mind, we have examined the as-grown and the annealed samples through SEM, XTEM and XRD measurements to comment on their structural quality. The structural analyses for the as-grown and the annealed samples have shown no significant evidence of the surface damage, degradation of the crystalline quality or incorporation of unnecessary defects. Therefore, the modified optical and electrical characteristics could solely be attributed to the natural superlattice ordering. Temperature dependent photoluminescence showed a redshift of 34 meV in the transition energy for the ordered structures with respect to the bulk material with the same composition, due to repulsion between the states in valance and conduction band as a result of the overlap of k-points for the increased periodicity of the crystal lattice in real space. The bandgap reduction as a result of ordering was found to be very similar to the case of atomic ordering reported previously in different compound semiconductor materials during epitaxial growth from vapor phase [173]. The decay of photoluminescence intensities with temperature were fitted with the modified Arrhenius equation for both the samples. The two excitonic binding energies come out to be 9.87, 43.09 and 5.07, 35.36 meV for the As-grown and the annealed samples, respectively. Two binding energies suggest activation of the excitons through two different channels at lower and higher temperature regions. The higher values of the binding energy in case of the ordered sample is basically showing the effect of confinement of the carriers in the superlattice layers which enhances the stability of the excitons in the superlattice channels as compared to the disordered sample. As a part of device application, we developed photodetector for working in the NIR regime of the electromagnetic spectrum, based on the spontaneously grown superlattice structures. In general, MSM PDs have two comb-like electrodes with 1 μm spacing. In the absence of photolithographic technique in our laboratory to form such electrodes, we have concentrated on the fabrication of co-planar metal-semiconductor-metal back to back Schottky diode photodetector with natural superlattice ordering in the active semiconductor layer, due to its geometrical simplicity and high response. For comparison on the basis of the device performance regarding the spectral and temporal response, we developed other devices with the same geometry of the contacts with the 700 ^{o}C annealed superlattice and also 900 ^{o}C homogeneous AlGaAs as the active layer. Device parameters were extracted using electrical equivalent Schottky diode model using an extra diode representing the superlattice layer. By employing Lambert W function for fitting the experimental I-V measurements with the help of the diode models, we evaluated three figures of merit such as responsivity, detectivity and sensivity for all the devices. In this dissertation, for fitting of the experimentally obtained data with the calculated ones using several theoretical models as discussed in the respective sections, we have employed standard nonlinear curve fitting algorithm and found the $\chi 2$ value reliable within 1%, which seems very much appreciable. The extracted parameters, most importantly, the Schottky barrier heights showed the reason for the device based on the superlattice structures to perform better. Under a forward applied voltage of 1 V, the peak values of responsivity, detectivity and sensitivity were 10.13 mA/W, 7.6×10^{11} cmHz$^{1/2}$W^{-1}, 81.06 cm^{2}/W and 1.14 mA/W, 7.05×10^{10} cmHz$^{1/2}$W^{-1}, 2.82 cm^{2}/W for the device based on the as-grown natural superlattice and homogeneous AlGaAs, respectively. Furthermore, the as-grown device also showed superiority in the temporal response also with the application of a pulsed optical signal. The device with natural superlattice ordering showed much faster response to the square wave pulsed light with rise and decay time of 560 μs and 1 ms as compared to 2 and 7 ms, respectively, for the device with homogeneous AlGaAs. The superior spectral and temporal characteristics of the devices are explained by the model based on a third diode representing the net effect due to the superlattice modulations along with two Schottky diodes at the metal-semiconductor junctions. The third barrier, which is basically due to the periodic modulation in aluminium composition, plays a vital role in enhancement of the photocurrent as a result of the activation of superlattice channels under light while keeping the dark current small by blocking the carriers without light. The fast sweeping of the photo-carries by the intrinsic small but effective electric field at the compositionally modulated interfaces in the active semiconducting layer makes the characteristic times of the device much smaller than one with homogeneous AlGaAs. Degradation in photoresponse and speed is attributed to decrease in the compositional contrast and the increase in the interfacial width due to the interdiffusion as an effect of thermal annealing. Besides, a range of wavelength for photodetection could be covered by using the superlattice structures annealed at different temperatures, with reasonable efficiency also. A comparative study shows that our device could be a simple but effective one because of the spontaneously formed superlattice layers. The AlGaAs photodetector based on the natural superlattice has the potential to complete the available devices with different materials for Vis-NIR photodetection.

7.2 Conclusion and future outlook

Spontaneous ordering in AlGaAs in such multiple monolayer length scale was observed on conventional (100) GaAs substrate grown by MOCVD in the barrier layer of MQW and bulk material despite the small bond length difference between the constituent binaries. The well observed and previously reported CuAu type monolayer ordering could be explained by the surface reconstruction to minimize the surface free energy. Although the origin of the of the ordering is not very clear at the present time, the existence of such spontaneously grown structures in the bulk material could depend on the surface thermodynamics for the formation, whereas the growth temperature inside the reactor and the growth rate decided the stability of the ordering inside the bulk. Since we have observed such a new kind of partial ordering in AlGaAs on the conventional GaAs substrates, the existence of the structures could be studied with various growth parameters like growth temperature, substrate orientation and flow rate for better understanding the origin and nature and stability of such ordering in future. It will be interesting to study how the atomically ordered layers can be changed to layers with random alloying with homogeneous concentration throughout by changing the growth parameters, and also whether there is a limit of nominal Al content to form such ordering in the full composition range of our interest. Furthermore, it would be interesting to study whether such natural superlattice ordering could form with other elements also for some particular growth condition such as flow rates of the precursors, temperature, substrate orientation etc. MOCVD, being a vapor phase epitaxial technique, has always an important role in the formation of such ordered structures and stabilize it well inside the material. It might be possible that such ordering could also form during the MBE growth but that needs further study. As the structure showed reduction in the bandgap similar to the case of monolayer ordering, the structure could be used to develop quantum heterostructures such as quantum well by growing order and disorder phase sequentially on the same material, just changing the growth parameters. The stability of such structures after thermal treatment is very important as most device applications need high temperature treatment. We have developed a model to thoroughly study the inter-diffusion characteristics in superlattice structures by employing high temperature X-ray scattering. We deduced the behavior of the diffusion coefficient at five different temperatures and showed concentration dependence of the diffusion coefficient in the material. The model can also be used to explain the interdiffusion process in various artificial superlattice structures of different length scales. Photoluminescence can also be employed to extract the interdiffusion characteristics as it shows significant modification in the transition energy. Then, the results from the XRD and PL can be compared in regard to the diffusion in the natural superlattice. The optical characteristics of the natural superlattice has also revealed a significant enhancement in the intensity of the transition. The intensity of the photoluminescence which depends on the carrier density and the radiative recombination rate depends on the degree of ordering. Theoretical background of the enhancement of the photoluminescence intensity i.e. the optical gain as an effect of ordering is still an open field for research. The polarization dependence of the emitted radiation for such newly observed natural ordering could also be interesting to study. The effect of ordering on the carrier concentration due to the zone folding and consequent splitting of the band energy can also be investigated in the future. From the device perspective, the implication of the superlattice structures in the metal-semiconductor-metal photodetector device showed a betterment in the device performance. The main advantage is that the natural superlattice constrained the dark current through the heterointerfacial barriers between the compositionally modulated structures, and on the other hand enhanced the overall gain by increasing the photocurrent through the activation of the superlattice parallel channels for the photogenerated carriers in presence of light. The response speed of the device also showed superiority by getting influenced due to the development of the intrinsic electric field at the heterointerfaces. The superlattice and such ordered-disordered structures mentioned above could also be used in various optoelectronic devices such as intermediate band solar cells, broad band photodetectors, quantum cascade lasers due to its better optical and electrical quality relative to bulk.

Summary

We observed a spontaneous superlattice ordering due to periodic compositional modulation in the AlGaAs barrier layer with nominal Al fraction of 0.3 of GaAs/AlGaAs multi-quantum well (MQW) structure grown by MOCVD. We have obtained the repetition length of 5.4 nm, which is nearly around 20 monolayers of the material. Observation of the similar type of natural superlattice ordering in an 1132 nm thick AlGaAs epilayer confirms the occurrence and stability of such spontaneous periodic compositional modulation in the bulk also. Spontaneous ordering in such multiple monolayer length scale was observed in AlGaAs, for different Al fractions, on conventional (100) GaAs substrate, in MQW and bulk material, despite the small bond length difference between the constituent binaries. Both low angle X-ray reflectivity (XRR) and high angle X-ray diffraction (XRD) showed equispaced, distinct and sharp satellite peaks as a signature of the modulated periodic structures. XRD scan shows the symmetrically positioned superlattice peaks around the central (004) Bragg peak. The similar measurement for (002) planes, which is quasi-forbidden for Bragg reflections showed only superlattice peaks with the zeroth order peak being at the center. The structures were analyzed rigorously through a combination of low angle reflectivity and high angle Bragg diffraction measurements. The combinatorial approach of simulation of the XRR and XRD data was employed using the distorted-wave Born approximation (DWBA) formalism and kinematical model of X-ray scattering, respectively, to extract the depth profile of the modulated composition. Thermal diffusion characteristics in the spontaneously grown ultra-nanoscale ordered structures have been studied in details. In absence of suitable direct experimental tools due to the physical resolution limit, we relied on the theoretical analysis of XRD simulations based on Born approximation coupled with the virtual diffusion experiment to arrive at the distortion in the lattice parameter profile and finally, diffusion characteristics across the interfaces of the spontaneously grown AlGaAs/AlGaAs superlattice structures from the decay rates of the integrated satellite peak intensities. We have found the diffusion coefficient across the interface to be highly nonlinear and concentration dependent. The analysis has shown that the satellite decay equation could fit the experimental data taking the maximum Al composition alone at each time step. The extracted interdiffusivity increases with temperature from 500 °C to 625 °C and decreases for further rise in temperature as the compositional contrast between the two layers reaches a critical value at higher temperatures beyond 625 °C. A significant difference in the activation enthalpy values for Al and Ga diffusion as 0.5-0.6 eV and 3.45-3.5 eV, respectively, was obtained in the temperature range 500-700 °C. Photoluminescence spectroscopy showed a redshift of 34 meV in the transition energy for the ordered structures with respect to the bulk material with the same composition due to the increase in lattice periodicity. The higher binding energy of the excitons for the former one could be attributed to the confinement of the carriers in the superlattice structures. We have fabricated co-planar metal-semiconductor-metal Schottky diode photodetector using the as-grown natural superlattice, 700 °C annealed distorted superlattice and homogeneous AlGaAs to investigate both the spectral and temporal response of the devices. Under a forward bias of 1 V, maximum value of responsivity, detectivity and sensitivity, 10.133 mA/W, 7.6×10^{11} cmHz$^{1/2}$W^{-1}, 81.06 cm^{2}/W, and a fast response time of 560 μs, were obtained for the device based on the superlattice structures. Activation of the superlattice channels for the carriers in presence of light enhanced the responsivilty while the detectivity being increased at the same time by limiting the dark current, caused due to the barriers in absence of light. The device based on the superlattice structures showed fast switching up to a relatively higher frequency which could be attributed to the intrinsic electric field due to the junctions formed between the consecutive layers.

Chapter 1

General Introduction

1.1 Introduction

Compound semiconductors have shown the potential to compete with integrated silicon technology due to the availability of direct bandgap materials applicable in a wide range of the electromagnetic spectrum [1]. Use of the compound semiconductors is advantageous because of the flexibility in the choice of materials for device fabrication. Along with the simple binary compounds, complex ternary and quaternary compounds with different concentrations can also be grown. Two different binaries with a common cation or anion can be mixed in the desired fraction to form a ternary compound whereas, a quaternary compound can be produced by mixing one ternary with a desirable amount of a binary compound. The production of compound semiconductor optoelectronic devices on a large scale needs growth of the materials in layers with fewer defects and misfit dislocations at the interface [2]. Besides, devices with low dimensional multilayer structures are required for increasing the efficiency of conversion of energy as well as the speed of transmission of information [3]. For the development of multilayer structures using compound semiconductors with fewer lattice defects, the epitaxial growth process is necessary. The epitaxial growth processes are mainly advantageous for the pseudomorphic growth of the multilayered structures with a wide range of desired thickness, high quality layered materials with abrupt interfaces, high degree of compositional uniformity and reproducibility. Besides, a wide range of electrical and optical properties can be covered by precise control over the structural parameters in various ternary or quaternary compounds. There are several epitaxial techniques such as liquid-phase epitaxy (LPE) [4], chloride vapor-phase epitaxy (ClVPE) [4], hydride vapor-phase epitaxy (HVPE) [5], highly sophisticated processes such as molecular beam epitaxy (MBE) [6], metalorganic chemical vapor deposition (MOCVD) [7] available for this purpose. Of late MBE and MOCVD have emerged with their potentials in compound semiconductor device processing.

MOCVD growth of II-VI or III-V based binary, ternary, quaternary compound material systems find the potential to replace the Si-based technology towards electronic and optoelectronic device applications [2]. In developing the GaAs based devices, AlGaAs is considered to be one of the most suitable materials in device fabrication due to its high flexibility in bandgap engineering and negligible lattice strain with respect to GaAs. AlGaAs/GaAs heterostructures are regarded as the backbone in the development of various electronic and optoelectronic applications [8,9]. As both GaAs and AlAs crystalize in Zinc-blende (ZnS) phase [10] and at the same time, having a small atomic size difference [11], the AlGaAs/GaAs material system usually does not require any special technique for the control of mechanical stresses during the growth of the conventional heterostructures. Observation of two-dimensional electron gas (2DEG) in AlGaAs-GaAs heterostructures [12], fabrication of quantum well cascade lasers due to large conduction band offset [13], increase the importance of the material system from the viewpoint of fundamental physics and application as well. The increasing interest in the material system has, in turn, led to a continuous study to improve the growing and processing methods in order to obtain high-quality quantum-well heterostructures (QWH's). Besides, various state-of-the-art low dimensional devices involving quantum cascade lasers (QCL) [13], vertical-cavity surface-emitting lasers (VCSEL) [14], quantum well-infrared photodetector (QWIP) [15], resonant tunneling diodes (RTD) [16], etc. have been demonstrated using the material system. Such devices demand a high quality of the interface, precise control over the doping concentration, formation of ultrathin layers with high repeatability and reproducibility. In all such applications, the alloy composition in the $Al_xGa_{1-x}As$ barrier layer is uniform. The ultimate performance and electronic properties of $Al_xGa_{1-x}As$/GaAs QW based devices not only depend on the quality of the GaAs well and the hetero-interface, but also on the compositional homogeneity of the barrier layer or ordering. A natural superlattice ordered structure due to periodic variation in Group-III content in the barrier layer may lead to improved optical mode confinement in the QW structures. Any random inhomogeneity, such as variation in alloy concentration or dopant fluctuations due to segregation, intermixing or diffusion can disturb structural integrity and affect device performance. The fascinating optical and electrical properties in low dimensions despite the simplicity of the system, retain its demand in research as well as device application till now [17].

A knowledge on the material properties of GaAs and AlGaAs is necessary for the understanding of the AlGaAs/GaAs heterostructures for device application. Firstly, we have to consider the lattice parameters of the end-point binary compounds. The best achieved linear relationship of the lattice parameter of the pseudo-binary compound to composition is given by, $a_x = 5.6533+0.00809x$ Å, where x is the fraction of Al in the compound [11]. In the zinc blende crystal structure, as shown in Fig. 1.1(a) of $Al_xGa_{1-x}As$ alloys, the two face-centered cubic (FCC) cation and anion sublattices are displaced by one-fourth of a body diagonal. In general, other than the random arrangement of the atoms in the group-III sublattice, there may be a preferential ordering of the atomic planes, comprised of alternative group-III atoms, along any particular direction. The structure with such ordering along <001> is shown in Fig. 1.1(b). The presence of such monolayer superlattice ordering could be observed directly from the appearance of the superstructure reflections at some of the forbidden positions along with the unmixed zinc blende Bragg reflections. The diffraction spots for the random zinc blende lattice and the additional superspots in case of the above mentioned ordered structure (also known as CuAu as first observed in the metallic alloy CuAu) in the reciprocal space are shown in Fig. 1.1(c) and (d), respectively. In reality, since all the atoms may not occupy the correct sites to define a fully random or completely ordered structure, a parameter called the degree of order, is given by

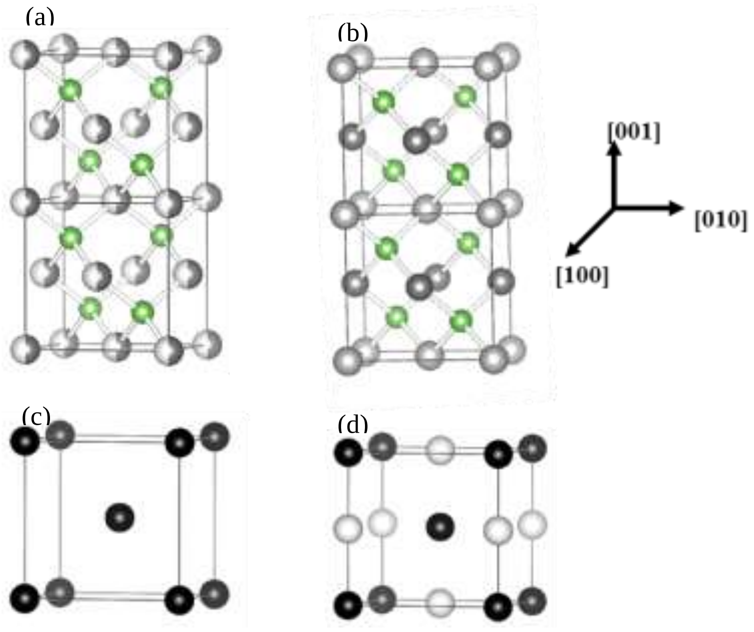

Fig. 1.1 The crystal structure of (a) random zinc blende lattice, the half shaded spheres stand for the fact that the group III site occupied by either A or B atom and (b) monolayer ordering along <001> direction, the darker spheres represent A and lighter ones, B atoms and green spheres C atoms, (c) and (d) represents the corresponding diffraction spots in the reciprocal space of the respective lattices

$$S = r_{Ga} + r_{Al} - 1 \qquad 1.1$$

Where r_{Ga} and r_{Al} are the fractions of Ga and Al atoms respectively occupying preferred sites. Thus the value of S is 1 for perfect ordering whereas S=0 for fully random arrangement. The CuAu I structure possesses P-4m2 symmetry, based on the tetragonal unit cell. The intensity of the superstructure reflection was found to vary as the square of the degree of the order [18]. Investigations on the AlGaAs system on GaAs substrates revealed that ordering could be stable for a wide range of Al concentration and growth temperature [19]. Generally, in case of such ordering, the direction of the formation of the superlattice axis is parallel to one of the crystal axes. For growth on a predefined surface, the variants with the tetragonal axis perpendicular to the growth axis would be produced [20]. Recently, we observed spontaneous superlattice type bilayer ordering in MOCVD grown AlGaAs epilayer on semi-insulating GaAs (100) substrate with a fine compositional modulation [21]. Physical properties, i.e. optical, electrical, depend upon the microstructural arrangement of atoms in the crystal. So, optical emission property, carrier mobility, band alignment, etc. are influenced strongly due to superlattice ordering. The device characteristics involving $Al_xGa_{1-x}As/GaAs$ (100) material system with such structures would also be significantly modified. The accuracy in determining the composition, strain, layer thickness, and interface are very important regarding the application of any structure. Our group has analyzed the spontaneously grown superlattice type structure by involving a combination of X-ray reflectivity and XRD based on distorted wave Born approximation (DWBA) and a kinematical model for X-ray scattering, respectively. The satellite peaks with a finite spacing which reflects the periodicity in the real lattice have been studied rigorously to understand the phenomena for spontaneous as well as artificially grown superlattice structures [22,23]. The intensity of the satellite peaks is a function of the compositional contrast in the consecutive layers and also the thickness of the individual layers. For the fabrication of several optoelectronic devices, it is necessary to have a good idea of how the superlattice behaves upon thermal treatment. The stability of the ordering at any length scale under thermal treatment depends on the rate of interdiffusion of the atoms through the interface. Previous studies on interdiffusion showed that XRD from MQW or superlattice type structures is more sensitive to interdiffusion in comparison with single quantum well structures [24]. The sensitivity of the ordered structures to X-ray has shown a new direction in the study of the order-disorder transition through X-ray analysis. It is also possible to evaluate the diffusion coefficient and the activation enthalpies for out-diffusion of the interfacial atoms by monitoring the rate of decay of the satellite peaks as a result of thermal annealing. Regarding the applicability and utility of the superlattice structures in semiconductor devices, a thorough investigation of interdiffusion and an idea of loss of order have been realized quite efficiently by the involvement of XRD in conjunction with interdiffusion. The change in the compositional contrast and the quality of the interface can be estimated from the decay of the satellite peaks as a function of anneal time as well as temperature. We have studied the interdiffusion characteristics of the natural superlattice ordering by means of high temperature real-time XRD measurements in the temperature range from 500 ^{o}C to 700 ^{o}C [25]. The temperature range has been chosen in such a way that the effect on the satellite intensity is both significant and also suitable to monitor at the same time. Our study revealed the stability of such ordering up to 800 ^{o}C temperature with certain amount of distortion in the composition profile and further rise in temperature resulted in homogenous concentration and consequently, the disappearance of the satellite peaks in the XRD pattern. We have applied a model combining interdiffusion and XRD based on kinematical simulation to extract the time evolution of diffusion in the natural superlattice structures of such low compositional contrast in such a length scale at different temperatures [25]. The study is important since interdiffusion due to annealing changes the compositional contrast and the interfacial width which affects the optical quality and device performance too. Due to the spontaneous ordering in the grown AlGaAs layer, a redshift of 34 meV in the photoluminescence signal was observed, which also showed higher binding energy obtained from Arrhenius plots. Next, we looked for the fabrication of photodetector devices using the superlattice. Metal-semiconductor-metal photodetectors are immensely studied due to its simple geometry to fabricate and the fast response of the devices [26,27]. We have developed such photodetector based on as-grown, distorted superlattice and totally disordered AlGaAs for a comparative study of the effect of annealing on ordering and consequently on the device performance [28]. For the analysis, Lambert W function was involved with a three (two) Schottky diode model for the ordered (disordered) structures. The two diodes represented the two metal contacts whereas the third diode was used as the electrical equivalent for the layer consisting of superlattice structures. The behavior of the device parameters and the figures of merit under dark and on the application of light showed the superiority of the device based on the superlattice regarding both spectral and temporal response.

Here, in the following section, I have discussed the observed spontaneous ordering in various material systems, their theoretical and experimental understanding and some of the major consequences.

1.2 Literature review

This section contains the fundamental aspects of atomic ordering observed in various material systems, their important features and the effects on their macroscopic material properties as a consequence.

1.2.1 Possible ordered structures

Instead of random arrangement of the group III atoms in a ternary compound semiconductor, say $A_xB_{1-x}C$, the atoms can take preferential positions in the lattice to form a number of ordered structures with periodicity being an integer multiple of that in the random lattice. One such ordered structure, CuAu I was shown previously in Fig.1.1. For the perfect stoichiometric compound of $A_{0.5}B_{0.5}C$, the ordered structures can be categorized into three classes depending on the direction along which the periodicity doubles. For CuPt, chalcopyrite and CuAu the ordering occurs on {111}, {210} and {001} planes, respectively [29]. Ordering like luzonite and famatinite can be possible for $A_{0.25(0.75)}B_{0.75(0.25)}C$ on {100}, {110}, {210} and {100}, {110} planes, respectively [30]. Moreover, based on these basic structures more ordered structures are always possible depending on the multiplicity of the periodicity, for example, triple period ordering (TP) with periodicity three times that of the random zinc blende lattice. CuPt, luzonite, famatinite, and chalcopyrite crystal structures are shown in Fig. 1.2(a), (b), (c) and (d), respectively [31]. The planes on which the atomic ordering takes place are also indicated in the respective figures for clarity.

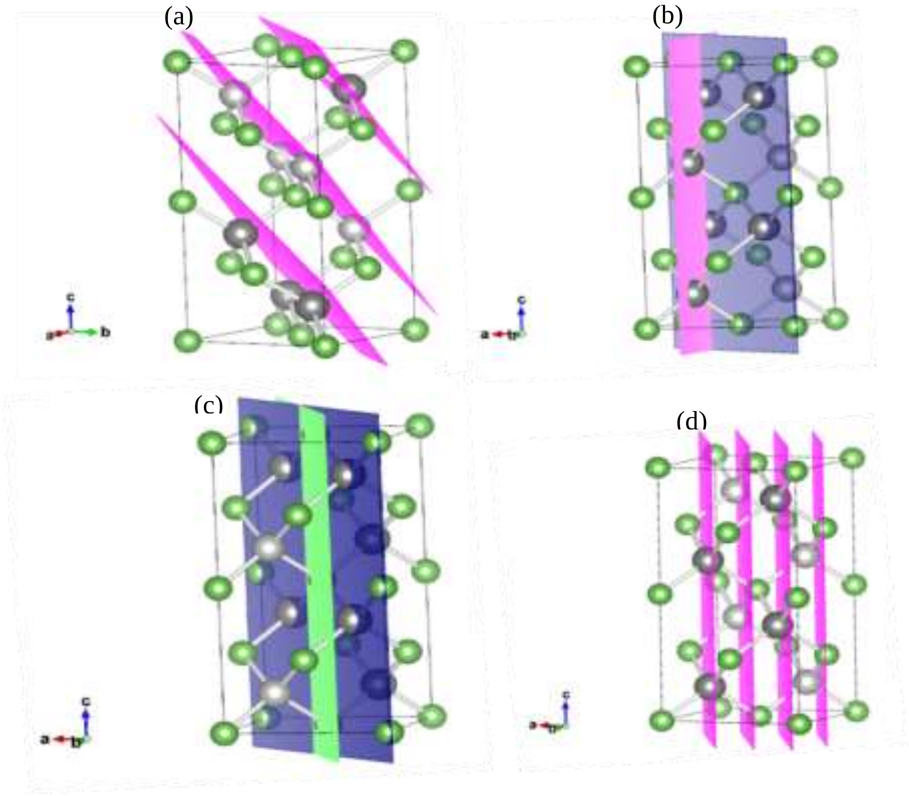

Fig. 1.2 (a), (b), (c) and (d) Crystal structures with the planes of alternating atoms (shaded) for CuPt, Luzonite, Famatinite and chalcopyrite ordering in $A_xB_{1-x}C$

1.2.2 Observation of atomic ordering in various material systems

The main advantage of using III-V alloys in competition with the Si technology in optoelectronic applications is their light emitting capability, the ability to tailor different material properties simply by varying the alloy composition of the ternary and quaternary alloys: $III_xIII_{1-x}V$, $IIIV_xV_{1-x}$, or $III_xIII_{1-x}V_yV_{1-y}$. In most of the III-V ternary or quaternary compound semiconductor alloys, which crystallize in the zinc blende structure (shown in Fig. 1.1(a)), the group III or group V atoms are distributed on their respective sublattices randomly. In certain cases, spinodal decompositions of alloys into binary components were also considered [32]. When atoms are distributed randomly in a ternary compound $A_xB_{1-x}C$, material properties such as the bandgap had been taken to be a single-valued function of the composition x. In the early 1980s, during the realization of AlInGaP laser diodes, an anomalous bandgap reduction was observed from 1.91 to 1.85 eV in the $In_{0.5}Ga_{0.5}P$ active layer lattice-matched to (001) GaAs [33,34]. Such anomalous change in bandgap revealed the presence of an atomic ordering known as CuPt-B, which was first observed in the metallic alloy CuPt [35]. In the mid of the decade, famatinite structure was observed in InGaAs on (001) InP [36], whereas CuAu I was found in AlGaAs [19], GaAsSb [37]. The CuPt ordering was found in AlInP, GaInAs, AlInAs and almost in all ternary and quaternary alloys which were grown epitaxially from the vapor phase. Other types of ordering i.e. triple period A (TP A) [38], CuPt-A [39] were found in AlInAs and AlInP, respectively. Chalcopyrite type structure was found in $CuInSe_2$ [40]. The letters “B”, “A” and “I” have their usual meanings. Originally, such atomic ordered structures were observed in metallic alloy systems. Ordering along [11-1], [-1-1-1] and [-111], [1-11] directions are referred to A and B variants, respectively in compound semiconductors looking at the similarity with the structures in CuPt [41]. For the CuAu alloy, below 380 ^{o}C, it forms a tetragonal phase with alternate copper and gold-rich (002) planes, termed as CuAu-I [42]. Similarly, the tetragonal ordered phases along [001] in compound semiconductor are identified as CuAu-I. Towards the investigation on the atomic ordering reported in many material systems, one important observation was that the bond lengths in III-V alloys remain the same as the constituent binary compounds [43]. The reported data for CuPt type ordering in different alloy systems suggest that the bond length difference is the deciding factor for such ordering. Absence of such phenomenon in AlGaP, AlGaAs and AlGaSb can be attributed to small bond length difference between the constituent binaries. Another evidence for such conclusion is $(Al_xGa_{1-x})_{0.5}In_{0.5}P$, containing Al and Ga and the bond-length difference between Al-P and Ga-P is quite small, but occurrence of CuPt ordering is possible. As there are large bond-length differences between Al-P and In-P (7.4%) and between Ga-P and In-P (7.4%), the alternate (AlGa)-alloy-rich and the In-rich planes occur in the <111> direction. However, no CuPt-B ordering reported with respect to Al and Ga atoms [44]. The different types of ordering observed in different III-V system on different substrate orientations with the associated reconstructed surface have been listed in Table 1.1.

1.2.3 Different aspects of ordering

1.2.3.1 Thermodynamics of mixing and ordering

The simplest model for the calculation of the free energy of mixing is the regular solution model which was first proposed by Hildebrand [45]. For a compound "AC" consisting of two different atoms A and C, the basic assumptions considered are - (i) random arrangement of the constituents, (ii) interaction between the nearest neighbor pairs and (iii) each atom surrounded by "Z" number of neighboring atoms. For a composition "x", the entropy of mixing is the configurational value given by

$$\Delta S^M = -R[x ln x + (1-x)\ln(1-x)] \qquad 1.2$$

The superscript M is used to indicate the change in entropy for mixing. R is the molar gas constant having the value 8.31 $Jmol^{-1}K^{-1}$.The enthalpy of mixing (ΔH^M) calculated by summing the nearest neighbor bond energies can be expressed by,

$$\Delta H^M = x(1-x)\Omega \qquad 1.3$$

Where Ω, the interaction parameter, is given by,

$$\Omega = ZN^0[H_{AC} - \frac{1}{2}(H_{AA} + H_{CC})] \qquad 1.4$$

Table 1.1 Several atomic ordering in III-V compound semiconductors

Material	Growth technique	Substrate orientation	Type of ordering	Reconstructed surface	Ordering direction
AlInP	MBE [46], MOVPE [39]	(001) 2° off towards (011) GaAs	CuPt-B	2×1, 2×4	[111]
GaInP	MBE [47], MOVPE[35], Cl-VPE [48], HT-VPE	(001) 2° off towards (011) GaAs	CuPt-A, CuPt-B	2×1,2×4	[111]
$(Al_xGa_{1-x})_{0.5}In_{0.5}P$	MOVPE[46]	(100)	CuPt	2×1	[111]
AlInAs	MOVPE [49],MBE [50]	(100)	CuPt-A	1×2	[111]
GaInAs	MOVPE [51], Cl-VPE [52]	(001) (110)	CuPt-B CuAu-I	2×1, 2×2	[111] [001]
GaInPAs	VPE [52]		CuPt-B	2×4	[111]
GaInAs	MBE [53]	(110)	CuAu	2×2	[001]
AlInAs	MBE [38],MOVPE [54]	(001) InP	CuPt-A, TP-A	2×3	
AlGaAs	VPE [20]	(110) GaAs	CuAu-I, chalcopyrite	2×2	[001]
GaInAsP	VLE [55]	(100)	CuPt	2×1	[111]

Where Z, N^0 are the number of nearest neighbors of a particular atom and the Avogadro number, 6.02×10^{23}, respectively. H_{AC}, H_{AA} and H_{CC} denote the bond energy of the bonds between A and C, A and A, and C and C atoms respectively. The above expression for the interaction parameter suggests that the positive value of the interaction parameter leads to clustering and finally separation of the two phases. On the other hand, anti-clustering and ordering may take place when the interaction parameter is negative. While short-range ordering means the number of the bonds between A and C atoms is more than that in a random alloy, the long-range ordering changes the translational symmetry of the crystal lattice in a particular direction. Though the regular solution model does not provide any insight into the thermodynamics of mixing, it is useful in the calculation of the phase diagrams of binary, ternary, quaternary compounds. A more physical model for enthalpy of mixing is the delta lattice parameter (DLP) model. The interaction parameter, depending on the equilibrium atomic spacings of the end component binary compounds of the alloy, is given by [56],

$$\Omega = k\frac{(a_{AC}-a_{BC})^2}{(a_{AC}+a_{BC})^{4.5}} \qquad 1.5$$

Where a_{AC}, a_{BC} are lattice parameters of the end-pint binary compounds and k is adjustable fitting parameter. The model explains quite efficiently the positiveness and the increase of the enthalpy of mixing with an increase in size difference of the constituents. Several models such as virtual crystal approximation (VCA), valence force field (VFF) were developed to match the experimentally measured values of the interaction parameter [57]. The failure of VCA, which assumes distribution of the atoms in the lattice to be uniform, lead to the consideration for the interaction between the atoms to be due to strain, stretching and bending of bonds in VFF. The models give a large positive enthalpy of mixing of alloys constituting of binaries with large lattice mismatch. Thus there is always a possibility of phase separation or clustering below a certain critical temperature above which randomness dominates the free energy. It is an important question whether the superlattice type structures are thermodynamically favorable relative to either phase separation or random arrangement. Early single interaction parameter model [58] and a positive enthalpy for all disordered alloys led to the interaction between the constituents for the alloy formation to be repulsive which originates from the energy for packing a lattice with dissimilar atoms [59]. The disordered structures upon cooling exhibit clustering, then a phase separation due to the repulsive nature of the interaction. On the contrary, the attractive nature results in anti-clustering and subsequently long-range or short-range order on the cooling of the disordered alloy. However, the main problem in such an assumption was lying in the fact that it assumed ordering and disordering phenomena to be mutually exclusive. Actually, the excess enthalpy is comprised of an attractive and a repulsive term. In a pseudo-binary system like $A_xB_{1-x}C$, the perfectly ordered structure can be thought of a repetition of a local arrangement of A and B atoms with the common atom C. A random structure comprised of a few local clusters with a number of them in a particular phase. One part of the excess enthalpy is purely repulsive which is basically the elastic energy required for the deformation of pure AC and pure BC from their equilibrium volume to the modified volume of the alloy. Another part is due to the substitution of atoms in pure crystal to form the alloy in the desired phase. So, the excess enthalpy can be expressed as [29],

$$\Delta H^{(\gamma)}(x) = G(x) + \sum_c p_C^{(\gamma)}(x)\,\varepsilon_C \qquad 1.6$$

With G(x), p_C and ε_C are the elastic energy, the number of cluster C in the phase γ and the substitutional energy for each cluster, respectively. When $\Delta H \geq 0$ the phase is unstable and for the opposite, the structure could be stable. As the elastic energy depends only on x, so the probability of finding a cluster for a particular composition at a temperature depends only on the substitutional energy. The systems with positive substitutional energy show anti-clustering whereas its negative value is responsible for clustering. Calculation of energy and formation enthalpies revealed the stability of the ordered structures with respect to the random alloy and also the phase separation. Three types of phases i.e. unstable, metastable and stable ordering can be distinguished as depicted in Fig. 1.3 [29].

1.2.3.2 Surface reconstruction

During the MOCVD growth of an alloy, with a V/III ratio much greater than unity, in the mid-temperature range, the growth process is diffusion or mass-transport limited. If we consider the growth of $A_xB_{1-x}C$, for example, a random arrangement of A and B atoms is expected to be deposited on the surface. If the random arrangement of the atoms is covered by the next layer before the diffusion of the atoms to significant distances, the randomness is frozen and further diffusion of the atoms is literally prohibited. But in the actual situation, during the growth of GaInP, the formation of Ga and In rich alternative layers at the surface due to a small amount of rearrangement of atoms makes an ordered structure. The ordered structures possess lower energy in comparison with the random alloy because of the reduction of strain energy through dimer formation between the group V atoms and arrangement of the large and small group III elements layer by layer along <111> direction [60]. Total energy minimization calculations showed that the lowest energy ordered structure is El_1 (chalcopyrite) which is observed very often in real bulk systems [29]. The ordered structure having the highest energy, $L1_1$ (CuPt), is the most commonly observed in the bulk [61]. The unexpected ordering in AlGaAs system despite the fact that AlAs

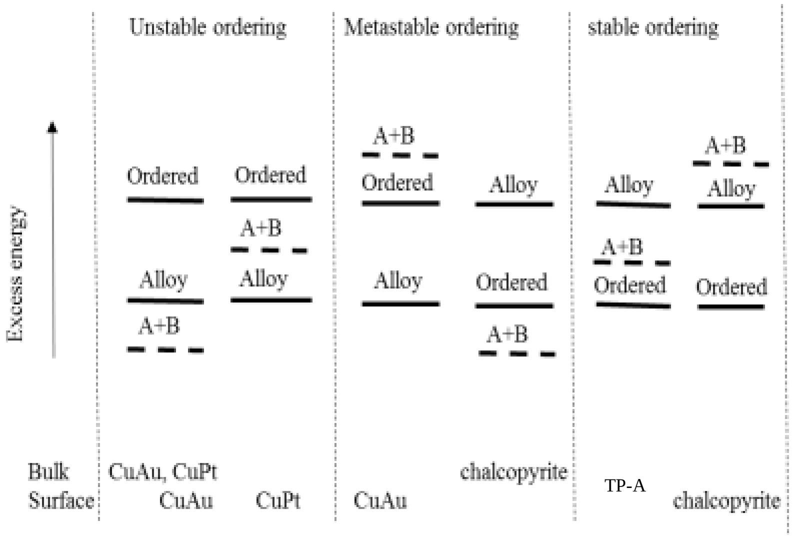

Fig. 1.3 Classification of ordering on the basis of excess energy in the bulk and surface of the materials

and GaAs have nearly equal lattice parameters and surprisingly, little ordering in GaPAs having a large difference in the bond lengths between GaP and GaAs and observation of CuPt ordering in most of the III-V alloys despite its higher energy for bulk in comparison to the other ordered structures [62], led to the idea of ordering as a surface phenomenon rather than its existence in bulk. The calculations on the stability of different surface reconstructions of Zunger and his coworkers, the pioneers in the theoretical field of ordering, revealed the stability of the two variants of the CuPt structures among the four equivalent {111} directions near the surface [62]. There exists a significant difference between the bulk and the surface structures as shown by the group. The symmetries of the minimum energy configurations for the bulk and surface structures are different. The surface of the CuPt ordered materials showed (2×1) surface structure when observed through reflection high energy electron diffraction (RHEED) during MBE growth [63]. The surface reconstruction could be attributed to the dimer formation/pairing by the dangling bonds of group V atoms. Similarly, (2×3) and (1×2) surface reconstruction were attributed to triple period and CuPt-A ordering, respectively because of the observed one to one correspondence between the surface reconstruction and the ordering [64]. The reconstructed surface structures corresponding to the ordering are shown in Table 1.1.

1.2.3.3 Growth kinetics

While surface thermodynamics dictates the atoms their energetically preferential sites, it is the growth kinetics that decides the extent to which the pattern of the atomic arrangements can propagate into the bulk during a real growth process. The only concern of thermodynamics is the initial and final states at equilibrium, but, it is incapable of providing the information about the time to reach the equilibrium lowest energy states and the rates at which the intermediate steps occur. Since the typical growth rate in MOCVD is very low (1μm/hr), the system can be considered to move through near-equilibrium. The difference in the formation rate and destruction rate of the growing species is very small compared to the rates of the reactions itself. The major processes of kinetics are: the different physical surface processes, chemical reactions, heat and mass transport [65]. Physical surface process describes various microscopic surface features like surface reconstruction, step size, adatom motion, etc. Mass transport controls the flow of the materials to the solid/vapor interface. The rates of the various chemical reactions occurring either homogeneously in the gas phase or heterogeneously at the interface also decide the overall growth rate. The growth parameters such as growth temperature, growth rate, and substrate orientation play vital roles in the propagation of the near-surface ordering. The kinetic factors during growth have shown an immense effect on the ordering. For example, for the GaAsSb system, the reduction of the growth temperature below 550 ^{o}C shows the absence of the chalcopyrite structures [66]. The cause may be the low surface mobility of the adatoms so that the lower energy ordered pattern cannot form. When the growth rate is also reduced in the above mentioned growth temperature, the atoms have sufficient time to form ordered structures despite the low surface mobility. With a change in substrate orientation, the number and nature of bonds play a major role in the surface mobility of the adatoms. L_{10} (CuAu) in MBE grown AlGaAs on (110) GaAs [20], decrease of the intensity of the super-spots in GaAsSb on (110) substrates [66], elimination of CuPt ordering in GaInP on (111) substrates [67], showed the strong dependence of ordering on the kinetic factors. Besides, many other elementary growth events such as step flow, single to double-step transitions, strain relief, etc. also have immense effects on ordering [68].

1.2.4 Consequences of ordering

The observed effects of ordering on various material properties make this phenomenon interesting from the application perspective. The long-range order parameter is measurable by transmission electron diffraction pattern, X-ray diffraction [69]. Regarding the effect of ordering on the optical properties, crystal field splitting and reduction in band-gap, such indirect measurements were involved in determining the extent of ordering [70]. A general dependence of a physical property *P(n)* on the order parameter *n* was established as follows [62]

$$P(n)=P(0)+n^2\left[p(1)-P(0)\right]+O\left(n^4\right) \qquad 1.7$$

P(1) and P(0) are the properties with fully ordered and without order phase. The fundamental reason for the difference between the ordered and disordered structures is the altered symmetry. In case of CuPt structures, the periodicity is doubled compared to that of zinc-blende which in turn makes the Brillouin zone folded [71]. As a result, two electronic states fold into a single K point. For CuPt type ordering in (111) direction, the L and Γ states fold to the $\overline{\Gamma}$ state. The zinc blende conduction band minimum appears to split into a doublet. When the spin-orbit coupling is considered, there are two conduction band levels whereas three valence band levels. Thus, the introduction of ordering makes the states with the same symmetry to repel each other which results in a change in the spectroscopic signature [72].

1.2.4.1 Bandgap reduction

One of the prominent effects of ordering is the bandgap reduction observed in CuPt ordered GaInP alloy [39]. Theoretical calculations showed the repulsion amongst the equal-symmetry states, causing the lower state to shift down, thus results in a reduction of the bandgap. The theoretical calculations in conjunction with the experimental measurements give the maximum bandgap reduction of 380 meV in fully ordered $GaInP_2$ and the highest value of the observed order parameter (*n*) deduced as 60% [73]. Another significant aspect is that sometimes the repulsion between the states becomes so strong that the shift makes Γ point below the X point, making an indirect gap semiconductor to one having direct gap. Such effects have been observed in Ga_2AsP [74]. Another interesting aspect is that sometimes ordering can be used to reverse the order of the bandgaps of two materials. Ordering induced lowering of the bandgap of GaAsSb beyond HgCdTe makes the antimonide useful for the far-infrared application [75]. The ordering induced lowering of the conduction band minimum could also lead to homojunction disorder/order/disorder quantum well structures for optoelectronic applications [76]. Again, ordering could also change type I to type II band alignment, although not observed yet.

1.2.4.2 Valance-band splitting

The average value of the energy (E_{av}) and the splitting of the valence band with respect to E_{av} are given by [72]

$$E_{av} = \frac{1}{6}(\Delta^{SO} + \Delta^{CF}) \tag{1.8a}$$

$$E_1 = \frac{1}{2}(\Delta^{SO} + \Delta^{CF}) \tag{1.8b}$$

$$E_2 = \frac{1}{2}\sqrt{(\Delta^{SO} + \Delta^{CF})^2 - \frac{8}{3}\Delta^{SO}\Delta^{CF}} \tag{1.8c}$$

$$E_3 = -\frac{1}{2}\sqrt{(\Delta^{SO} + \Delta^{CF})^2 - \frac{8}{3}\Delta^{SO}\Delta^{CF}} \tag{1.8d}$$

Where Δ^{SO} and Δ^{CF} are the energy difference due to split-off band and crystal field splitting, respectively. In case of strain-induced valence band splitting, the energy states E_1, E_2 and E_3 represent the heavy hole, light hole, and the split-off bands. The transition intensities depend only on strain in case of zinc blende crystals but as the L states folded into the Γ states in presence of ordering, so the transition corresponding to the conduction band minimum to the doublet depends on the order parameter. Thus the extent of ordering can be deduced from the intensity variation as well as from the comparison of the splitting of the valence band theoretically and experimentally

[72]. The obtained transitions appeared as a result of ordering in specific directions would depend on the polarization of the excitation. This polarization dependent transition makes the ordered materials to be useful as polarization detectors. This also enables the optical detection of the type and also the variant of the ordering present in a material system.

1.2.4.3 Carrier effective mass enhancement

Another effect of the $\Gamma - L$ coupling in the ordered structures is the alteration of the carrier effective mass. Bandgap reduction due to ordering causes a decrease in the effective mass whereas the coupling behaves in the other way and the resultant effective mass depends on the balance of the two counteracting effects [77]. Another aspect of ordering is the anisotropy in the effective mass in the direction of ordering with respect to the other directions [78].

Moreover, the theoretical predictions regarding the increase in critical pressure for the transition of direct bandgap materials to the indirect gap, the generation of electric fields due to ordering are verified by the experiments on the ordered systems [79,80]. Another observed phenomenon is the up-conversion in InGaP and AlInGaP materials where emission was observed at a higher energy compared to the excitation even at low temperatures which might be the consequence of the localization effects due to ordering [81]. Observation of the fundamental ordered structures, its origin and its effect on the material properties have been studied and correlated through years by several groups [29,63,68,82]. In the meantime, superlattice type ordering in a comparatively large length scale have been reported by Albert Chin and his coworkers who reported a partially ordered $Al_xGa_{1-x}As/Al_yGa_{1-y}As$ periodic structure in the 0.75μm thick $Al_{0.3}Ga_{0.7}As$ on (111) A GaAs [83]. They have also observed the same ordering in AlGaAs barrier layers with GaAs quantum well on (111) B GaAs but they did not find any superstructure on (100) substrates. The bandgap anomaly observed in atomic-scale ordering due to doubling of the periodicity of the lattice was also appeared in such structures although relatively small. The optical quality was also enhanced as a result of ordering. The origin was not very clear but the formation of such structures on <111> substrates but absence for <100> might have kinetic influence. The steps in the oriented substrates may enhance the step flow growth which could be considered as the catalyst of the ordering.

1.2.5 Ordering in AlGaAs

As our material system is concerned, the $Al_xGa_{1-x}As$ alloy grown on (100) GaAs substrates, one of the most-studied materials among the III-V alloys, was grown by LPE since the 1960s and by VPE since the 1970s. However, no one has reported the existence of CuPt-B ordering in this alloy grown by MOVPE, MBE, or LPE. A significant broadening of the luminescence peak was observed in MBE grown AlGaAs by Petroff *et al.* due to quasi-periodic alloy clustering [84]. CuAu-I type of ordering in MOVPE grown $Al_xGa_{1-x}As$ was reported on GaAs substrates by Kuan *et al.* in 1985, where a clear separation of GaAs and AlAs atomic monolayer was observed at different growth temperatures for different compositions [16]. Later, in the mid of 90s Albert Chin and his coworkers observed spontaneous formation of Al and Ga rich compositional modulation in $Al_{0.4}Ga_{0.6}As$ quantum well layer with $Al_{0.7}Ga_{0.3}As$ barrier on (111) GaAs substrates grown by MBE whereas there were no such periodic structures for (100) substrate orientation [83]. The enhancement of Photoluminescence intensity and the reduction in the transition energy for (111) AlGaAs were reported. Formation of alternative Al and Ga rich layers with a periodicity of 55 Å, as confirmed from Transmission Electron Microscopy, has been attributed as the probable reason for the observations. The difficulties regarding the growth of AlGaAs, which is a very important material system in optoelectronic device applications, can be overcome by the spontaneous ordering during the growth of the material [83]. The Long range spontaneous ordering over a length scale much greater than monolayer has been observed in MBE grown $Al_xGa_{1-x}As$ layer with aluminum rich and gallium rich superlattice constituents with period 50–70 Å grown on (111) facets of specially patterned (100) GaAs substrate [85]. We have observed natural superlattice ordering in a multiple monolayer scale in MOCVD grown AlGaAs barrier layer of GaAs/AlGaAs multi-quantum well (MQW) and AlGaAs epilayer on the conventional (100) GaAs substrates [21]. TEM and X-ray study confirmed the presence of superlattice type ordering in the AlGaAs epilayer with a fine modulation in Al composition. As an effect of ordering, enhancement of Photoluminescence intensity and reduction in bandgap energy in AlGaAs on (100) GaAs.

1.2.6 X-ray analysis of the ordered structures

Among various direct and indirect measurement techniques, X-ray scattering is one of the useful tools for structural characterization in the nano-scale regime. The electron density and interface roughness of the layered structures can be analyzed by X-ray reflectivity in the low angle regime whereas high angle diffraction is used to extract the atomic information (arrangement, orientation, etc.). High-resolution X-ray diffraction (HRXRD) is very efficient in determining compositional modulation present in a layered material [22]. The periodicity in the lattice gives rise to satellite peaks in the reciprocal space separated with an inverse relation to the real space. The intensity profile is sensitive to the thickness of alternative layers, interface roughness, composition, and strain profile [86]. The utility of such spontaneously-grown superlattice-type structures depends on its thermal stability since many device fabrications involve high-temperature processing of the grown material. Interdiffusion across the interface due to thermal treatment plays an important role in such structures regarding device applications. The most common approach to study interdiffusion is to perform direct measurements of the profile across the interface as a function of annealing time. This type of work could be performed with Rutherford backscattering spectrometry (RBS) [87], cross-sectional transmission electron microscopy (XTEM) [88] and most frequently with secondary ion mass spectrometry (SIMS) [89], but the spatial resolution of the depth profiles is limited by the instruments. To study the interdiffusion of Al and Ga atoms in AlGaAs/GaAs heterostructures, a number of experimental techniques such as Auger electron profiling [90], wavelength modulation in quantum well lasers [91], cathodoluminescence (CL) and transmission electron microscopy [92] have been applied. Photoluminescence spectroscopy has also been used in case of MQW systems as well as superlattice-type structures [93]. In comparison with such direct measurements of interdiffusion, x-ray diffraction (XRD) of superlattices are sensitive to the quality and uniformity of the interfaces involved [94]. As XRD satellite peaks are very sensitive to the various parameters of the superlattice structure, the interface roughening by interdiffusion as a result of thermal annealing can be extracted using high-temperature x-ray diffraction (HTXRD) technique. XRD has been involved to study interdiffusion in deliberately grown superlattice structures in II-VI/II-VI [95] and IV-IV materials systems [96]. Fatah *et al.* have shown that the XRD technique is more useful in case of MQW or superlattice-type structures rather than single quantum wells, as has been demonstrated in the case of CdTe/CdMnTe superlattice system [97].

1.2.7 Photodetectors

The optoelectronic devices which are able to convert the absorbed optical energy into its equivalent electrical analog, are called photodetectors (PDs). PDs generally work under reverse bias. The working principle of the PDs is basically a three-step process mentioned below

i. Generation of photocarriers by absorption of an optical signal.

ii. Transportation of these photocarriers through the semiconductor towards the electrical contacts.

iii. Collection of the carriers in the external electrical circuit.

From the structural point of view, PDs can be classified into multiple categories like p-n junction PDs, p-i-n, PDs, metal-semiconductor Schottky PDs, heterojunction PD, metal-semiconductor-metal (MSM) PD, etc.

Metal-Semiconductor-Metal Photodetector:

When two identical or non-identical Schottky junctions (SJs) are connected in the back-to-back configuration on a coplanar semiconducting surface, the device is known as metal-semiconductor-metal (MSM) structure [98]. Usually, an undoped or intrinsically doped semiconducting surface is preferred for the fabrication of MSM structure. As here two SJs are connected back-to-back, application of external bias always makes one of them forward biased and the other one in reverse biased. The light is absorbed only by the semiconductor, which produces electron-hole pair within it. Afterward, the electrons and holes are separated and collected to the opposite metal contact. The maximum absorption of light by the semiconductor is possible when this layer possesses a thickness which is a little bit greater than the absorption length. In the MSM structures, the main drawback is the high dark current under bias due to the extended electric field at both the junctions. The inclusion of MQW or superlattice structures in the semiconductor layer can limit the dark current and enhance the speed at the same time [99]. The main advantage of using AlGaAs is its ignorable lattice mismatch with GaAs substrates. GaAs-AlGaAs material system is widely used for quantum cascade lasers based on GaAs [100]. Large conduction band offsets are desirable in the active region of the quantum cascade lasers to suppress the thermally activated processes which limit device performance at high temperatures and also allow increasing the energy separation among the subbands. GaAs based optoelectronic devices attracted much attention in telecommunications [101]. The most large scale application of the AlGaAs/GaAs system is quantum well-infrared photodetector (QWIP) [102]. We have designed metal-semiconductor-metal photodetector based on the superlattice structures using the AlGaAs/GaAs (100) grown by MOCVD [28]. Lambert W function was incorporated to simulate the device. We have studied the effect of the superlattice structures on the spectral and temporal response of the device by comparing the figure of merits with those of a device based on homogeneously alloyed AlGaAs. The band diagram of a typical MSM structure with intrinsic (n-type) is shown in Fig. 1.4.

1.3 Motivation and objectives

Since the first report of atomic ordering in AlGaAs [20], the topic has attracted much interest not only from the device application perspective but for the flavor regarding its origin and nature also.

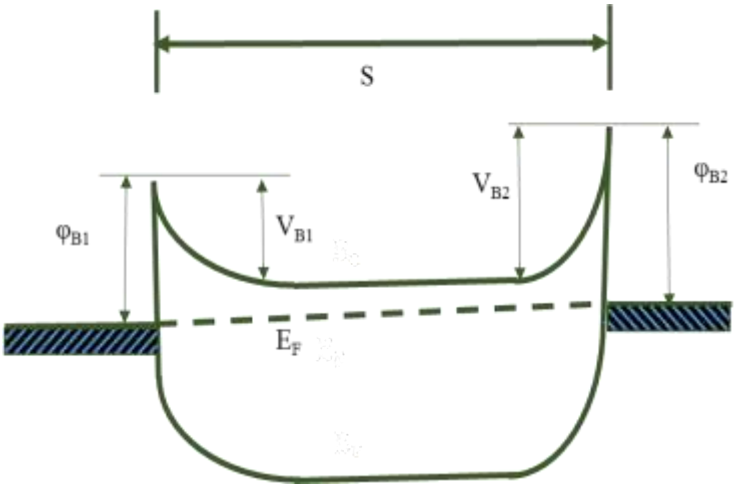

Fig. 1.4 Band diagram for the metal-semiconductor-metal structure

Theoretical predictions and experimental results have demonstrated the effect of ordering on the physical properties of the system. The atomic ordering shows significant effects on device performance also. Therefore, it is critical to understand the ordering in semiconductor alloys during the design and fabrication of devices. Observation of natural superlattice ordering in the AlGaAs barrier layer of GaAs/AlGaAs MQW system has led us to study such structures in great detail.

Similar multiple monolayer superlattice structures were also observed in AlGaAs/GaAs (100) epitaxial layer [21]. Since X-ray scattering techniques reflect the quality of the interface with high precision, we looked for a combinatorial approach involving low angle reflectivity and high angle diffraction for the information from layers and atomic planes, respectively. To investigate the stability of the spontaneously grown structures, high-temperature rocking curve analysis was involved. Studying the interdiffusion phenomena through the interface of the superlattice structures is interesting and also useful regarding the diffusion mechanism in the material and also for the device application. We used the theoretical formulation of interdiffusion across the interface through a comparative study of virtual interdiffusion driven kinematical diffraction and real-time rocking curve measurements. The overall effect on the optical and electronic properties is also important which led us to the fabrication of the device and study of the spectral and temporal response on the light of localization of carriers and the electric field due to the superlattice structures.

1.4 Outline of the thesis

The whole work has been arranged in a number of chapters form with the content given below.

Chapter 1 briefly describes the background and the nature of the present work covered in the thesis in a nutshell.

Chapter 2 describes some basic aspects of metalorganic chemical vapor deposition technique.

Chapter 3 contains the description of the experimental techniques used for the device fabrication and understanding the structural, optical and electrical properties of the materials.

The results we obtained are depicted in chapters 4 5 and 6.

Chapter 4 describes the growth procedure we followed and observation of a new type of spontaneous superlattice ordering in our material system through various structural characterizations.

Chapter 5 discusses the stability of the ordered structures and interdiffusion phenomenon in such structures through high-temperature X-ray diffraction measurements.

Chapter 6 describes the fabrication of the photodetector based on the superlattice structure and the superiority of the device in terms of spectral and temporal response relative to the device based on the homogeneous alloy of the same material.

Chapter 7 contains the conclusions we have drawn based on the study.

Chapter 2

Basics of MOCVD growth technique

2.1 Introduction

Epitaxial crystal growth of materials made it possible to fabricate various high quality low dimensional complicated structures for basic research as well as large scale electronic and photonic device applications. Epitaxy is basically controlled layer by layer growth of single crystalline thin films of a particular material on a given substrate with a definite crystallographic relationship between the growing film and the substrate. If the same material is grown on the substrate, the epitaxy is termed as homoepitaxy. On the other hand, when the growing material is different from the substrate, the process is called heteroepitaxy. The various epitaxial techniques available for the layer by layer growth are liquid phase epitaxy (LPE), chloride-vapor phase epitaxy (ClVPE), hydride-vapor phase epitaxy (HVPE), metal-organic chemical vapor deposition (MOCVD) and molecular beam epitaxy (MBE). MOCVD technique is the most efficient technique to grow compound semiconductors in a large scale due to its high throughput. Table 2.1 showed a comparison between the different epitaxial growth techniques. Despite the complexity of the MOCVD growth process, the technique offers growth of versatile materials for commercial applications with atomically flat interface between multilayers.

2.2 Lattice matching in epitaxial growth

When we consider heteroepitaxy, the relative lattice parameter of the substrate and the epitaxial layer plays a vital role in the growth process and formation of misfit dislocations and defects. In case of pseudomorphic or layer by layer growth, perfect lattice matched layers can be grown. Difference in lattice parameters causes formation of strained layers which can be of two types – when the lattice parameter exceeds that of the substrate, the layer is grown with compressive strain and when the lattice parameter of the layer is smaller, the layer is under tensile strain. The Fig. 2.1 demonstrates the lattice matched and strained layers. For the growth of low dimensional heterostructures, both the strain profile and the band diagram should be considered simultaneously. The bandgap engineering helps us to optimize the desired band diagram for real devices. For example, AlAs has a bandgap 2.1 eV and GaAs has a bandgap 1.43 eV at room temperature (300 K) [103]. When these two alloys are mixed together to get the ternary compound $Al_xGa_{1-x}As$, then depending on the value of composition (x) of Al, the bandgap of the compound can be varied from 1.43 eV to 2.1 eV. In general, for ternary compound $A_xB_{1-x}C$, the variation of the bandgap with composition(x) can be written as $E_g(x) = E_g(0)+bx+cx^2$ where c is the bowing parameter. Fig. 2.2, which is basically the bandgap vs lattice constant diagram for various semiconductors [104], depicts clearly the bandgap and lattice parameter values of different binary and ternary compounds made out of them.

Table 2.1 comparison of different epitaxial growth techniques

Growth technique	Phase of the constituents	Advantages	Disadvantages
LPE	Liquid	Simple to operate, high purity of the material	Less flexibility, nonuniformity of the grown materials
ClVPE	Vapor	Simplicity, purity	Al and Sb alloys difficult to grow, graded layer at the interface
HVPE	Vapor	Large scale growth	Hazardous sources, Al, Sb alloys difficult
MBE	Vapor	Simple process, uniform growth, abrupt interface, superlattice structures with high precision,	As/P alloys difficult, expensivie, low throughput
MOCVD	Vapor	Most flexible, large scale production, high precision	Expensive reactants, hazardous precursors

2.3 Overview of MOCVD process

Metalorganic chemical vapor deposition (MOCVD) is also termed as organometallic vapor phase epitaxy (OMVPE) and by other permutations of the same letters (OMCVD or MOVPE). This epitaxial growth process started with the pioneering work of Manasevit [7,105] in late 1960s. After that, it took a huge time for the development of the technique to be precise for atomically abrupt interfaces and suitable for the large scale production at the same time. Undoubtedly, it has become the most versatile technique for the production of III – V compound semiconductor materials for optoelectronic device applications. All the desired parameters such as layer compositions, doping levels, and thicknesses can be manipulated more or less independently in order to produce a device with a complex heterostructure. The fundamental processes that have been taken place during crystal growth can be divided into thermodynamic and kinetic components. Thermodynamics controls the direction of the overall growth process whereas kinetics decides the rates of the various processes occur. Hydrodynamics and mass transport determine the rate of transport of precursor materials to the interface formed between the vapor and the solid phase. All the factors combinedly

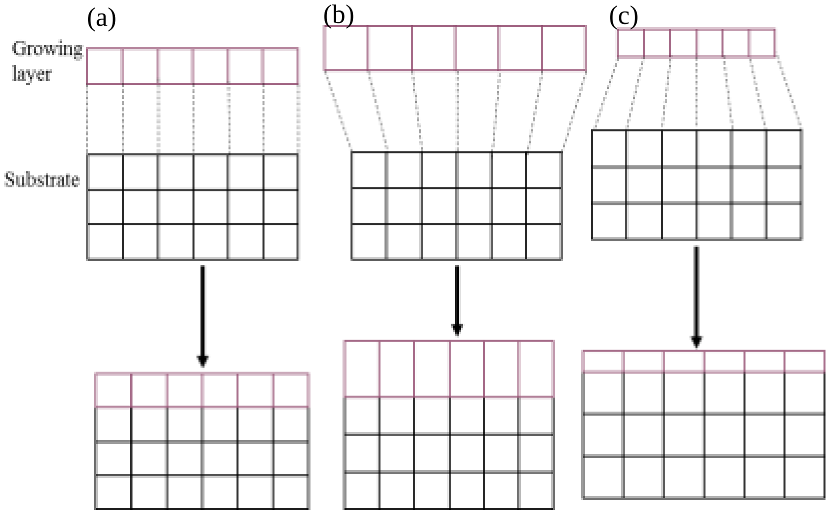

Fig. 2.1 Epitaxial growth of (a) lattice matched layer ($a_{layer}=a_{sub}$) (b) layer under compressive strain when $a_{layer} > a_{sub}$ and (c) layer with tensile strain as $a_{layer} < a_{sub}$

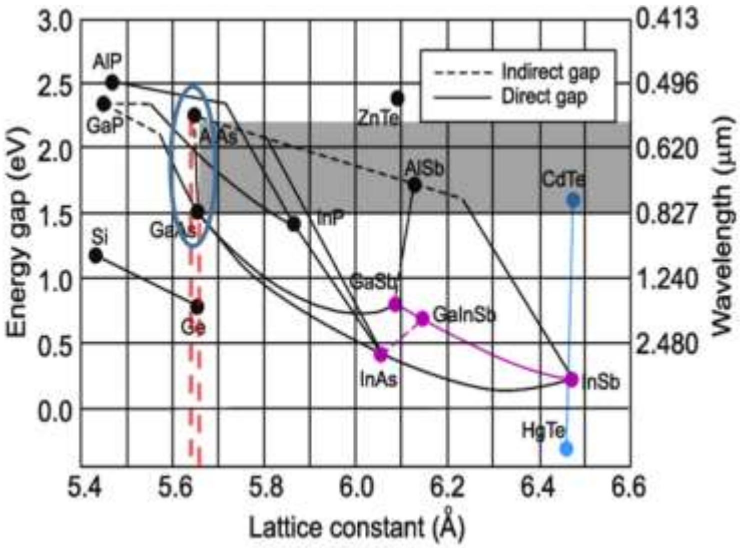

Fig. 2.2 Energy bandgap as a function of lattice constant for several compounds. The red broken lines show the nearly equal lattice parameters of GaAs and AlAs and the shaded region show the wavelength range covered by the material of our interest in the whole composition range

define the overall growth process. To understand the growth mechanism, dependence of the growth rate on various external parameters were studied [106–108]. A general categorization of the process limiting the growth rate was done by Shaw after studying the growth rate as a function of temperature [109]. As MOCVD is an exothermic process, thermodynamically limited growth rate decreases with increasing temperature [110]. An increase in growth rate with temperature can be concluded as kinetically limited case. If the growth rate remains nearly unaltered with temperature, the process must be mass transport limited. Similarly, dependence on other factors such as the total gas flow rate, substrate orientation revealed the dominating factor for the growth process. Observations by different groups led to the conclusion that the MOCVD growth process is determined by mass transport in the temperature range of 550-750 ^{o}C [106,107]. In the lower temperature regime, the growth rate is found to be controlled by the kinetic factors and at temperatures above 750 ^{o}C, it is thermodynamically limited. Another important observation for the growth of III-V alloys is that the growth rate depends linearly on the flow rate of the group III species entering the reactor. Assuming the mass transport through a fictitious laminar-flow boundary layer, the linear dependence of the growth rate on group III flow rate suggests that interface is depleted of the group III element to maintain the stoichiometry. High group V flow or V/III ratio is typically maintained to preserve the stoichiometry of the growing layer since the vapor pressure of these elements are higher compared to the group III atoms.

2.4 Equipment of MOCVD system

The basic chemical reaction of MOCVD process, the kinds of sources and in general the hardware used to deliver and process the sources are discussed below.

2.4.1 Chemical reactions

The essence of the MOCVD process for deposition of compound semiconductors can be considered as the simplified version of a more complex step by step process given as

$$R_nA + BH_n \rightarrow AB + nR \qquad 2.1$$

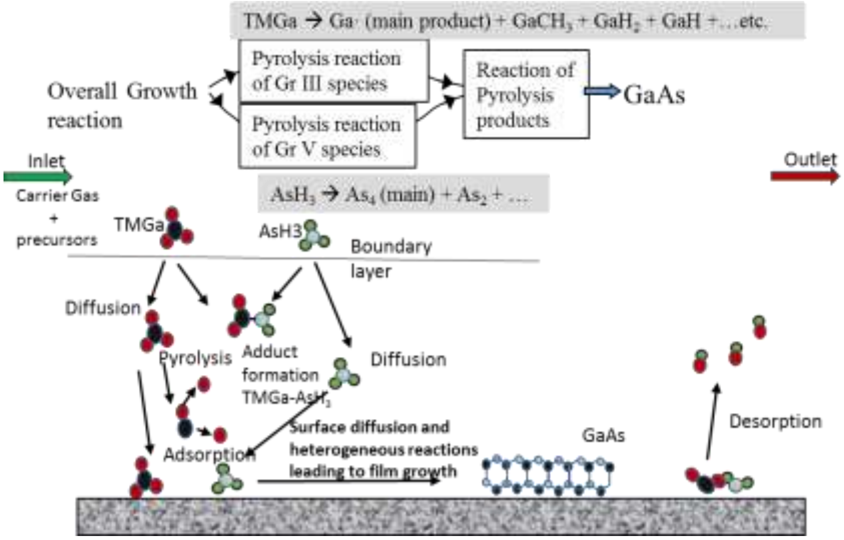

Fig. 2.3 Schematic representation of various processes inside the reaction chamber leading to the growth of single crystalline GaAs

R_nA is the organometallic compound of group III species with R being H or alkyl (CH_3, C_2H_5), BH_n represents the hydride of the group V element and AB is the desired compound semiconductor. Actually, both the group III and group V precursors undergo pyrolysis to give various products among which reaction between the main products from both side gives rise to the desired compound in solid phase under proper temperature and pressure. Many other byproducts would be present which are excluded from the chamber through the outlet. As an example, a schematic of the processes occur in the reaction chamber for the growth of GaAs from trimethylgallium (TMG) and arsine (AsH_3) is shown in Fig. 2.3.

2.4.2 Precursors

Choice of the source molecules for MOCVD growth of compound semiconductors determines the kinetics of the pyrolysis reactions which in turn controls the overall growth process. An important factor in MOCVD growth process is the energy of the metal-carbon bond in the precursor molecule. The bond strength depends on the electronegativity and size of the metal and configuration of the radical as well. Observations showed that the metal-carbon bond strength is decreased as more number of carbon atoms are attached to the central carbon [111]. The methyl-metal bonds were found stable for group II or III species and hydrides for group V or VI showed maximum stability [112]. Another important aspect is the vapor pressure of the precursors that influences the overall growth. For MOCVD growth process, the metal-carbon bond energy in the precursor molecule (organometallic compounds) is important it determines the stability of the molecule against pyrolysis. The bond strength depends on the electronegativity of the metal and the size and configuration of the radical. In case of group II, III, V species, the metal-carbon bond strength is decreased as the number of carbon atoms bonded to the central atom, indicated as no, is increased. The bond strength gets increased in the order, $H > 0^o$ (Me) $> 1^o > 2^o > 3^o$ [113]. As a consequence, the vapor pressure of the heavier branched molecules is higher in comparison with the lighter molecules. For the growth of AlGaAs, we used TMG and TMA (trimethylaluminium) as the group III precursors, while arsine is used as the group V source.

2.4.3 Reactor components

An MOCVD reactor comprises three major components:

The gas delivery system that carries different gases to the reaction chamber

The reaction chamber where the growth process takes place

The reactor safety system

A simplified schematic is shown for the MOCVD growth system is shown in Fig. 2.4.

2.4.3.1 Reactor gas delivery system

The function of the gas handling system is mixing and metering of the gas entering the reactor. Timing and fraction of the gas entering the reactor will determine the crystallinity and stoichiometry of the epilayer structure. This reactor gas handling system is an ultra-clean, leak-

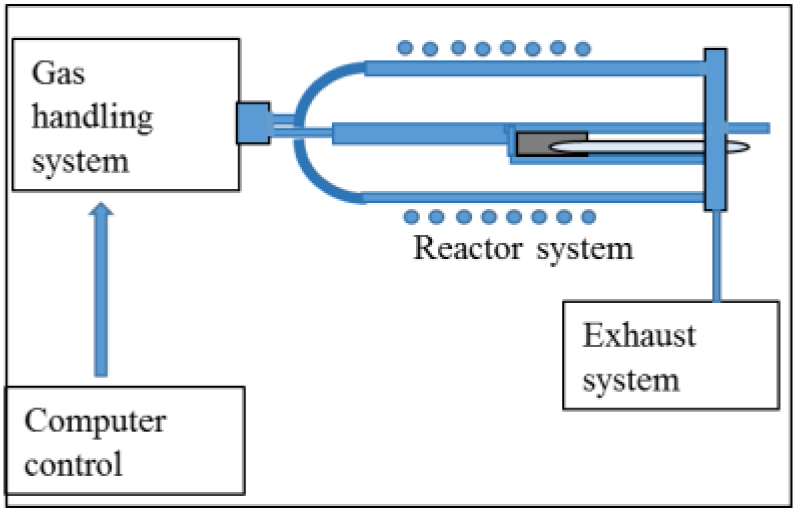

Fig. 2.4 Schematic of the overall MOCVD growth system

free arrangement of stainless-steel tubing, automatic valves, and mass flow controllers, as shown in Fig. 2.5.

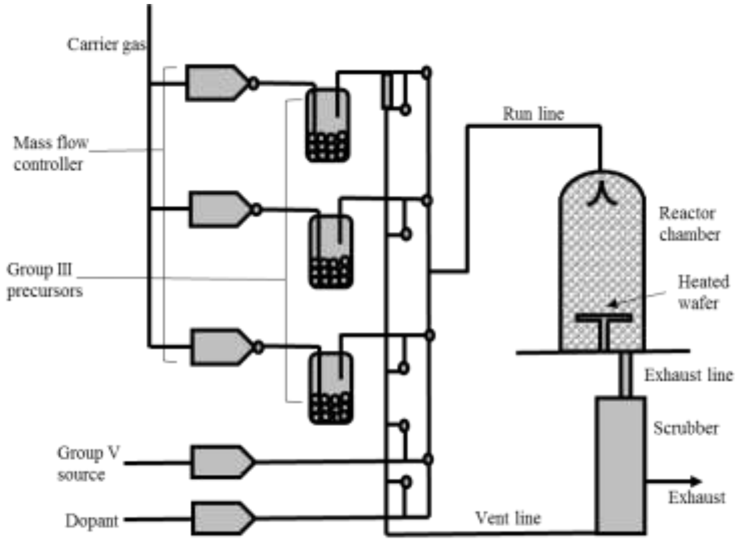

Fig. 2.5 Schematic diagram of the gas handling system in a typical MOCVD reactor

Each constituent e.g. gaseous hydride or solution of the organometallic compounds having high vapor pressure requires a different control system to be delivered to the reaction chamber. The delivery modules for hydride generally requisite a few valves and Mass Flow Controller (MFC) which is a kind of device which is used to measure and control the flow of a gas or liquid [114]. The elements of an MFC are base, sensor, bypass, control valve, and printed circuit board. All other components are mounted on the base. The gas flows through the sensor tube and it causes heat transferred from the upstream to the downstream resistance thermometer element. This temperature differential is linearized and amplified into a 0 to 5 V of the output signal through a bridge circuit. The comparison of the output signal with the setpoint causes an error signal that directs the control valve to remain open or closed for maintaining a regular flow at the setpoint level. The components of a typical mass flow controller are shown in Fig. 2.6. The source materials are contained in stainless-steel bubblers stored in a refrigerated bath to produce a stable vapor pressure over the source. These individual pressure-controlled alkyl bubblers in temperature-controlled baths provide reliable and constant delivery. Volatile precursor molecules transported by the carrier gas (mainly H_2 or N_2) to the reactor chamber. A small variation in the carrier gas flow could change the source delivery.

In all configurations, the flow of vapor is directly related to the vapor pressure of the material kept in the vessel, which varies with temperature in accordance with the characteristics of the liquid. The delivery rate of a liquid or solid organometallic source depends on its temperature, the flow rate of the carrier gas through the organometallic bubbler, and the pressure of the bubbler. The flow of a source can be expressed as

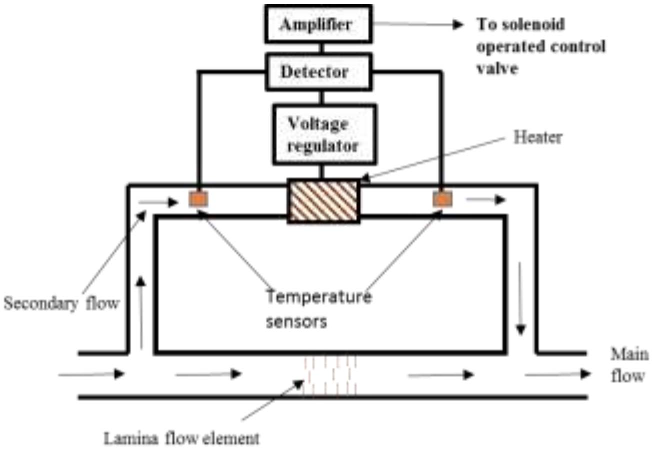

Fig. 2.6 Various components of a typical mass flow controller

$$Qs = Q\ (\text{carrier gas})\ [Ps\ (T) / P_{total}] \quad 2.2$$

where Qs is the molar flow rate of the organometallic source, Q(carrier gas) is the molar flow rate of the carrier gas through the bubbler, Ps(T) is the vapor pressure of the organometallic source at temperature T, and P_{total} is the total pressure inside the organometallic bubbler. In the simplest case, the flow of vapor is controlled by the carrier gas flow. This system can be improved by holding the pressure constant in the bubbler. As a result, the ratio between the carrier gas and the vapor is fixed, stabilizing the output. The flow of vapor can then be kept constant by controlling the carrier gas flow, based on the sensor signal.

Another important part of the main gas panel is the supply of carrier gases within a vent-run configuration. In order to increase the carrier gas consistency, a relatively large flow rate of the carrier gas (typically several liters/min) is maintained in the supply line. The source flow rate of tens or hundreds of cm^3 /min can then be set up and become stable while the valve is vented to a waste line prior to injection into the run supply line, shown in Fig.2.5. As long as a fixed relationship is maintained among the total pressures in all vent and supply lines, transients will be reduced and the actual source flow can be managed.

2.4.3.2 Reaction chamber

Once an appropriate gas mixture has been synthesized, the gases are introduced into the reactor where a substrate is located and a basic pyrolysis reaction takes place. The reactor's design fall within two categories; the vertical and horizontal reactor. Both the reactors are cold-wall systems that cause the basic pyrolysis reactions, both contain a relatively small diameter inlet into a transition region, and both make use of an indirectly heated silicon carbide-coated graphite susceptor. The chamber can be made of quartz, stainless steel, or quartz-lined stainless steel. The

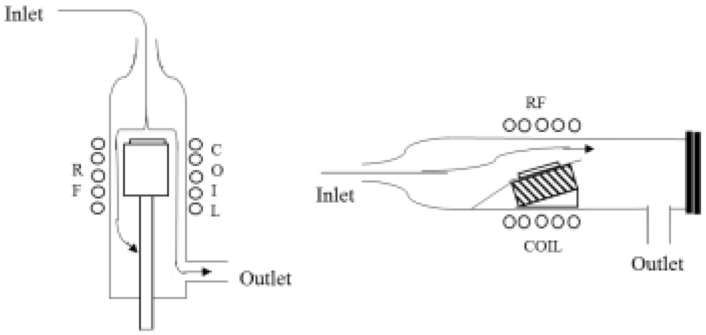

Fig. 2.7 (a) Typical vertical reactor and (b) Horizontal reactor used for MOCVD growth

chief distinction between the vertical reactor and horizontal reactor is the direction of gas flow relative to the substrate surface. In a vertical reaction chamber (Fig 2.7(a)), the process gases enter the chamber from the top, getting deflected by a baffle before moving downward through a cold transition region and finally approaching vertically to the heated susceptor. The flow of the gas is forced to the sides by the susceptor with a velocity profile depending on the geometry of the reactor. Better uniformity of the grown material is obtained by rotation of the susceptor. Exhaust gases escape through the base of the reaction chamber. In the horizontal reaction chamber (Fig. 2.7(b)), the process gases enter from the small inlet and maintain laminar flow over the heated susceptor, which is tilted by a small angle as shown in the figure so that the depletion of the reactants can be taken into account. Uniformity can be improved by incorporating a rotating disk within the susceptor. The multiple-wafer chamber has a region for mixing of the gases above a diffuser that constrains a uniform normal gas flow. A rotating sleeve isolates the heater from the process gases. A multistage heater block is used to introduce a lateral temperature gradient to improve the uniformity of the grown material.

2.4.3.3 Safety

Safety is always an important issue for the design and operation of the MOCVD growth apparatus due to the hazardous sources used. Use of the hydrides such as AsH_3, PH_3, etc. which have high vapor pressure, increases the risk because of their toxicity (TLV:0.05 and 0.3 ppm, respectively [115]). Organometallics are also toxic and pyrophoric, but easier to control as they are liquids at normal temperatures. Moreover, the use of the quartz reaction chambers which are fragile, large volumes of hydrogen gas, high temperatures required for the growth are also increasing the risk factor in the growth process. Such risks can be handled by categorization. Firstly, the access should be limited that means each level of access to potentially harmful materials must be controlled by a higher level of authority with a correspondingly higher level of training. Secondly, thorough training in the safe handling of materials must be required, and emergency-response situations should be taken care of by proper planning. Lastly, a powerful safety infrastructure must be attached to the system, Hazardous gases should be kept in relatively remote areas having proper safety arrangements with automatic cylinder-change hardware and both mechanical and electronic systems for sensing and limiting the flow rate with high precision.

Fig. 2.8 picture of the Thomas swan, presently Aixtron (UK), MOCVD system at SINP, Kolkata

The gas handling system must have a leak-free coaxial tubing with either an inert gas or an appropriate vacuum in the outer tube. The waste gases through the vent lines or the side products should be mixed with the atmosphere through proper filtering of the hazardous gases. Care must be taken for the automatic shutdown of the source gases in the case of a power failure and the backup power is also insufficient.

2.5 The MOCVD system at SINP

The experiments for the growth of the materials were carried out in the metalorganic vapor phase epitaxy (MOVPE) or metalorganic chemical vapor deposition (MOCVD) system (Thomas Swan, now Aixtron, UK) commissioned at the MOCVD laboratory, Saha Institute of Nuclear Physics, Kolkata, a picture of which is shown in Fig. 2.8. This is basically a vertical flip-type showerhead reactor. The showerhead MOCVD reactor was equipped with a showerhead flange and inlets located very close to the substrate. The reactant gases were injected vertically from the showerhead flange with many small holes (in the order of 0.5mm in diameter) toward the substrate. The showerhead distributes the reactant gases uniformly over the substrate and yields a uniform concentration field. Then reactant gases travel across the boundary layer onto the substrate surface through diffusion driven by the concentration gradient. By adopting a close space (roughly 1 cm) between the showerhead and the substrate, the convection component can be suppressed, the gas residing time can be reduced and the reactant gases can be used efficiently. The schematic of the components in a typical vertical showerhead reactor is shown in Fig. 2.9, where h_C is called the ceiling height or electrode gap and D refers to the diameter of the reaction chamber. The values of D and h_C for our MOCVD reactor were 16” and 16.9 mm, respectively. The susceptor can hold three wafers of 2” diameter during each run. The susceptor was made of high quality graphite

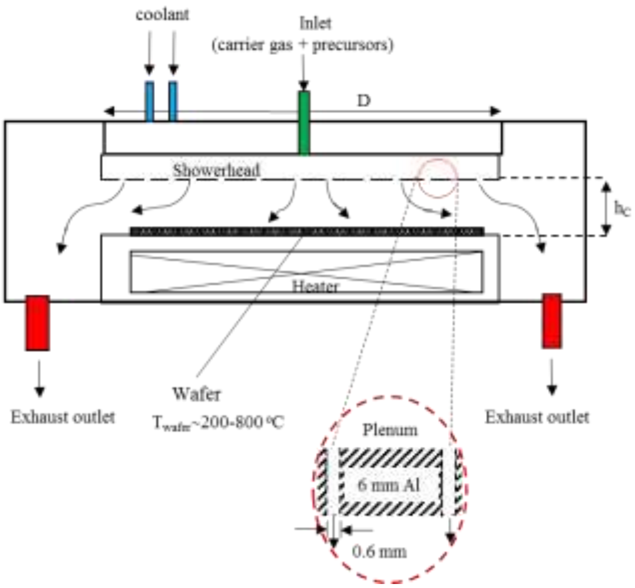

Fig. 2.9 components of the vertical showerhead MOCVD reactor

which was placed on a tungsten heater having three independent heating zones. Each heating zone could be controlled separately to attain uniform temperature across the entire surface, which was extremely important for the uniform growth of the material on the whole wafer. The velocity of the mixture of the source-carrier gas and the growth pressure in the reactor was maintained by a high capacity rotary pump-throttle valve combination. Ultra high pure H_2 gas was used as the carrier with a total flow of 10 lit/min in the two ‘Run’ lines. The susceptor was given a slow rotation of about 50 rpm for uniform growth. The entire reactor was housed in a sealed glove box which was maintained under N_2 environment. The N_2 inside the glove box was under re-circulation through certain media to reduce moisture and oxygen content. The wafers were inserted into the reactor and taken out from it after growth through a load lock chamber connected to the glove box.

Safety and Exhaust

Growth of III-V materials in MOCVD involves pyrophoric metalorganic (MO) molecules as group III precursors, highly inflammable hydrogen gas (carrier), and highly toxic arsine (AsH_3), phosphine (PH_3) gases as group V source. Leakage in any of these gases may lead to an unsafe and hazardous situation. Hence, all the run and vent lines of metal-organics and hydrides, the entire gas mixing cabinet, the reactor cabinet, toxic arsine and phosphine gas cabinet have been periodically checked by helium gas leak detector. In addition to this, leak test has been performed while installing the new sources (MO and Hydrides) and replacing the empty bottles to achieve the desired leak-free environment.

In order to handle the process gases (MO, hydrides and hydrogen), in an emergency or accidental case, MOCVD system has been equipped with exhaust pipe lines, emergency off and process stop buttons. The power supply of MOCVD system is terminated by the EMERGENCY-OFF button in any situation of emergency. Pressing the PROCESS-STOP button leads to the following steps

- All gas lines are purged with nitrogen
- Throttle valve gets closed
- All hydrogen and metal organic source valves are closed
- Process heater is turned off
- Running recipe is terminated

In addition to these safety buttons, phosphine, arsine and hydrogen gas sensors are mounted on the walls, exhaust pipes and gas cylinder rooms. The gas sensors are highly sensitive to the flow rates. It can deduct the gases in the order of parts per million (ppm). Typical alarm levels of all the gases are maintained 30 ppm. If any gas level exceeds this value, the Dräger sensor controllers automatically trigger the alarm and abort the recipe from further progress of the process.

Another important part of the exhaust system is the scrubber. It consists of two tanks which are filled with the cleansing solution. The cleansing solution is basically a mixture of sulfuric acid and deionized water. The gaseous by products are fed into the liquid scrubber. There, the gases are detoxified and the rest is left to the environment through the exhaust. The scrubber has a touch screen controller. The controller alerts when the solution level is low and if there are other problems. The pH value of the solution is maintained at 5. The cleansing solution should be replaced, if there is any sign of crystallization.

Chapter 3

Experimental techniques

3.1 Introduction

The MOCVD grown samples were studied by several structural characterization techniques such as electron microscopy (especially, scanning electron microscopy and transmission electron microscopy) and x-ray scattering (X-ray reflectivity and X-ray diffraction). The optical properties were investigated by employing low temperature photoluminescence. Devices were fabricated with two metal contacts on the front face of the active semiconducting layer using thermal evaporation technique. The effect of light on the device performance was studied through I-V measurements and time response. All these techniques are discussed in the following sections.

3.2 Physical vapor deposition

Physical vapor deposition (PVD) is basically a thin film deposition technique performed in presence of a vacuum [116]. Typically, the air pressure of the chamber during evaporation is maintained around 10^{-6} mbar. For this process, the material to be deposited is placed in a crucible that provides the heat of vaporization with proper vapor pressure. The entire growth process is basically divided into two steps as follows

(i) First melting and then evaporation of the material to be deposited.

(ii) Transport of the vapor through the vacuum and again comes to the condensed phase on the substrate to form a layer.

The air pressure inside the chamber must be below 10^{-5} mbar to achieve uniform film. Among different types of PVD processes, electron beam evaporation (EBE) [117] and thermal evaporation (TE) are two important techniques for thin film deposition [118]. We employed TE for the growth of the contacts on the epilayer of AlGaAs on GaAs using proper masks. The following subsections contain a brief discussion on thermal evaporation technique.

3.2.1 Thermal evaporation

In a PVD process, when the material is melted and evaporated by means of thermal energy through the heating of electrical resistance (in general tungsten filament is used), the technique is called TE. The crucibles are usually made with materials such as tungsten, molybdenum, or tantalum, having a very high melting point and very low vapor pressure. The shape of the crucibles used is in the form of a coil (diameter 0.02 in). Their endpoints are directly connected to the heavy copper or stainless-steel electrodes for the completion of the electrical circuit. In our case, we have always used tungsten crucible during TE.

3.2.2 Experimental setup for TE

Different components of for TE technique are given below. Fig. 3.1 shows a schematic of this setup.

Vacuum pump: Two different types of vacuum pumps are used for reaching the overall vacuum level of 10^{-6} mbar. A turbo pump in conjugation with an oil pump (a rotary pump can also be used) is used to reach and sustain the required vacuum level for the deposition.

Crucible: Molybdenum crucibles are used during EBE. In the case of TE, crucibles are made of tungsten.

Substrate holder: A metal plate for holding the substrate.

Heater: To heat the sample for the deposition of the thin film at high temperature. The maximum achievable temperature is 400^{o} C. It is attached to the substrate holder.

Quartz crystal monitor: For measuring the thickness and growth profile of the grown material.

Tungsten filament: The evaporant is taken inside a filament, normally tungsten is used in case of TE.

Water cooling system: The crucible containing the material is cooled down to keep the effect of electron beam heating limited to a very small region.

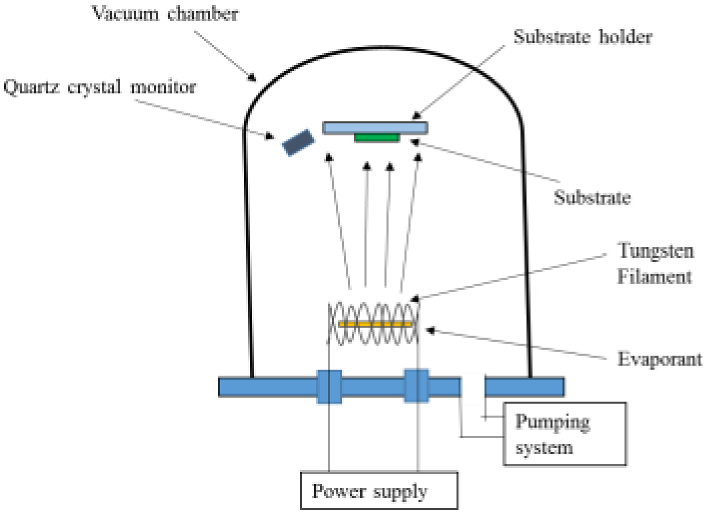

Fig. 3.1 Schematic representation for the experimental set up of thermal evaporation technique

3.3 Structural characterization techniques

There are two types of techniques for the structural characterization of nanomaterial in general. Both destructive and nondestructive techniques can be employed to extract structural information. In case of destructive techniques, sample preparation is an integrated part of the techniques such as cross-sectional transmission electron microscopy in our case. On the other hand, we employed X-ray scattering also which are faithful nondestructive techniques for the evaluation of various parameters of the grown structures.

3.3.1 Electron microscopy

The spatial resolution of optical microscopes is limited to a few micro-meters due to the diffraction limit of light. Probing the surface and the atomic structure of materials with a higher resolution beyond the wavelength of light, up to a few nm towards Å, is very important not only to look into the inside of the material but also to understand its macroscopic properties. Electrons can be accelerated to gain sufficient energy to possess the de Broglie wavelength well below that of light. The fact makes them an eligible candidate for studying materials in the nanoscale regime.

3.3.1.1 Scanning electron microscopy

Scanning electron microscopy (SEM), fulfilling the criterion for better resolution, serves as a powerful and popular technique for imaging the surfaces of almost any material with a resolution down to about 1nm. The image resolution offered by SEM depends on the properties of the electron probe and also on the interactions between the electrons and the specimen. The interaction of an incident electron beam with the specimen produces secondary electrons, the emission efficiency being dependent on surface geometry, surface chemical characteristics and bulk chemical composition [119,120]. SEM can thus provide information about the surface morphology and also the chemical composition. The SEM measurement unit consists of an electron gun as the source of electrons, a high electric field across the electrodes for accelerating the electrons, a system of electromagnetic lenses which focus the beam of electrons onto the sample, scanning coils facilitating the scanning of the electron beam over the sample surface, the sample chamber where the sample is located, and detectors that measure the signals generated from the interaction of the electrons with the sample. All these components are kept within a vacuum chamber to prevent unwanted scattering of the electrons. Fig. 3.2 shows a schematic diagram illustrating the major components for the formation of the image in SEM. There exist two types of electron source (or electron gun), one is based on thermionic emission and the other field emission. A thermionic electron gun relies on electrons emitted from a heated filament. Usually, a tungsten filament serves as the cathode. On the other hand, in the case of the field emission electron gun on electrons emitted from a sharp tip upon the application of a high electric field. Instead of the heating of a filament, here as soon as a high electric field is applied to the tip, electrons from the tip quantum mechanically tunnel through the energy barrier into the vacuum. Typically the field emission gun has two anodes. The first anode (at ~ 0 –5 kV) serves to extract the electrons from the tip, while the second anode (at ~ 1–50 kV) serves to accelerate the electrons and this determines the energy of the electrons traveling down the column to the specimen. The field emission electron gun has a higher brightness as compared to the thermionic electron gun. As the electrons are streaming out from the electron gun, they form a spray pattern. In order to control the profile of this electron beam into a finely adjusted focused beam, electromagnetic lenses are used. When an electron with charge *e* and velocity *u* travels in a region with a magnetic field *B*, it will experience a force *F* given by

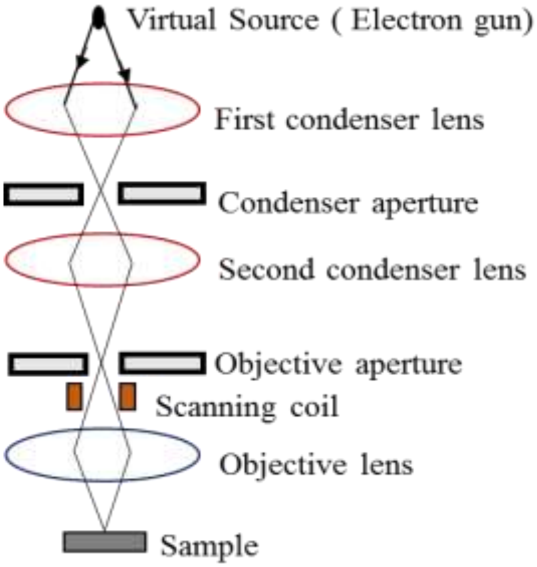

Fig. 3.2 Major components of SEM apparatus for the formation of an image

$$F = e u \times B \qquad 3.1$$

The only effect of the magnetic field is to change the direction of the motion of the electrons. The magnetic field profile generated by a typical electromagnet used in an SEM apparatus is highly non-uniform. The magnetic field of the electromagnetic lens system can be considered to be made up of two independent components, the vertical axial component (H_z) and the horizontal radial component (H_r). The radial component causes the electron traveling in the *z*-direction to move in a helical manner with respect to the central axis. The axial component causes the electron to move closer to the central axis, i.e., the effect of the axial component is to reduce the diameter of the helical path of the electrons. As a result, the electron beam spirals down the column as it passes through the electromagnetic lens and becomes finely focused on the sample for imaging purposes. There are usually two such electromagnetic lenses in the SEM system, the condenser lens and the objective lens. The condenser lens provides the first focusing effect and guides the electrons traveling through the SEM column. The objective lens focuses the electron beam onto the sample surface. The focal length of the objective lens is denoted as the working distance of the microscope. The scanning of the electron beam over the surface of the sample is achieved by deflecting the beam using an applied electric field or magnetic field. Typically a deflection coil consists of four radially oriented coils arranged so that the magnetic field is perpendicular to the axis of the system. The magnetic field generated by these coils can be controlled by the amount of electric current passing through these coils. By programming these scanning coils, one can readily raster the electron beam over the sample surface. The typical accelerating voltage used in SEM is of the order of a few thousand volts.

With an energetic beam of electrons scanning over the sample surface, a number of phenomena such as the production of secondary electrons (SE), backscattered electrons (BE), auger electrons (AE), x-ray photon emission and cathodoluminescence (CL) occur due to the interaction between the electrons and sample atoms [121]. Among them, SEs are the most abundant and they are commonly used as imaging signals in SEM. Fig. 3.3 illustrates the phenomena that are observed when an energetic electron beam is incident on a typical sample. Energetic incident electrons can collide with the electrons in the sample and knock them out of their usual orbitals. These electrons are known as secondary electrons (SE). During the process, the incident electrons lose little energy

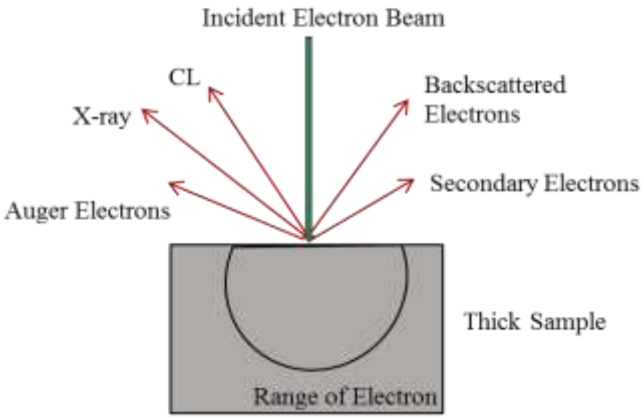

Fig. 3.3 Detectable signals generated when an energetic electron beam is incident on the sample in SEM

and continue to generate more SE as they traverse further into the sample. A single incident electron will typically generate a shower of thousands of SE before losing its energy. Since a large number of SE are generated, the detection of SE is the most common mode of operation for SEM sample imaging. Note that the SE have low energies so that SE generated deep in the sample are unable to travel to the surface and consequently unable to contribute to the formation of the image. So, the SE detected are primarily from the region close to the sample surface (<10 nm). Hence SE imaging would produce good topographical information of the sample. The SEM generates an image of the sample by scanning the electrons over the sample surface while a SE detector placed near the sample collects the signal generated. In SEM, operating at a higher magnification means scanning the focused electron beam over a smaller area of the sample. Naturally, when the magnification reaches a high value, more effort is required to obtain a high quality image. The quality of the image also depends on the type of sample being imaged too. The SEM requires a vacuum environment in order to function properly. If a poor vacuum is maintained in the system, air molecules can cause the electron source to burn out. The electron beam would also be scattered by the air molecules in the chamber. The collision between the electrons and the air molecules could give rise to ionization and discharge. The stability of the beam and the quality of the images would be affected. The presence of air molecules in the SEM system can result in chemical reactions between the sample and the molecules. The result is the formation of some compound on the sample. This will affect the quality of the image too.

3.3.1.2 Transmission electron microscopy

Transmission electron microscopy (TEM) is an efficient structural and chemical characterization tool with high spatial resolution. Historically, the development of the electron microscope actually started with the invention of the electron microscope by Knoll and Ruska in 1933 [122]. In TEM, the voltage used to accelerate the electrons, typically in the range of 200 to 300 kV, is much higher than that used in SEM. At such high energies, the electrons are able to pass through the sample that is made thin deliberately. The de Broglie wavelength of such energetic energy electrons would be very short, which means that the detection of features in a relatively smaller length scale is possible through TEM as compared to SEM. High-Resolution TEM (HRTEM) is now routinely used to see various atomic planes and domains in single-crystalline and polycrystalline samples. However, it is a destructive technique and a lengthy sample preparation is usually required to make the sample thin enough for the electrons to pass through. Since the beam is traveling through the sample, the sample bulk and not the surface is being imaged. A modern apparatus used for TEM has the capability to directly image atoms in crystalline specimens at resolutions close to 0.1 nm, smaller than interatomic distance. An electron beam can also be focused to a diameter smaller than ~ 0.3 nm, allowing quantitative chemical analysis from a single nanocrystal. This type of analysis is extremely important for characterizing materials at a length scale from atoms to hundreds of nanometers. TEM can be used to characterize nanomaterials to get information about particle size, shape, crystallinity and other structural information.

The working principle of TEM is very similar to that of SEM. Fig. 3.4 shows a schematic of the important components used for the image formation in a typical TEM apparatus. Similar to SEM, an electron gun producing the stream of monochromatic electrons, is typically located at the top of the instrument. This stream of electrons is focused on a coherent beam by the condenser lenses 1 and 2 as indicated in Fig. 3.4. A condenser aperture is employed to restrict the beam and exclude the high angle electrons that deviate from the main optic axis of the system. It is important in this case that the specimen should be thin enough to allow some electrons to transmit through the sample. Electrons suffer both elastic and inelastic scattering during the interaction between the electron beam and specimen and the undeflected electrons traverse in the forward direction. The

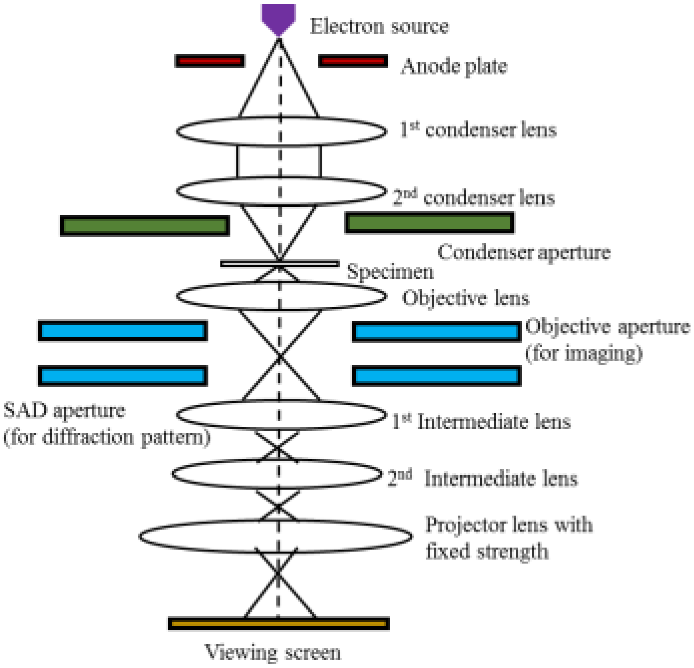

Fig. 3.4 Schematic representation of the major components for TEM

final signal at the detector contains all the information about the sample. The beam of electrons strikes the specimen and a part of it is transmitted. The transmitted electrons are then focused by the objective lens into an image. The objective and selected area apertures are utilized depending on the mode of operation. The two basic operations of the TEM system are image formation and diffraction pattern. During the imaging mode, the objective aperture is utilized to enhance contrast by blocking high-angle diffracted electrons. During the diffraction pattern mode, the selected area aperture is engaged and facilitates the examination of the diffraction of electrons caused by the interaction of the electrons with the ordered arrangements of atoms in the sample. The emerged electrons then pass through the intermediate and projector lenses before striking the viewing screen to either produce an image or diffraction pattern. In the bright field imaging mode, the darker areas of the image represent those areas of the sample that fewer electrons are transmitted through (thicker or denser); the lighter areas represent those areas that more electrons are transmitted through (thinner or less dense). When the incident electrons strike the sample, the usual phenomena found in SEM such as SE, BE, AE, X-ray, CL are generated as previously discussed. However, in the case of a TEM, since the sample is thin, electrons pass through the sample. Fig. 3.5 shows the schematic of the signals generated when an incident electron beam strikes a thin sample in TEM. The electrons that pass through the sample may scatter elastically, inelastically or remain unscattered. The unscattered electrons are incident electrons that pass right through the thin sample without any interaction with the sample atoms. The transmission of such unscattered electrons is inversely proportional to the thickness of the sample: The thicker the sample, the fewer the transmitted electrons and vice versa. Therefore the thicker parts of the sample appear darker while the thinner parts of the sample appear lighter. When the incident electrons are deflected due to their interaction with the sample but with no loss of energy, this gives rise to elastically scattered electrons. During the elastic interaction, incident electrons are scattered according to Bragg's law of diffraction by atoms with a regular arrangement. The scattered electrons are collected using

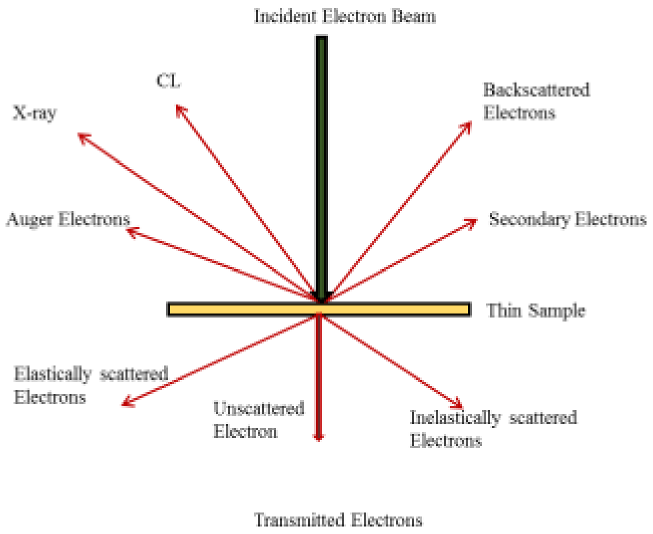

Fig. 3.5 Detectable signals generated when high energetic electron beam is incident on a thin sample in TEM

magnetic lenses to form a pattern of diffraction spots. These diffraction patterns can be used to identify the crystalline order of the sample, giving information about the orientation, and atomic arrangement in the area probed.

TEM specimen preparation

Undoubtedly, TEM is a powerful technique for microstructure and composition analysis, but it needs special attention for the specimen preparation. As the highly energized electrons have to be transmitted through the sample, so direct insertion of the sample in any form is not possible. The liquid sample can be inserted by drying them on a carbon coated copper grid but the solid sample is to be made electron transparent following the steps described below.

Initial thinning

The general lateral dimension of the specimen used for TEM is 3 mm in diameter. So a nearly about 3 mm diameter disc is cut from the sample using a disc grinder (Gatan). With the help of a silicon carbide paper, they are thinned to the appropriate thickness for dimpling. Care should be taken such that no crack is introduced, otherwise, the sample could be broken at any of the later stages.

Dimpling

After the initial thinning, the central portion of the sample is dimpled to reduce its thickness more. At the time of dimpling, as a small portion of the sample is made thinner, the chance for breaking of the sample is diminished. After that, the sample is placed on the turntable of the dimple grinder rotating at a constant speed. The grinding wheel is rotated orthogonally to the turntable rotation. Its speed can be varied according to the hardness of the sample. While dimpling, a diamond paste of grain size 3µm is applied on the sample, dimple thickness was set and then the grinding wheel is lowered on the sample. After dimpling, the final polishing is done with a 0.25 µm grain size diamond paste.

Ion milling

The mechanical thinning as described previously is not enough to make the sample electron transparent. A Precession Ion Milling System (PIPS) (Gatan, Pleasanton, CA model) has been used for this purpose. In a PIPS, generally, Argon ions are impinged on the dimpled sample to knock out atoms from it to make it electron transparent. A CCD attachment in conjugation with an LCD is used to monitor the sample inside the chamber. In our present ion milling system, the energy of the ions can be varied up to 6 KeV and the angle of incidence can be varied up to $\pm 10^{o}$. The electron transparency of the sample is confirmed when a tiny perforation appears in the dimpled region, which can be viewed in the LCD.

Sample preparation for cross-sectional TEM

The cross-sectional view in TEM is necessary to extract the detailed structural parameters of epitaxial layers. For the layers deposited on semiconductor substrates (Si, Ge, GaAs), at first two pieces of the sample of less than 3 mm width are cut and bonded with epoxy, keeping the deposited or the treated side face to face. For this purpose, Gatan Epoxy, which consists of two parts, a resin and a hardener, is used. They are mixed in 8:1 (resin: hardener) ratio. After the epoxy is applied to the sample, it is heated at 120 ^{o}C to get strong adhesion. Now the composite is inserted into a brass tube and the empty place is filled with thin dummy substrates and epoxy. The sample contained inside the brass tube is cut to make 0.5 mm discs, using a diamond wire saw. The disc is now mechanically thinned to 60-100 μm as described earlier, with the disc grinder and silicon carbide paper of different grit size. The central portion of this thin sample is now dimpled down to 30μm thickness and inserted inside the PIPS chamber for ion milling. After the ion milling, the electron transparent sample for the cross-sectional TEM (XTEM) study is obtained.

3.3.2 X-ray scattering

X-ray scattering techniques have been extensively used as a nondestructive and robust probe for structural and interfacial investigation of thin film complex nanostructures like superlattice, quantum dot, etc. with resolution down to one atomic layer. Although for simple epitaxial layers, the lattice constant, strain as well as the composition can be extracted directly from the experimental data alone, but for complex structures such as multilayer superlattice with cross incorporation of atoms across the interface, to extract various parameters, simulation of the experimental data is necessary. In the grazing angle reflectivity regime, the scattered intensity profile depends on the electron density distribution only in the layer but does not depend on the crystal structure. It is sensitive to surface, interface roughness, interdiffusion at the interfaces whereas, in the high angle regime, the intensity profile is sensitive to the atomic arrangements in the crystal. So, information about the crystalline quality, difference in lattice constants at the interface, strain profile, composition (applying Vegard's law) can be obtained from x-ray diffraction analysis [22].

3.3.2.1 X-ray reflectivity

XRR is a useful technique for characterizing thin film and multilayer structures. In the low angle regime, up to the critical angle, X-ray does not enter inside the sample suffering total external reflection. As the grazing angle of incidence is increased beyond the critical angle, X-ray starts to penetrate the surface of the sample and interference between two rays reflected from the air-film interface and the film-substrate interface would give rise to fringes bearing the information of the sample. Typically, a reflectivity measurement is done in θ-2θ configuration for an incidence angle up to ~ 6^{o} to extract the depth profile of the electron density [123]. Fig. 3.6(a) demonstrates a typical geometrical arrangement of the x-ray source, specimen and detector used in the laboratory for reflectivity measurements in θ-2θ configuration. A schematic representation of the experimental arrangement using synchrotron radiation is shown in Fig. 3.6(b).

3.3.2.2 X-ray diffraction

X-ray diffraction (XRD) is a powerful and routine nondestructive technique for determining the crystal structure as well as the phase present of crystalline materials. When X-ray of a certain wavelength λ passes through the periodic planes of atoms (Fig. 3.7) the diffraction angle θ at which constructive interferences are detected is given by the Bragg's law

$$\lambda = 2d_{hkl}sin\theta \qquad 3.2$$

Here, d_{hkl} is the inter-planar spacing between consecutive (hkl) planes and is given for the cubic crystals of lattice parameter *a* as:

$$d_{hkl} = \frac{a}{\sqrt{h^2+k^2+l^2}} \qquad 3.3$$

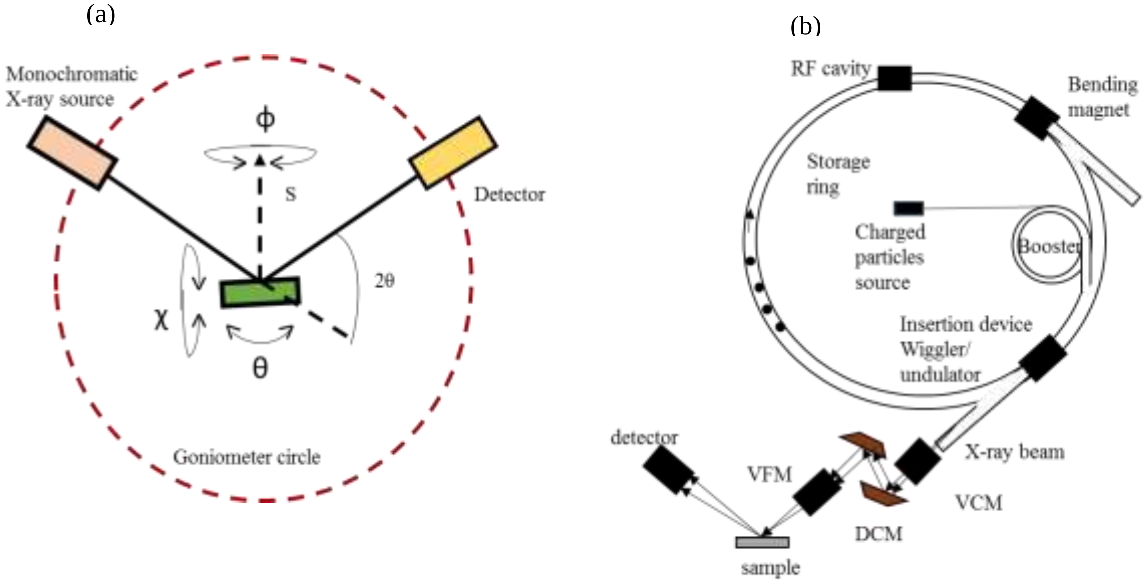

Fig. 3.6 (a) Arrangement of the X-ray source, sample and detector in a typical lab based setup for X-ray scattering measurements (b) Various components for synchrotron radiation source along with the experimental setup

The most widely used x-ray diffraction technique in materials characterization was originally used for examining the crystal structure of powder samples and thus, traditionally it is called x-ray powder diffractometry [124]. In fact, polycrystalline aggregate solids other than powder are commonly examined by this technique. In the x-ray diffractometer, a monochromatic x-ray beam is used to examine specimens to a dimension of a few angstroms. By continuously changing the incident angle of the x-ray beam, a spectrum of diffraction intensity versus the angle between incident and diffraction beam is recorded. The basic function of a diffractometer is to detect the amount of X-ray scattered from materials in different directions and produce the diffraction intensity as a function of the diffraction angle (2θ). X-ray source, specimen and detector are arranged in the same way as given in Fig. 3.6(a). X-ray sources can be common laboratory sources depending on different target materials such as Cu, Mo, etc. Synchrotron radiation is used nowadays as well focused, stable, high intensity versatile X-ray sources. In the laboratory-based diffractometer, relative movements among the x-ray tube, specimen and the detector ensure the recording of diffraction intensity in a range of 2θ. Note that the θ angle is not the angle between the incident beam and the specimen surface. In the case of symmetric scans, it is the angle between the incident beam and the crystallographic plane that generates diffraction as the planes we look for are parallel to the sample surface. In asymmetric scans, the planes of interest are not parallel to the surface. Diffractometers can have various types of geometric arrangements to enable the collection of X-ray data. The majority of commercially available diffractometers use the arrangement, in which the X-ray incident beam is fixed, but the sample stage rotates around the axis perpendicular to the plane of incidence in order to change the incident angle. The detector also rotates around the axis perpendicular to the plane of incidence but its angular speed is twice that of the sample stage in

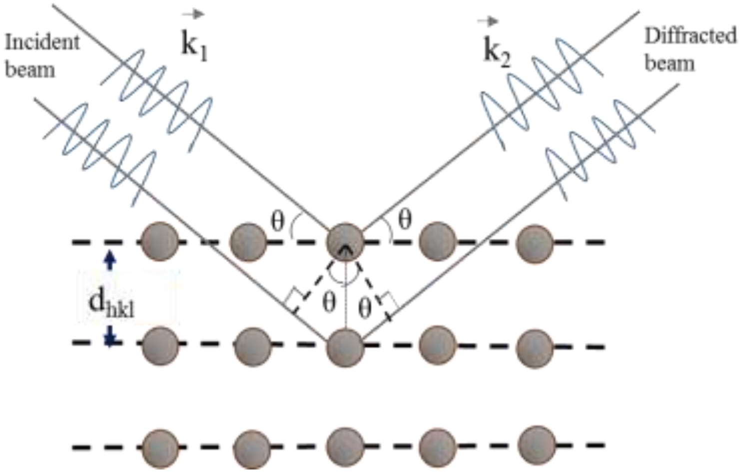

Fig. 3.7 Bragg's representation for diffraction of X-ray from atomic planes

order to maintain the angular correlation of θ–2θ between the sample and detector rotation. Here, we mainly perform the θ-2θ scans for (200) and (400) symmetric reflections to monitor the satellite peaks around the main Bragg as a signature of the superlattice structures. The high-resolution x-ray θ-2θ scans were performed at Indian Beamline, BL-18B at Photon Factory, Japan. The wavelength of the x-ray is 1.08887 Å. We performed experiments with the same setup discussed above as the direction of the beam is fixed in synchrotron experimental setup. The high resolution x-ray θ-2θ scans were performed around the weak (002) and allowed (004) Bragg position. The sample was mounted onto an 8-circle goniometer (Huber, Germany) at the focal point of the focusing mirror of the beamline. The sample was mounted horizontally and the scattered beam was collected by a single channel scintillation detector mounted at a distance of 380 cm onto the 2 h arm of the goniometer. A slit of 1.5 mm (horizontal) by 0.25 mm (vertical) was mounted just before the detector to increase the signal-to-background ratio. For the high temperature real-time XRD measurements, the sample is heated under a graphite dome, in presence of $N_{2,}$ with As overpressure to avoid As desorption and consequent degradation of the surface.

3.3.2.3 X-ray source

X-rays are generated by electronic energy transitions in a solid (laboratory source) or in a confining magnetic field (synchrotron source). For the reflectivity and diffraction experiments, both X-ray tubes and synchrotron X-rays can be used. After the discovery of X-ray in 1895 by Rontgen [125], the developed tube X-ray was the only source of X-ray till 1970s for application in diverse fields like medical science, crystallography, material science, etc. In the 1970s, since the realization of the synchrotron radiation, which is emitted from charged particles circulating in a storage ring under magnetic field, several efforts are made to use it for high energy nuclear physics experiments and also other fields of science [126,127]. Synchrotron is potentially much more intense and versatile source of X-rays compared to the lab sources. Many storage rings have been constructed now around the world dedicated solely to the production of X-rays.

Lab source

In case of an X-ray tube, normally electrons are produced from a filament by thermionic emission. The accelerated electrons move towards the water-cooled anode. The high voltage and the current can be varied independently, and the limitation of the intensity of the radiation coming out is set only by the cooling efficiency. However, the rotating anode method is a relatively better alternative for the dissipation of heat over a larger volume, and to increase the total power. The spectrum of the X-ray generated from an X-ray tube is comprised of two components: continuous bremsstrahlung radiation due to deceleration of the electrons at the anode and a discrete characteristic part which is due to de-excitation of the excited electrons in the shells of the anode material [128]. For X-ray related experiments using a monochromatic beam, one of the characteristic line, K_α, which is several orders of magnitude more intense than the bremsstrahlung radiation, is chosen. However, only a small fraction of the total number of photons emitted can be utilized in a beam which requires an angular divergence of a few squared milliradian. In addition, as the X-ray tube source is not continuously tunable, it is not always possible to have the optimal wavelength for a particular experiment as desired. On the contrary, X-rays generated from synchrotron sources do not face such difficulties, and have a brilliance which is enormously higher than that of standard laboratory sources.

Synchrotron radiation (SR)

Synchrotron is basically a special kind of particle accelerator. The synchrotron radiation is the radiation emitted from charged particles traveling at relativistic speeds in presence of the applied magnetic field. The particles, electron or positron are compelled to follow a curved trajectory depicted by the magnetic field. Synchrotron radiation is produced in storage rings where the charged particles are kept circulating with a finite constant energy. In a storage ring, the synchrotron radiation is produced either using bending magnets generating a constant magnetic field or by insertion of devices like wigglers or undulators giving an alternating magnetic field. In these devices, the alternating field forces the charged particles to follow oscillating paths rather than moving in a straight line. In a wiggler, the amplitude of the oscillations remains large, and the radiation from different wiggles superimpose incoherently, whereas, in undulators, the small amplitude oscillations from the passage of a single electron add up in a coherent fashion to give the resultant radiation. The divergent white beam is passed through a set of slits, a vertical collimating mirror (VCM), a double crystal monochromator (DCM), a vertical focusing mirror (VFM) under proper vacuum and cooling system to obtain a monochromatic, focused, horizontally and vertically squeezed beam that can be used for various X-ray scattering experiments. A schematic representation of a synchrotron radiation source is shown in Fig. 3.6(b), as mentioned earlier. We have carried out measurements using SR at BL-18B, photon factory, Japan and also BL-13, INDUS-2, RRCAT, Indore.

3.4 Optical characterization technique

3.4.1 Photoluminescence spectroscopy

Photoluminescence spectroscopy is an efficient nondestructive method to probe the electronic structure of materials as a macroscopic phenomenon. Electromagnetic radiation of desired wavelength is directed onto a sample, where it gets absorbed. One possible way this absorbed energy can be dissipated, is through the emission of light, or luminescence. In the case of photo-excitation, this luminescence is called photoluminescence. Photo-excitation causes electrons within a material to move into permissible excited states. When these electrons return to the lower energy states, the energy can be released through emission of light via radiative recombination or lost nonradiatively by heating effect. The energy of the emitted light (photoluminescence) relates to the difference in energy levels between the two electronic states involved in the transition between the excited state and the equilibrium state. The quantity of the emitted light is related to population density of the carriers involved in the process. Photoluminescence is primarily a three step process.

i. Creation of electron-hole pairs by absorption of the exciting light.

ii. Radiative recombination of electron-hole pairs.

iii. Escape of recombination radiation from the sample.

It is a process in which an optically active material is excited through a photon, typically having higher energy than the bandgap and then analyzing different luminescence transitions in the form of a spectrum. The transition can take place either through the fundamental gap or via different

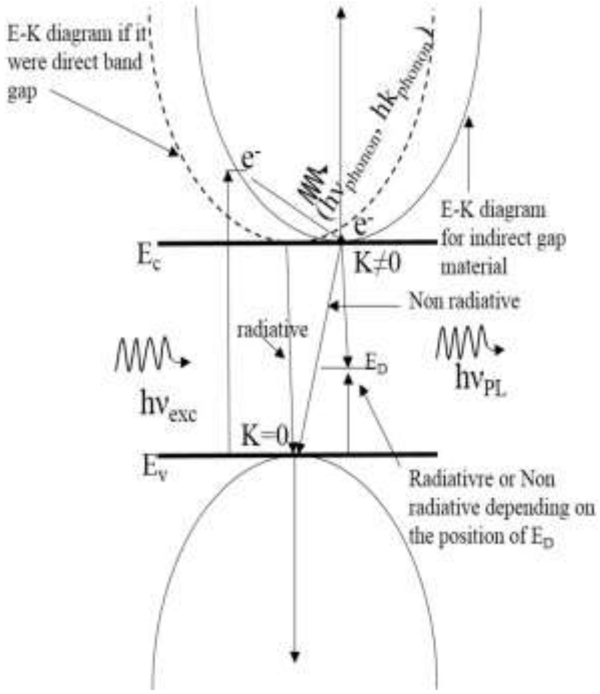

Fig. 3.8 Radiative, non radiative, defect assisted transitions in case of direct and indirect gap materials

defect states. The possibilities of radiative or non radiative transitions in case of direct gap and indirect gap materials are illustrated in Fig. 3.8. It is an important technique for measuring the purity & crystalline quality of semiconductors and for the quantification of the amount of disorder present in the system. Photoluminescence is also very useful for determination of bandgap, impurity level, defect detection, recombination mechanism & material quality of the semiconductor.

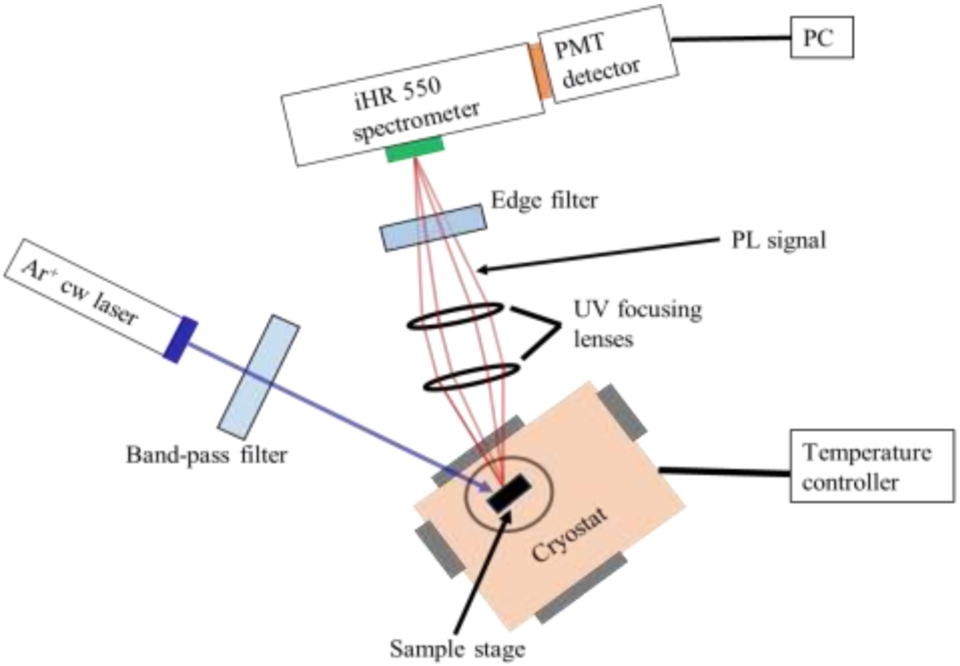

Fig. 3.9 Experimental set up for the temperature dependent photoluminescence measurement

3.4.2 Experimental setup

The schematic of the experimental setup for photoluminescence measurement is shown in Fig.3.9. The basic components are as follows:

i. **Excitation source**: Melles Griot series Ar^+ laser with excitation power of 100 mW operating at 488 nm was used as the excitation source. The laser beam is linearly polarized and the beam diameter is 1.79 mm.

ii. **Line filter or Band pass filter**: Band pass filter for 488 nm wavelength was used for our setup to eliminate other laser lines except the desired one.

iii. **Sample stage**: sample stage with X-Y-Z translation associated with a sample holder was used for mounting the sample.

iv. **Collection optics**: Two UV quartz lens with 40 mm and 60 mm focal length were used to collect the PL emission from the sample to the monochromator.

v. **Edge filter**: This filter is used before the monochromator to block the laser line and pass the higher wavelength.

vi. **Spectrometer**: Horiba Jobin Yvon iHR series spectrometer was used for our PL setup. iHR-550 spectrometer is automated, triple grating spectrometers with a 550 nm focal length (f/6.4 aperture) equipped with a photomultiplier tube (PMT) detector for the wavelength range of 185-900 nm and a cooled InGaAs detector with two stage thermoelectric cooling for the range of 800-1700 nm. The spectral range of this spectrometer is 150 nm to1500 nm with 1200 rulings/mm grating and resolution is 0.025 nm.

For low temperature (up to 4 K) PL measurements, we use a closed cycle He cryostat (Janis Research Co. Inc., SHI- 4). The sample is mounted on a copper sample holder in a cryostat, which allows the measuring temperature to be adjusted from about 4 K to room temperature. A vacuum of about 10^{-6} mbar is maintained inside the chamber with the help of a turbo pump. The resulting luminescence is collected through two lenses and a coupled Horiba Jobin Yvon iHR-550 series spectrometer by which the luminescence is then spectrally dispersed. After that, the dispersed luminescence is detected by PMT that is suitable for detecting light from near-UV to 900 nm. The signals produced by the PMT are recorded and processed by computer system through an interface.

3.5 Electrical characterization

3.5.1 Spectral response

The current-voltage characteristics (I-V) were measured for the devices fabricated under dark and in presence of light to study the effect of light on the device performance. Model electrical circuits were involved to see the effect of the device parameters on light. Three figure of merits were calculated and spectral response were studied. The components are given below.

1. Excitation Source: Horiba Jobin Yvon Fl1039/40 xenon lamp with an output power of 450 W, used as the excitation source. Its output spectra cover a spectral range from 150 nm to 1500 nm.

2. Monochromator: Gemini 180, double additive grating scanning monochromator, used to disperse the radiation coming out from the xenon lamp. The radiation emitted from the monochromator illuminated the device.

4. Sample Holder: A platform capable of translation in X-Y-Z directions along with a holder for the sample mounting.

5. Source Meter: The current-voltage (I-V) characteristics of the sample under dark and in presence of illumination were carried out by the Keithley 4200 SCS.

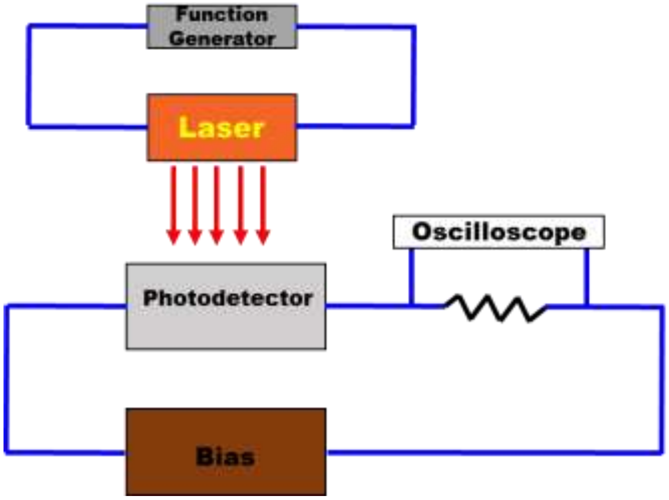

Fig. 3.10 Circuit diagram for the measurement of temporal response of the photodetector

3.5.2 Temporal response

The time response of a photodetector to switching frequency determines its capability to follow a fast-varying optical signal. For temporal measurements, the laser is powered by an ultrafast function generator to produce an optical pulse of desirable frequencies. Tektronix TBS2102 digital storage oscilloscope (DSO), used to measure the response in the form of a voltage across the resistance chosen properly to maximize the photocurrent. The arrangement for measuring the temporal response is shown in Fig. 3.10.

Chapter 4

Observation of the spontaneous superlattice structures in MQW and bulk AlGaAs

4.1 Introduction

Epitaxial growth of II-III-V-VI ternary or quaternary heterostructures on suitable substrate materials either by MBE or MOCVD provides a huge scope to play with the structural as well as the optical and electrical properties by simply changing the composition of the alloy. The III-V semiconductor technology based on GaAs, has received much attention due to its superior optoelectronic properties and flexibility in fabrication of nanostructures [129]. Multi-quantum well (MQW) and artificially fabricated superlattice structures have delivered the role of active region for improvement of the device performance over bulk owing to their continuum sub-band formation [104]. The GaAs based quantum well, superlattice or quantum dot structures are used as an active part of the tandem solar cell to enhance its efficiency [130]. One of the widely used III-V material systems, AlGaAs/GaAs is very much useful in device fabrication due to its high flexibility in bandgap engineering and negligible lattice strain. Its large conduction band offset is desirable in the active region of the quantum cascade lasers due to the suppression of the thermally activated processes that could limit the device performance at high temperatures [131]. The quantum confinement in the QWs depends on the potential barrier which is a function of the alloy composition ‘x’ of the $Al_xGa_{1-x}As$ barrier layer. On the other hand, the QW superlattice structures are grown to form “minibands” for applications such as quantum well infrared photodetector and quantum Cascade laser [132]. Most of the device structures involving $Al_xGa_{1-x}As$ with varying alloy composition ‘x’ are grown on (100) GaAs substrates by epitaxial techniques like MOCVD. Since optical emission property, carrier mobility, band alignment etc. are affected strongly due to superlattice ordering, device characteristics involving $Al_xGa_{1-x}As/GaAs$ (100) material system with such structures would also be significantly modified.

4.2 Growth of the material

4.2.1 Growth of GaAs/AlGaAs quantum wells on (100) GaAs substrates

A thick GaAs buffer layer was-grown on conventional (100) semi-insulating (SI) GaAs substrate to minimize the crystal defects and misfit dislocations in the quantum well structures. Trimethylgallium (TMG) and Arsine (AsH_3) were used as group III and group V sources, respectively. TMG bubbler was kept at 5 °C and its vapour was carried to the reactor through ultrapure H_2 gas (carrier gas). AsH_3 was kept at high pressure cylinders. The GaAs buffer layer was-grown at 650 °C. Initially, the growth temperature was increased at a rate of 40 °C/min. AsH_3 was introduced into the reactor chamber at 400 °C to maintain high overpressure of As to suppress As desorption from the surface during growth. The AsH_3 and TMG flows during the growth were stabilized at 8.91×10^{-3} and 1.41×10^{-4} mol/min, respectively. The values resulted in a V/III ratio of 63.2. The layer was-grown for the duration of 90 min. After the growth of the buffer layer, three quantum wells with nominal thickness 45, 65 and 85 Å were grown separated by the barrier layers of 400 Å of AlGaAs with nominal Al concentration of 0.3. Trimethylaluminium (TMA) was used as the Al source for the growth of the barrier layer. Details of the growth is given in Table 4.1.

4.2.2 Growth of $Al_xGa_{1-x}As$ on (100) GaAs

As we shifted our attention towards the ordering phenomenon in AlGaAs, a thick $Al_xGa_{1-x}As$ layer was-grown on semi-insulating (SI) GaAs substrate with conventional (100) orientation to distinguish the effect of ordering in the material. TMG and TMA were used as group III sources while Arsine (AsH_3) was used as group V source. TMG and the TMA bubblers were kept at 5 °C and 17 °C, respectively. The molar flow of TMG, TMA and AsH_3 were 3.32×10^{-5}, 6.02×10^{-6}

and 2.68 × 10^{-3} mol/min, respectively, giving a V/III ratio of 68.2. The growth temperature and growth time were 650 ^{o}C and 35 min, respectively. A thin buffer layer of GaAs was grown before the onset of growth of AlGaAs layer. The growth rate was estimated to be about 1.94 µm/hr from the measured thickness of the epilayer. The growth parameters regarding the growth of the GaAs buffer layer and the AlGaAs layer are shown in the Table 4.2. The pressure inside the reactor was kept at 76 torr (1/10 atm).

Table 4.1 Growth parameters for the GaAs/AlGaAs MQW

Growth parameters	GaAs buffer	AlGaAs barrier	GaAs QW1	GaAs QW2	GaAs QW3	AlGaAs cap
Layer time (s)	480	73	15	23	31	146
Reactor temp (^{o}C)	650	650	650	650	650	650
AsH_3 (mol/min)	1.79E-3	1.79E-3	1.79E-3	1.79E-3	1.79E-3	1.79E-3
TMGa (mol/min)	1.86E-5	1.86E-5	1.86E-5	1.86E-5	1.86E-5	1.86E-5
TMAl (mol/min)		2.01E-5				2.01E-5
V/III ratio	96	46.2	96	96	96	46.2
Layer thickness (µm)		0.04	0.0035	0.0055	0.0075	0.08
Growth rate (µm/h)	0.84	1.97	0.84	0.86	0.87	1.97

4.3 Structural characterization

4.3.1 TEM study

A set of samples of AlGaAs/GaAs MQW structure with three GaAs quantum wells of thickness 35, 55 and 75 Å, each well sandwiched between AlGaAs barrier layers of thickness 400 Å with nominal Al composition of 0.3, were grown by MOCVD technique. When we looked at the sample after growth through cross sectional transmission electron microscopy (XTEM) as given in Fig. 4.1(a), we have got the thicknesses of the well and barrier layers as expected and in addition, there was a clear alternative repetitive brightness contrast visible in the AlGaAs barrier layers, which seemed interesting as ordering in this material is quite unusual due to small bond length difference between its constituent binaries [11]. Although the flux of the precursors were kept constant during the growth of the barrier layer in the MQW structure to obtain a constant composition throughout the layer, the periodic variation of brightness in the XTEM image suggested a natural formation of compositional modulation in the layer. From High-Angle Annular

Table 4.2 Various growth parameters related to the growth of the GaAs buffer and AlGaAs epilayer in MOCVD

Growth parameters	GaAs	AlGaAs
Layer time	5 mins	35 mins
Reactor temp	650 °C	650 °C
AsH_3 (mol/min)	0.00268	0.00268
TMGa (mol/min)	4.69E-5	3.32E-5
TMAl (mol/min)		6.02E-6
V/III ratio	57.2	68.2
Layer thickness	0.18 µm	1.38 µm
Growth rate	2.20 µm/h (6.11Å/s)	2.37 µm/h (6.58Å/s)

Dark-Field (HAADF) microscopic images (Fig. 4.1(b)), we plotted the elemental mapping across an area including the three QW layers as well as the barrier. A periodic modulation in the Al and Ga concentration could be clearly visible in the barrier region, while the As concentration seemed to be uniform across the entire region. Fig. 4.1(c) showed the concentration plot of Ga and Al along a line in the growth direction. In addition to the three distinct QW layers, there was clear indication of regular variation in Ga and Al concentration in the barrier layer - higher Al concentration region showing lower Ga concentration and vice versa. The interesting feature of such spontaneous ordering in the material led us to study about nature and stability of the ordering in details. Next, to confirm the extent of such ordering in the bulk, we have grown a layer of AlGaAs on GaAs for the same substrate orientation and other growth parameters, but with a different Al composition of 0.15 compared to the MQW to verify whether the ordering exists or not. XTEM of the as-grown sample showed the same kind of ordering of about 5.4 nm. The selected area electron diffraction pattern showed signature of the zinc-blende symmetry of the crystal. In addition, a close look at the Bragg spots in the SAED pattern revealed extra satellite spots in the (001) direction near around the main Bragg spots. Fig. 4.2(a) showed the XTEM image

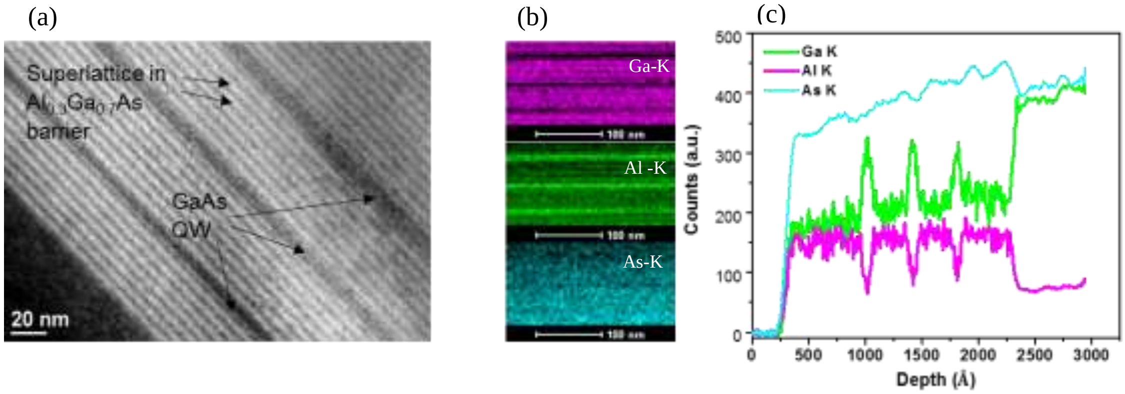

Fig. 4.1 (a) Cross sectional TEM image of the GaAs/AlGaAs MQW showing three GaAs QW layers and an ordered structure in the AlGaAs barrier layers (b) Elemental mapping for the MQW structure for Ga, Al and As (c) Line profile of the constituent elements in the structure

of $Al_xGa_{1-x}As$/GaAs layer with a nominal Al composition of 0.15. Alternate dark and bright lines parallel to the grown surface are clearly visible in the image. The inset in Fig. 4.2(a) showed the brightness contrast plot over the marked line in the figure, where the peaks in the plot correspond to the center of a “bright” layer. While the image did not reveal anything about the crystallinity of the layer, but it clearly indicated the presence of regularly spaced layered structure in the grown epilayer with a characteristic repetition length of about 5.4 nm. The SAED pattern of the grown epilayer is shown in Fig. 4.2(b). The clear and distinct spots indicate high crystalline quality of the grown epilayer with a cubic zinc blende structure. A closer look at an individual spot, as shown in the inset of Fig. 4.2(b), revealed additional satellite spots around the main diffraction spots. These satellite spots, superimposed on the main set of spots correspond to electron diffraction from the layered structures, which could be regarded as natural superlattice structures. Similar superlattice spots have been clearly observed in case of ordered $Ga_{0.5}In_{0.5}P$ epilayers which are well separated from the main diffraction spots [35]. The ordering on monolayer scale in case of $Ga_{0.5}In_{0.5}P$ gives well separated super spots, while those in our case are of comparatively larger length scale bringing the superlattice spots very close to the main spots.

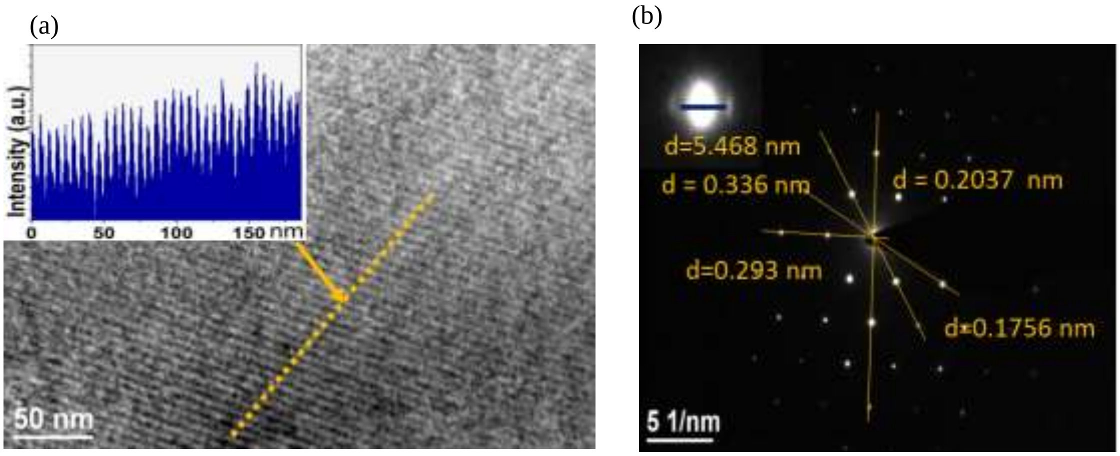

Fig. 4.2 (a) Cross sectional TEM image of the bulk $Al_{0.15}Ga_{0.85}As$ sample showing alternative bright and dark fringes. The intensity profile is shown in the inset. (b) Selected area electron diffraction pattern and appearance of superspots around the main set of diffraction spots (inset).

4.3.2 X-ray analysis

The structural parameters like the compositional profile, the interface roughness of such structure show a strong effect on the X-ray scattered from the material both in low angle and high angle regime. Indirect X-ray scattering techniques seem to be effective in determining the structural modulation in the superlattice layer for low compositional contrast in such length scale since the conventional direct techniques such as transmission electron microscopy or secondary ion mass spectrometry are limited by the instrumental resolution [22]. A combination of low angle reflectivity and high angle diffraction were involved simultaneously to extract the compositional information and to get an overview of the cross-incorporation of the atoms at the interface. X-ray scattering techniques are nondestructive and robust probe for structural and interfacial investigation of such materials, consisting of individual layers of a few monolayer thickness and very low compositional contrast. We need elaborate simulation of the measured data to obtain the composition profile, interfacial diffusion and interface roughness for such complex structure. In the grazing angle reflectivity regime, the scattered intensity profile depends on the variation of refractive index i.e. the electron density only, not on the atomic configuration in the crystal. It is sensitive to surface, interface roughness, inter-diffusion at the interfaces. In the high angle diffraction regime, the intensity profile is sensitive to the crystal structure i.e. the contribution from the atomic planes [123,133]. X-ray reflectivity (XRR) in the θ-2θ mode (q scan) was employed to find out the depth profile of the electron density in the ordered structure under the framework of distorted-wave born approximation (DWBA), and the extracted electron density profile (EDP) was used to provide information regarding composition as well cross incorporation of atoms and interface roughness. The model showed its validity and effectiveness in quite a broad range from Cadmium Arachidate Langmuir-Blodgett (LB) film [134] to artificial Si-Ge superlattice structures [22]. The obtained EDP was then applied to fit the XRD curves of the ordered structure using the kinematical model to extract the stoichiometric information and lattice parameter profile of the superlattice structure. The kinematical theory of x-ray diffraction is suitable when the thickness of the sample is small (in our case less than 1 μm) and can be used safely instead of dynamical theory of x-ray diffraction when layer reflectivity remains below 10% [135]. The method is computationally much simpler and less resource intensive compared to the dynamical theory. Since the $Al_xGa_{1-x}As$/GaAs material system is nearly lattice matched, negligible lattice strain is involved especially for low values of 'x', and the above mentioned method of analysis could be safely used. The formalism has been previously employed to successfully simulate and predict compositional profile and interface roughness of Si-Ge and type-II InAs/GaSb superlattice structures by comparison with the experimental results [22,136]. The precision of the model mostly relies upon judicious guess of superlattice period, separate layer thicknesses in each bilayer, total film thickness etc. High Resolution Transmission Electron Microscope (HRTEM) technique, which is useful to visualize the structure at a very local level, in conjunction with the x-ray scattering techniques has been employed here to verify the thickness of the bilayers in the spontaneous superlattice structure. However, TEM does not provide compositional profile at the interface in such a nanoscale regime with good accuracy. The results obtained from the X-ray simulations were reported by T. Maitra *et al.* [23]. The experimental data along with the fitted ones for the XRR and the extracted composition profile are shown in Fig. 4.3(a) and (b), respectively. The extracted lattice parameter profile (LPP) from XRD by using the kinematical model showed well match with that obtained obeying vegard's law for the same compositions. The q scan (θ-2θ configuration) for (004) crystal planes and the extracted lattice parameter profile are shown in Fig. 4.3(c) and (d), respectively. So, through X-ray scattering technique, we were able to extract the structural details of the spontaneously formed partially ordered structures in a length scale of about

20 monolayers which is quite different from the conventional atomic ordering i.e. CuPt-B, CuPt-A, CuAu, etc. [47,137]. Surface reconstruction showed an important connection with previously reported atomic ordering [138]. However, in our case, interplay between the parameters involved in kinetics i.e. growth temperature, rate of the chemical reactions, growth rate stabilize the ordering in such a comparatively larger length scale in addition to the surface thermodynamics which can be considered as the cause of the ordering [62].

Stability of such structures was always an important issue regarding both the nature of ordering and the device application.

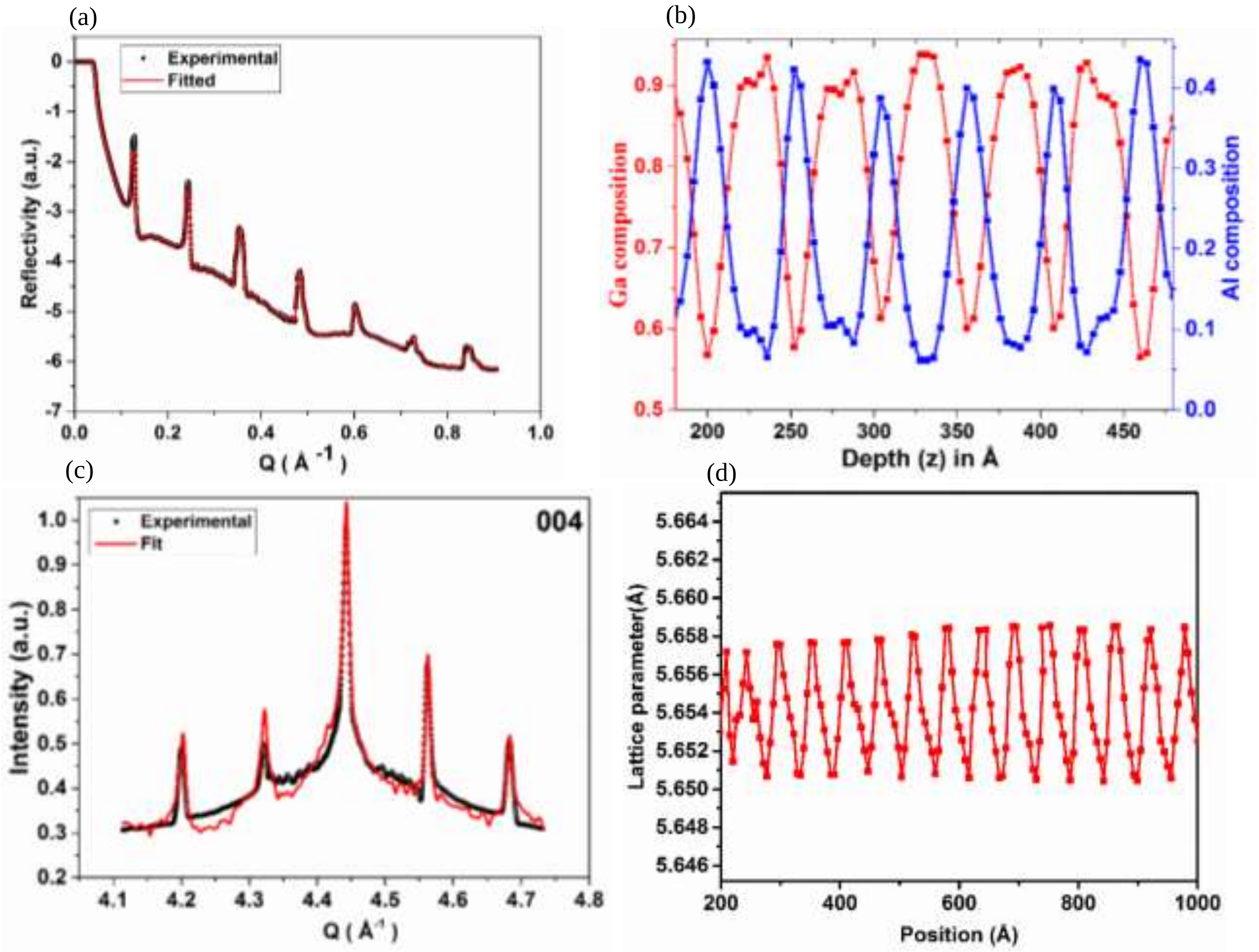

Fig. 4.3(a) Experimental (black dot) and fitted (red solid) X-ray reflectivity curves (b) Al and Ga fractions along depth extracted from the reflectivity (c) Experimental (black dot) and fitted (red), XRD curves, using the composition profile obtained from XRR (d) Extracted lattice parameter profile.

4.4 Summary

We have observed superlattice structures in a length scale of multiple monolayer in $Al_{0.3}Ga_{0.7}As$ barrier layer of AlGaAs/GaAs quantum well structures on GaAs (100). Despite the small bond length difference between AlAs and GaAs, such spontaneous ordering was also observed in $Al_{0.15}Ga_{0.85}As$ epilayer on GaAs substrates for the same orientation, reactor temperature and pressure. The presence of the ordered structures with the similar features not only denied the possibility of just an accident to get such structures but also it proves the stability of the ordering for different Al concentrations [21,23]. In this work, as mentioned, we have concentrated on the natural superlattice ordering, its thermal stability, and the utilization of it in device fabrication, for the particular Al compositions of 0.3 and 0.15. As our idea was to utilize the material for the optoelectronic application, we look for the material with a direct bandgap. We have grown AlGaAs with nominal Al content below 0.4 not only for the direct bandgap but also for the negligible lattice strain looking at the suitability of the material for the optoelectronic device applications. In the regime of our interest, the ordering is stable for a low concentration as well as a high concentration under similar growth conditions as described in this chapter.

Chapter 5

Structural and thermal stability of the natural superlattices

5.1 Introduction

It is important to study the thermal stability and the diffusion characteristics of the semiconductors as the device quality depends on the interdiffusion through the interfaces [139]. Atomic diffusion in semiconductors refers to the migration of atoms, including the host, the dopant, and the impurities [140]. The diffusion of atoms and defects (both native and dopant) is at the heart of semiconductor processing. This includes the growth, post-growth and device construction stages. For the case of chemical diffusion, the process occurs due to spatial gradients in the concentrations of the chemical components in the material. Self-diffusion in $Hg_{0.8}Cd_{0.2}Te$ for the formation of the p-n junction and dopant diffusion in GaAs/AlGaAs structures causing disordering is explained in literature [141,142]. Compositional interdiffusion (CID), donor or acceptor diffusion into GaAs-based superlattices can cause essentially complete intermixing on the cation sublattice [141]. This phenomenon is also known as diffusion induced disorder. Boron (B) or Arsenic (As) doping also results in rapid intermixing at a Si/Ge interface [143]. Profiling of the diffusant for the self-diffusion using a radiotracer has been widely used [144]. Neutron reflectometry has been used to measure Si self-diffusion in $^{29}Si/^{28}Si$ isotope multilayers [145]. Thermal diffusion in AlSb/GaSb multi-quantum wells was investigated through a temperature range of 820-950 K by employing photoluminescence (PL) spectroscopy [93]. Profiling techniques applicable to CID in quantum well and superlattice structures utilize either high-resolution x-ray diffraction (HRXRD) [94]. Double crystal X-ray diffraction (XRD) simulations have been employed for CdTe/CdMnTe multi-quantum well structures to extract the diffusion coefficient for post-growth annealing as well as the amount of diffusion during growth [146]. Self-diffusion of ^{71}Ge and ^{31}Si in Si-Ge alloys was found to follow an Arrhenius type relation with temperature as extracted using the radiotracer technique [147]. XRD patterns from Si/SiGe superlattices were utilized to extract the pre-exponential factors and the activation enthalpies for the interdiffusion process [148]. To study the structural stability of the spontaneously grown superlattice structures, we annealed the samples at different temperatures and the effect on the sample was monitored through XRD measurements. It was noticed that up to a temperature of 800 ^{o}C, the satellite peaks around the main Bragg, which carried the signature of the periodic structures, remained present but annealing at 900 ^{o}C caused disappearance of the satellite peaks. When the sample was heated, interdiffusion and redistribution of the atoms between the layers gradually led to the homogeneous concentration throughout the epilayer. The XRD scans performed after annealing the sample at different temperatures from 300 ^{o}C to 900 ^{o}C are shown in Fig. 5.1. As the satellite peaks contain the information of the superlattice structures, we have studied the interface intermixing and the interdiffusion phenomena in the structures using the temperature dependent XRD measurements while monitoring the superlattice peaks. The temperature range from 500 ^{o}C to 700 ^{o}C was chosen for the study as the heat treatment showed significant effect on the satellite peaks in the above mentioned range which was neither too fast nor too slow, suitable for monitoring. Study of interdiffusion in the natural superlattice structures was performed by employing a matlab code for interdiffusion and the output composition profile was then fed to the XRD code to generate the intensity vs q curves. The experimental results were then fitted using a kinematical model based on Born approximation (BA) to get the evolution of the profile as a function of the time of annealing at different temperatures.

5.2 Theoretical simulation

Fick's law of diffusion was used to solve the depth profile of the compositional modulation in the superlattice structures as a function of time with the step-like square wave initial composition

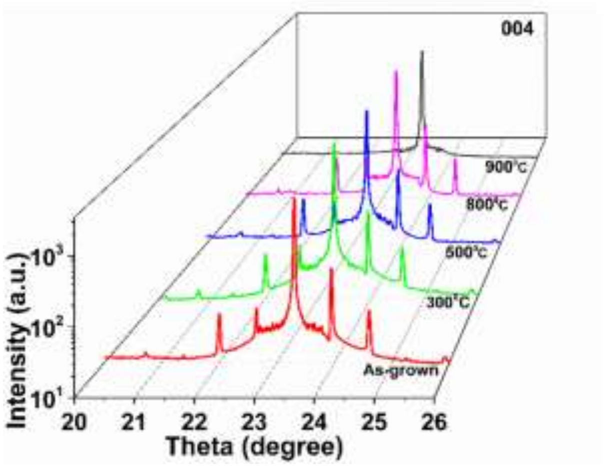

Fig. 5.1 (004) X-ray θ-2θ scans at different temperatures showing the stability of the ordered structures up to 800 ºC and loss of ordering at 900 ºC

profile. The compositional profile that was fed to the XRD code was basically the solution of the equation

$$\frac{\partial C(z,t)}{\partial t} = D\frac{\partial^2 C(z,t)}{\partial x^2} \qquad 5.1$$

The concentration of Al atoms, *C* was taken as function of depth *z*, and time *t*. The initial composition profile was taken as C (z, 0) for the periodic superlattice structures. The overall diffusion coefficient D was taken as an explicit function of temperature only whereas position and time were taken implicitly. In case of our sample, the diffusion coefficient of the superlattice layers was expressed as a superposition obeying Vegard's law [149]

$$D = D_{Al}^{0} C_{Al} \exp\left(-\frac{H_{Al}}{KT}\right) + D_{Ga}^{0} C_{Ga} \exp(-\frac{H_{Ga}}{KT}) \qquad 5.2$$

where C_{Ga} and C_{Al} are the fractional concentrations of Ga and Al, respectively in the superlattice structure. D^0_{Ga}, D^0_{Al} are the pre-exponential factors and H_{Ga}, H_{Al} are the activation enthalpies for Ga and Al diffusion into AlAs and GaAs, respectively, *K*, *T* are the Boltzman constant and the temperature, respectively. In the case of the diffusion process in our sample, the energy required for the Al or Ga atom to escape the potential of the surroundings is the activation energy. For the diffusion process to be completed the escaped Al (Ga) atom must find a suitable position in the GaAs (AlAs) crystal and hence the Eq. 5.2 bears the activation enthalpies instead of the activation energies of the atoms [149]. The X-ray diffraction curves in θ-2θ configuration was simulated using the kinematical model based on the first order BA. The diffracted intensity around a particular Bragg, away from the critical angle, can be written as the summation of the intensity from the epilayer and that from the substrate [150],

$$I_{tot}(q_z) = \left|\exp(iMa_sq_z)\sum_{n=0}^{N}(A_n\exp[i\sum_{j=0}^{n}a_jq_z]) + A_s\frac{1-\exp(iMa_sq_z)}{1-\exp(ia_sq_z)}\right|^2 \qquad 5.3$$

with a_s and A_s representing the out of plane lattice parameter and the scattering amplitude in the substrate material, respectively whereas M is the total number of layers in the substrate material each having a thickness equal to the lattice parameter of the substrate material. To obtain the total intensity as a function of the scattering vector (q_z) normal to the sample surface, the epitaxial layer was considered to be divided into N number of sub-layers each having a constant local composition and thickness equal to the local lattice parameter. The lattice parameter and the scattering amplitude of the nth sub-layer are denoted by a_n and A_n, respectively, values of which were decided by the local composition of the corresponding layer.

The simulation approach we used is a combination of an interdiffusion code (equivalent to run a virtual interdiffusion experiment) and a code on XRD. Theoretically, for the as-grown sample, a model composition profile comprised of a bilayer, denoted as layer ‘A’ and ‘B’ with a slight difference in Al fraction (roughly, $Al_{0.15+\delta}Ga_{0.85-\delta}As$ for layer ‘A’ and $Al_{0.85-\delta}Ga_{0.15+\delta}As$ as layer ‘B’) with almost abrupt interface repeated for several times was used as the initial profile C (z, 0) to the interdiffusion code. The model periodic structure was taken as the input to the diffusion equation to get the time evolved composition profile C (z, t) at a given temperature, which showed the distortion of the square wave composition profile. The annealing temperature was taken as a parameter. Solving the diffusion equation, the output i.e. the composition-position-time matrix C (z, t) was then fed into the XRD code to generate the X-ray θ-2θ curves at different annealing times i.e. intensity-scattering vector-time matrix I (q_z, t). The simulated XRD superlattice satellite peak structures showed significant changes as a result of interdiffusion across the interfaces. The integrated satellite peak intensities were reduced as the shape of the square wave composition profile got distorted with annealing time. Distortion of the initial square type composition profile and as a result, changes in the x-ray diffraction curves for prolonged annealing time at a fixed anneal temperature of 600 ^{o}C are represented in Fig. 5.2(a) and (b), respectively. It has already been established that for (000) (direct beam) as well as (004) reflection, assuming the initial sinusoidal or square composition profile, the interdiffusivity goes linearly with the decay rate of natural logarithm of the first order satellite peak in accordance with the following equation [151],

$$-\frac{d}{dt}\left(\ln\left(\frac{I(t)}{I(0)}\right)\right) = \frac{8\pi^2}{\mathrm{L}^2}D \qquad 5.4$$

where I(t), the integrated superlattice satellite intensity at time t, I(0), the initial integrated intensity of the satellite peak, L, the spatial period of the superlattice defined previously and D represent the diffusion coefficient as expressed in Eq. 5.2. The integrated intensities of the first order satellite peaks with annealing time were monitored and the decay rate was compared with the experimental data to extract the diffusivity values as prescribed by Eq.5.4. Besides, we used the above equation to evaluate the composition dependence of the inter-diffusivity taking three different values of Al composition at each time step throughout the total depth, the maximum, the minimum and the mean as extracted from the XRD simulations. The decay rate of the satellite intensity for the interdiffusivity values correspond to the maximum Al composition has been found to follow the experimental decay curves.

5.3 Distortion of the composition profile extracted from high temperature XRD measurements

The spontaneously grown AlGaAs/GaAs (100) superlattice structures are suitable for measuring interdiffusion through XRD as satellite peak intensities depend on the compositional contrast in the layers. To validate our calculation based on the model, we compared the experimental XRD curves with the simulation results. The XRD curves were first simulated using the inter-diffusion code followed by the x-ray diffraction code and then fitted to experimental x-ray θ-2θ curves. The experimental curves and the fitted ones based on the calculation for three different annealing temperatures of 500 °C, 600 °C and 675 °C for a fixed annealing time of 20 minutes are shown in Fig. 5.3(a) while Fig. 5.3(b) represents the output composition profile obtained from fitting. It is evident from the later that with increasing anneal temperature, the contrast in composition between the two consecutive layers has become less and the interface got broadened. The extracted values of the Al fraction and the interfacial width for five different annealing temperatures are listed in Table 5.1. The simulated x-ray curves for increasing anneal time at a fixed temperature, given in

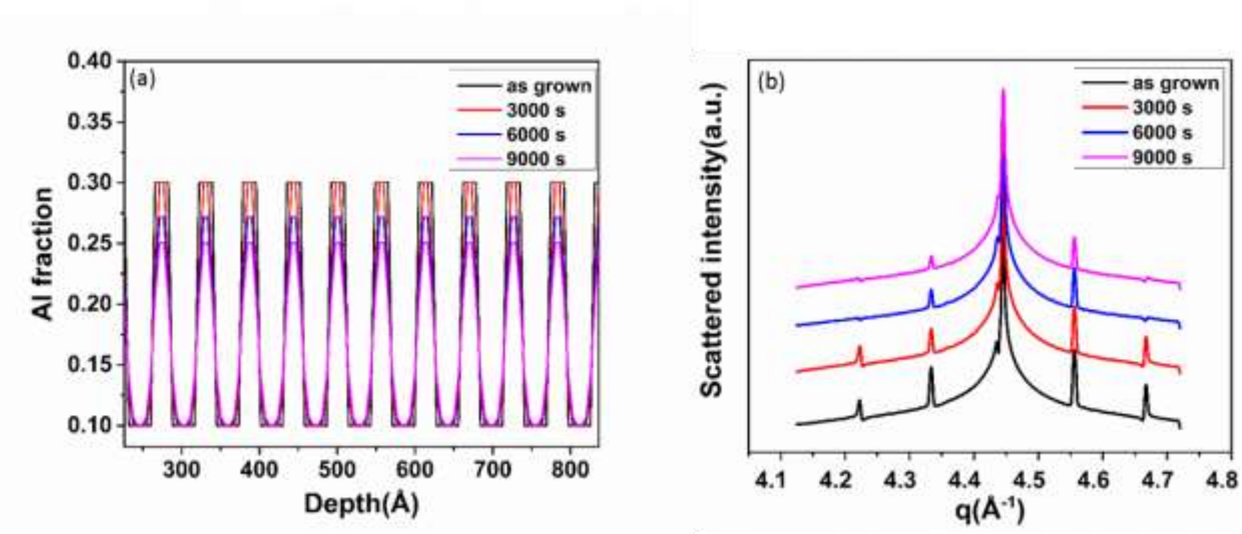

Fig. 5.2 (a) Virtual interdiffusion experiment which shows change in composition profile for the as-grown and three different annealing times and (b) Simulated x-ray diffraction curves for the structures described in (a)

Fig. 5.2(b), clearly showed the decrease in intensity of the satellite peaks. The second order satellite peaks were more sensitive to annealing as the decay of the intensity was faster in comparison with that for the first order. But as the intensity of the second order peak was much lower, it would be appropriate and reliable to monitor the first order satellite peak intensity. So, integrated intensities of the first order satellite peak were collected for prolonged annealing time (not continuously but at a finite time interval fixed by the time taken for a scan at each time to be completed) from the experimental XRD curves and plotted with annealing time. To correlate the experimentally obtained satellite peak intensity with the theoretical, interdiffusion driven XRD intensity, we

Table 5.1 Extracted structural parameters: the Al composition in two consecutive layers and interfacial widths by fitting the XRD curves for five different temperatures

Anneal temperature (°C)	Al composition in layer A	Al composition in layer B	Compositional contrast	Mean Al composition	Interfacial width (Å) (d_{AB+BA})
500	0.05	0.35	0.3	0.17	16
600	0.07	0.3	0.23	0.16	18
625	0.09	0.22	0.13	0.15	25
675	0.1	0.2	0.1	0.14	28
700	0.11	0.19	0.07	0.14	30

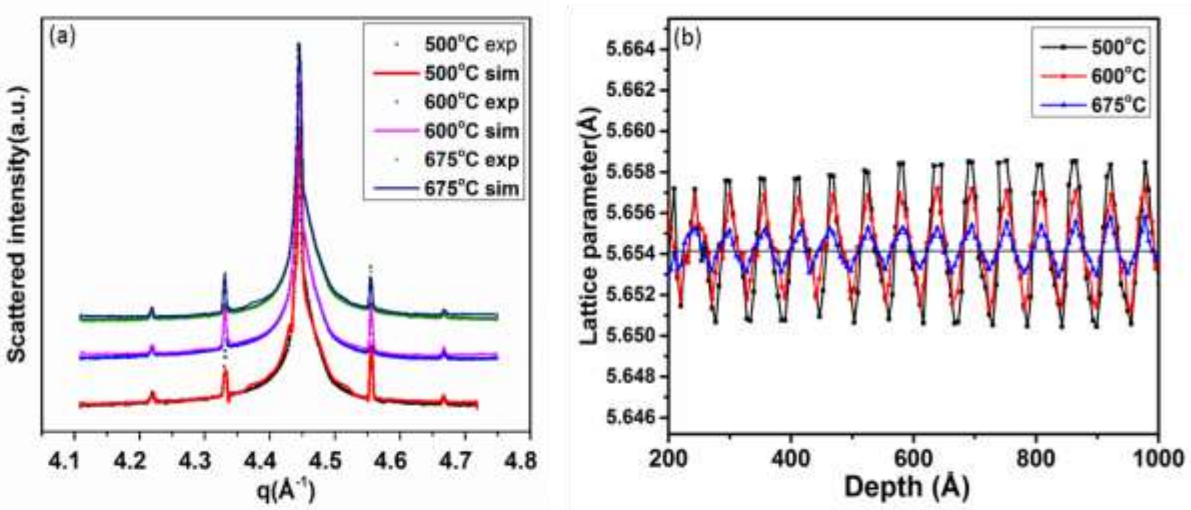

Fig. 5.3 Experimental x-ray diffraction curves taken for three different temperatures along with fitted ones using our model and (b) Extracted lattice parameters from fitting for 500, 600 and 675 °C

clubbed and plotted the same data from the simulated rocking curves, finally compared them with the experimental data by employing a standard fitting procedure. Excellent match between the theoretical and experimental data established the fact that the model combining interdiffusion and XRD could be well applicable to our natural superlattice structures present in the AlGaAs system for the (004) diffraction planes. We collected the integrated intensities for prolonged anneal time at 500, 600, 625, 675 and 700 ^{o}C. The experimentally collected data for the decay of the first order satellite peak and those taken from the theoretical simulation are presented in Fig. 5.4(a). For the three temperatures in the lower regime, 500, 600 and 625 ^{o}C, the nature of the decay curves showed similar behavior with increasing annealing time. The integrated intensity of the first order satellite peak, decaying initially at a faster rate, was followed by a relatively slower decrease at a later time. At higher temperatures i.e. 675 ^{o}C and 700 ^{o}C, the integrated intensity got reduced in almost no time and monotonically decrease at a much slower rate as time elapsed. In the inset of Fig. 5.4(a), the negative of the satellite decay rate which was in turn proportional to the interdiffusion coefficient values at subsequent temperatures are plotted against the time for which annealing was allowed. It was evident that the interdiffusivity for lower anneal time increased from 500 ^{o}C to 625 ^{o}C, attaining a maximum at 625 ^{o}C and further decreased for higher temperatures to possess a minimum value at 700 ^{o}C. Up to a certain time, the values of the diffusivity decreased sharply and thereafter showed the trend to saturate for all three temperatures of 500, 600 and 625 ^{o}C. The initial decay rates at 675 ^{o}C and 700 ^{o}C were less than those observed at the lower temperatures as the compositional contrast was quickly reduced at such temperatures higher than 625 ^{o}C. The increase in the decay rates i.e. interdiffusivity with increasing temperature from 500 ^{o}C to 625 ^{o}C was quite normal as increase in temperature would enhance the surface mobility of the adatoms. But after that temperature, the value of the contrast in composition i.e. the concentration gradient dropped below a certain critical value that prevented further increase in diffusion for temperatures above 625 °C. The product 'Dt' for the five different temperatures was also plotted against the anneal time as shown in Fig. 5.4(b). For all the temperatures, the variation of the product suggested the composition dependence and the nonlinearity of diffusion process. The product showed increasing behavior with time to attain a maximum sometime later as the annealing temperature kept on increasing. The product peaked at about 12000 s, 8000 s, 6000 s for 500 °C, 600 °C and 625 °C respectively. The fact could be explained using the arguments that as the temperature was raised from 500 °C towards 625 °C, the rate of diffusion increased which moved the product to its maxima at an earlier time. After that, a drastic change in the pattern showed that the product increased at a relatively slower rate and gave broad peak at 20000 s for 675 °C and kept on increasing at a very slow rate for 700 °C up to 28500 s of annealing time. Such behavior of the "Dt" vs t curves showed clear indication of the nonlinearity and also saturation after 625 °C in the diffusion process for our superlattice structures. If D were constant in time, then we must have an ever increasing straight line of "Dt" with increasing time. The portions of the curves which showed decay with time reflects

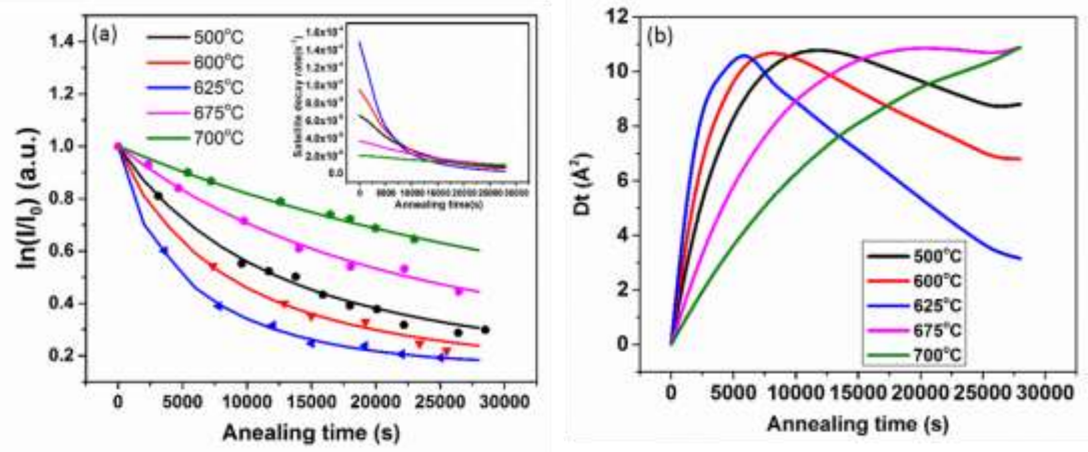

Fig. 5.4 Plot of fall of 1st order integrated satellite peak intensity with annealing time from x-ray diffraction simulation using composition profile from interdiffusion code. The discrete dots represent the experimental data and dots with the lines represent theoretical ones while the negative of the satellite decay rate vs annealing time is shown in the inset and (b) Product 'Dt' vs anneal time at five different temperatures

the fact that the D values decreased in such a way that the product dropped with time. Above 625 ^{o}C, as the temperature increased, the rate of change in D values got slower and the curve found its maximum at a later time. At 700 ^{o}C, the curve kept on increasing up to 28500 s which was our limit for annealing time. We derived the results for the maximum annealing time of 28500 s. This is true that the decrease in the "D" values might not be sufficient for the lowering of the "Dt" values for successive annealing time beyond 28000 s at 700 ^{o}C.

5.4 Concentration dependence of interdiffusivity

Further, the concentration dependence of the interdiffusion coefficient was studied quantitatively by employing the calculation of the decay rates of the satellite peak using Eq. 5.2 followed by Eq. 5.4. First, we calculated the values of the diffusion coefficient using Eq. 5.2 at time t=0 for each temperature for three different Al concentrations: maximum, minimum and the mean value which are the values of Al concentration of layer B, layer A and their mean value ($(C_A+C_B)/2$), respectively, as given in Table 5.1. This approach was adopted because from these three value, we would have the idea of the decay behavior for all the compositions those lie in between. Later on, we would see that theoretical curves corresponding to the three values were sufficient to ascertain the trend of the experimental results. Then we calculated the decay rates using Eq. 5.4 at each temperature for the three D values appropriate for the three concentrations mentioned above. We presented the decay rates from the experimental rocking curves, XRD simulations and output using Eq. 5.4 for five different temperatures of 500, 600, 625, 675 and 700 ^{o}C in Fig. 5.5(b), (c), (d), (e) and (f), respectively. We started with a concentration independent interdiffusivity value which showed a linear decay of integrated satellite intensity for prolonged annealing time both from XRD simulations and the output using the decay equation as given in Fig 5.5(a). The decay curves taking the interdiffusivity values appropriate for the minimum and the mean Al composition deviated considerably from the experimentally obtained data. The interdiffusivity for the maximum Al composition showed a satisfactory fit of the satellite decay curve with the experimental data for all the specified temperatures. This suggests that the diffusion described by the decay equation could also follow the experimental satellite decay with a single Al composition which is the Al fraction in layer B in this case at each time step. So, the decay equation could be well applicable for (004) reflection and square composition profile for our naturally grown superlattice system. The simulated composition profiles for three different annealing times shown in Fig 5.5(a) depicted clearly that for our superlattice structures, the maximum Al fraction (Al composition in layer B) changed much rapidly with time rather than the mean and the minimum values. The same fact could also be observed from the values listed in Table 5.1 for five different temperatures. So, we can conclude that the time variation of the maximum Al fraction was predominantly responsible the interdiffusion across the interface. This can be attributed to the fact that the composition dependent diffusivity values for the maximum Al fraction along the depth are well applicable for the decay rate calculation using decay equation to fit the experimental data. We extracted the D values from the fitting the experimental data with the theoretical model. We have used the values of the pre- exponential factor and activation enthalpy for intermixing as given in ref. [149] for AlGaAs/ GaAs QW system as the initial guess. Although the extracted values of pre-exponential factor have come out to be almost consistent but the activation enthalpy values found to deviate from the initial value 3.5 eV to 0.5 eV. As our system is $Al_xGa_{1-x}As/Al_yGa_{1-y}As$ superlattice type structure, the activation enthalpy for intermixing was found to be as low as 0.5 eV. We can conclude that the self-diffusion in AlGaAs is much faster than AlGaAs-GaAs interdiffusion. So, the diffusion coefficient values in our case are much higher than previously reported for AlGaAs/GaAs QW type system. The pre-exponential factors and the activation enthalpies coming out as a result of the fitting of the experimental data are listed in Table 5.2.

Table 5.2 Extracted parameters related to interdiffusion, the pre-exponential factors and the activation enthalpy values for five different temperatures

Temperature(°C)	D^0_{Al} (cm^2/s)	H_{Al} (eV)	D^0_{Ga} (cm^2/s)	H_{Ga} (eV)
500	0.17	0.5	0.01	3.48
600	0.2	0.525	0.05	3.5
625	0.18	0.55	0.1	3.45
675	0.25	0.57	0.12	3.4
700	0.23	0.62	0.11	3.42

The extracted value of the activation enthalpy for Al atoms was found ~0.5 eV whereas that for Ga atoms acquired a much higher value of ~3.5 eV. This difference in the values of the activation enthalpy between Al and Ga atoms could not be explained by taking into account the vacancy

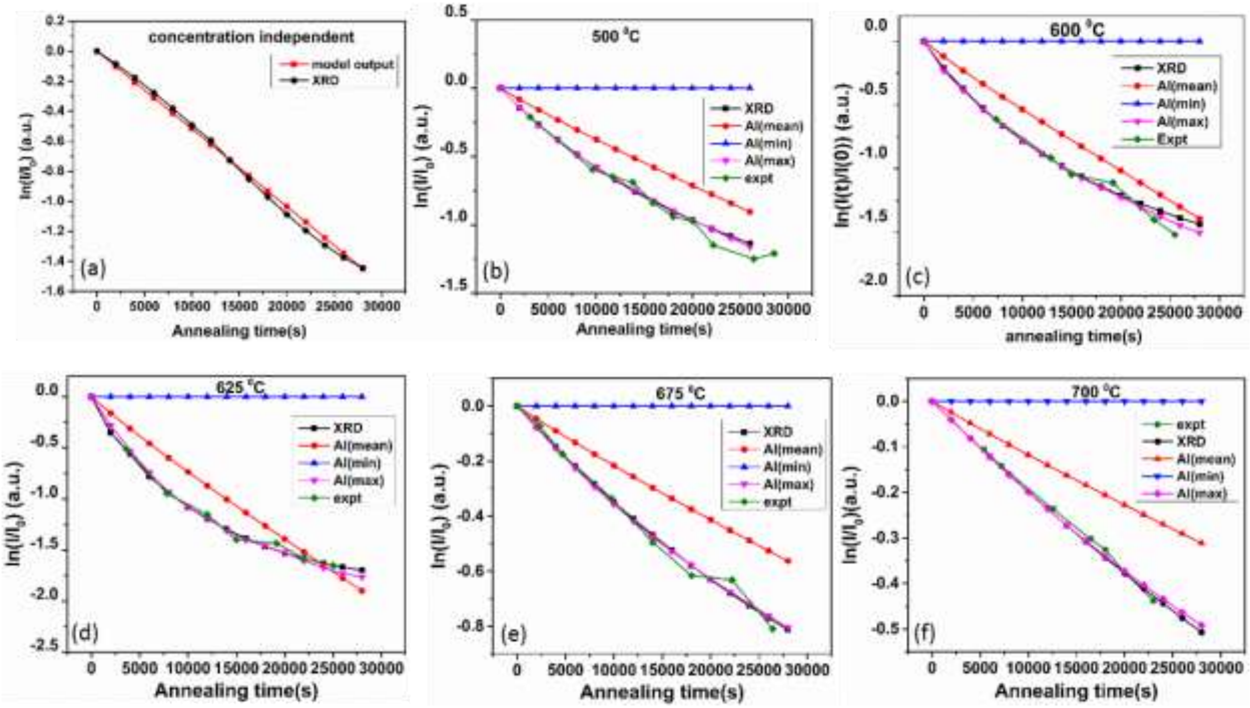

Fig. 5.5 Plot of integrated intensity of the 1st order satellite peaks obtained from x-ray diffraction and composition independent model using Eq. 2 and Eq. 4 successively and (b), (c), (d), (e), (f) show the plot of integrated intensity vs anneal time from x-ray diffraction and model output for min, max and mean Al fraction for 500, 600 625, 675 and 700 °C, respectively

diffusion mechanism only as that would lead to nearly equal values [149]. The smaller size of Al atoms may contribute to its higher surface migration velocity. But the reason for such a significant difference in the values of the activation enthalpy is not very clear till now. Further study is needed to explain this type of diffusion in the newly observed spontaneous $Al_xGa_{1-x}As/Al_yGa_{1-y}As$ superlattice structure. The values of the diffusion coefficient obtained have been plotted against annealing temperature for three different times as shown in Fig. 5.6. The variation showed that for 6000 s of annealing the value of the interdiffusivity increased up to 625 °C and then decreased at higher temperatures [25]. For higher anneal times i.e. 8000 and 10000 s, the diffusivity value found its maximum at 600 °C and dropped sharply at 625 °C as the critical value of the compositional contrast was reached beyond which diffusion was not favorable. In other words, the occurrence of fast diffusion at 625 °C up to 6000 s of annealing resulted in a much lower compositional contrast such that the interdiffusivity value at 625 °C dropped below that at 600 °C beyond 6000 s of annealing and thereafter.

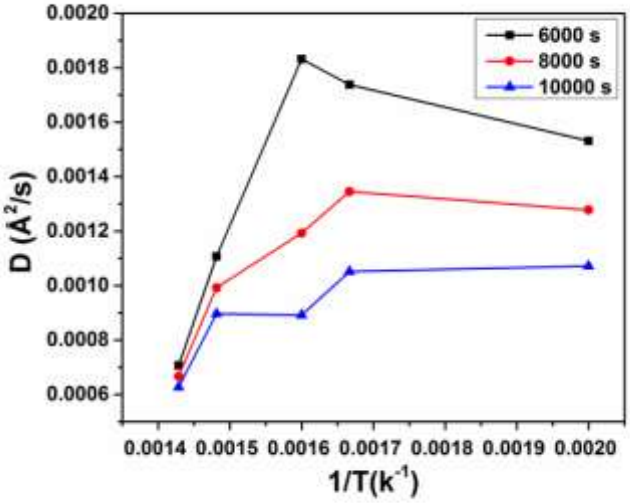

Fig. 5.6 Plot of interdiffusion coefficient against inverse of anneal temperature for data taken at three different anneal times

5.5 Summary

An important issue for such spontaneously grown superlattice structures was the thermal stability as most device fabrication needed high temperature processing. Interdiffusion and intermixing of such $Al_{0.15+\delta}Ga_{0.85-\delta}As/Al_{0.15-\delta}Ga_{0.85+\delta}As$ (δ~0.1) was also important from fundamental physics perspective. The satellite peaks in XRD measurements have been correlated with interdiffusion between the consecutive layers. The interdiffusivity has come out to be concentration dependent and nonlinear. Only the maximum concentration of Al was found to be sufficient to describe the intermixing as the diffusion of the Al atoms was more preferable compared to the Ga atoms. The activation enthalpy for Al interdiffusion was found much lesser than that of relatively larger Ga atoms. High temperature XRD along with necessary theoretical simulations was employed successfully to evaluate the interdiffusion in superlattice structures. The rate of interdiffusion increased initially as expected as the temperature was raised from 500 ^oC to 625 ^oC and decayed thereafter as compositional contrast, which was the driving force for the interdiffusion to occur, reached its critical value. Slow diffusion was responsible to stabilize the structure up to 800 ^oC with significant amount of intermixing, but when the sample was annealed at sufficient temperature (900 ^oC), the thermal energy of the atoms became comparable with the activation enthalpy for diffusion and consequently, diffusion of the atoms from region of higher concentration to that of lower made the layer homogeneous throughout and as a result the spontaneous ordering disappeared. Next, we have studied the effect of the ordering on the optical properties of the material. In the last part, we have fabricated photodetectors out of the ordered and disordered materials and studied the effect of the ordering on the photoresponse properties.

Chapter 6

Effect of the natural superlattice ordering on the optical and electrical properties

6.1 Introduction

Atomic ordering or formation of superlattice structures in semiconductors have been found to significantly modify its optical properties and device characteristics [72,152]. Atomic ordering causes a well distinguishable effect on the optical property that is reduction in band gap of the semiconductor [153]. During the efforts to realize red-light-emitting laser-diodes with the compound AlGaInP grown by metal-organic vapor phase epitaxy (MOVPE), it was noticed that the bandgap of $Ga_{0.5}In_{0.5}P$, which is an end-point ternary alloy used as the active layer of the laser diode, had an anomalous lower value of 1.85 eV (at room temperature) than the then-most-reliable value (1.91-1.92 eV). The reduction in the bang gap was correlated to the atomic ordering in the material from the structural analysis [44]. The observed shift in the photoluminescence (PL) peak energy and the enhancement in the PL integrated intensity in the $Al_{0.4}GaAs$ well with $Al_{0.7}GaAs$ barrier grown on (111) GaAs by molecular beam epitaxy (MBE) was attributed the spontaneous formation of Al and Ga rich superlattice ordering in the well layer [154]. Infrared photodiodes using the InAs/GaInSb strained layer superlattice in heterojunctions with GaSb have been demonstrated with high quantum efficiency arising from the favorable absorption properties [155]. Improvement of the device performance as an effect of heat treatment was reported for 4H-SiC metal–semiconductor–metal ultraviolet photodetectors [156]. In the absence of the homogeneous AlGaAs with the same Al content for the similar growth conditions, to study the effect of the natural superlattice ordering, we have made a comparative study between the as-grown ordered and the annealed disordered samples. Furthermore, our aim was a systematic investigation of the effect of annealing on the microscopic structures of the spontaneous superlattice and also the optical properties and the device performance and to establish the correlation between the structural and the optical and electrical properties of the natural superlattice ordering. This is another important reason for using the ordered and thermally annealed disordered sample to understand the effect of the superlattice ordering on the optical and electrical properties of the material. In regard to the utilization of the superlattice structures in device fabrication and a systematic study of the device characteristics with temperature, the crystallinity of the bulk and the surface of the sample after the heat treatment were two important factors that should be considered to affect the properties of the material. Normally, high-temperature annealing can significantly modify the morphology of the materials and defects may be incorporated unintentionally. To exclude the possibilities of damage of the surface or incorporation of unintentional defects, we have examined the as-grown and the annealed samples through SEM, XTEM and XRD measurements to comment on their structural quality. The annealing was done under arsenic overpressure to prevent the arsenic desorption from the surface and retain the surface morphology intact. The SEM images of the surface before and after annealing, shown in Fig. 6.1(a) and (b) respectively, clearly revealed that the surface morphology did not change with annealing. Fig. 6.2 shows the elemental mapping using XTEM for the as-grown (ordered) and the 900 °C annealed (disordered) sample [28]. A periodic modulation in the Al and Ga distribution was observed for the as-grown sample (Fig. 6.2(a)) whereas the annealed sample (Fig. 6.2(b)) showed homogeneous distribution of these elements throughout the epitaxial layer. Distribution of As was uniform throughout the area of the scan for both the samples. For the crystallinity of the material, X-ray diffraction (XRD) measurements are done for both the as-grown and the annealed sample as shown in Fig. 6.3 [21]. The black trace shows the XRD curve (θ-2θ scan) of the as-grown $Al_xGa_{1-x}As$ layer for the (004) crystallographic planes consisting of strong substrate Bragg peak at the center, strong, sharp and nearly equispaced peaks are present on both sides of it. The disappearance of the satellite peaks in case of the annealed sample (red trace) can be attributed to the concentration homogeneity as a result of interdiffusion. No shift in the zeroth order peak and unaltered peak width suggest the crystalline quality remained unaffected.

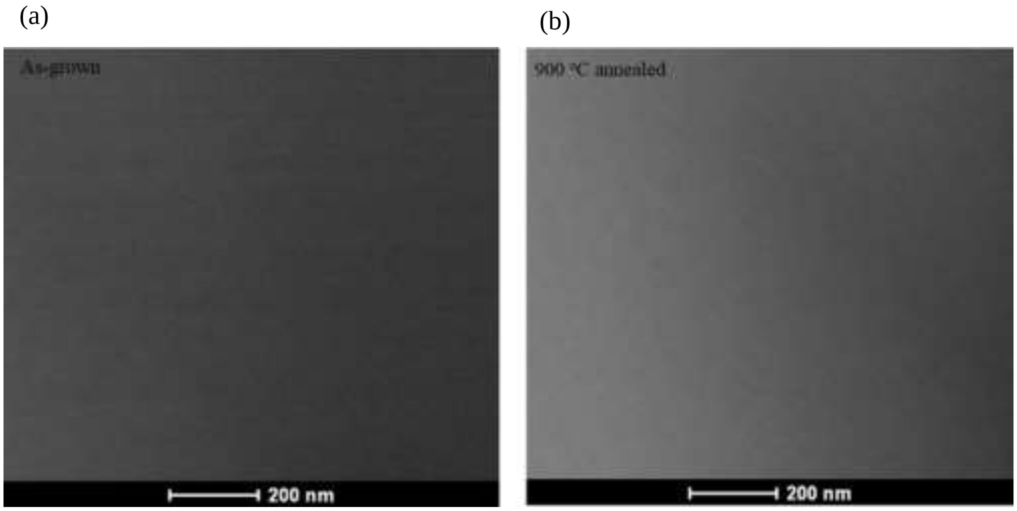

Fig. 6.1 SEM images of the surface of the (a) as-grown and (b) 900 °C annealed sample

6.2 Optical properties

6.2.1 Photoluminescence

Optical properties of the ordered and disordered samples are compared on the light of photoluminescence (PL) spectroscopy. The PL spectra for both the samples consist of a high energy sharp peak corresponding to the bandgap related transition and a relatively weaker low energy peak. The peak appeared at lower energy could be attributed to free to bound (F-B) transition related to carbon acceptor commonly observed during MOCVD growth [157]. The temperature dependent PL spectra for both the ordered and disordered samples, as given in the upper and lower panel of Fig. 6.4(a), respectively, show three important features: firstly, the excitonic peaks shift toward low energy with the increase in temperature for both the samples following Varshni relation [158]

$$E_g(T) = Eg(0) - \frac{\alpha T^2}{\beta + T} \qquad 6.1$$

The peak position as a function of temperature for the ordered and disordered samples are shown in the upper panel of Fig. 6.4(b). Secondly, a clear redshift of about 34 meV in the excitonic transition was observed for the ordered sample in comparison to the disordered case throughout the whole temperature range. Thirdly, the integrated PL intensity in both the cases falls with temperature obeying the modified Arrhenius equation [159]

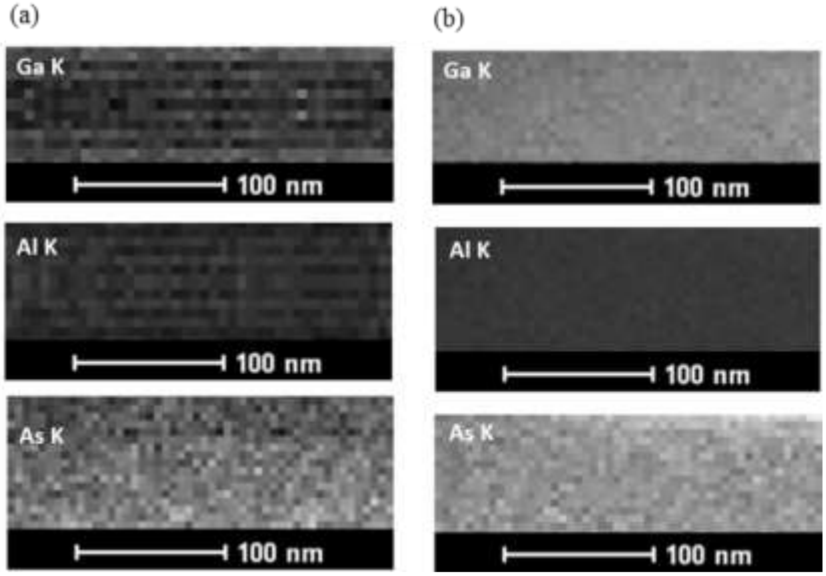

Fig. 6.2 Cross sectional elemental mapping for Al, Ga and As for the (a) aAs-grown and (b) 900 ºC annealed samples

$$I = \frac{I_0}{1 + A * \exp\left(-\frac{E_A}{k_B T}\right) + B * \exp(-\frac{E_B}{k_B T})} \qquad 6.2$$

with A and B being considered as constant fitting parameters and E_A and E_B are the two activation energies appropriate for the two temperature ranges. The experimental and the fitted integrated intensity vs temperature plots are shown in the lower panel of Fig. 6.4(b).

6.2.2 Explanation

Structural studies through TEM and XRD show the loss of the spontaneous ordering as a result of interdiffusion at a temperature of 900 ^{o}C without affecting the crystalline quality of the material. As the crystal structure and the average composition remain unchanged, the difference in the optical properties measured from the PL spectra can solely be attributed to the order-disorder transition. The bandgap related PL peak with reduced intensity (~1/60 times) appears at 1.766 eV for the annealed disordered sample at 4K. In comparison, the peak energy for the as-grown sample, 1.732 eV, suggests a clear redshift of 34 meV. The reduction in the bandgap may be thought of as the effect of repulsion between the folded bands due to the presence of ordering [62]. More elaborately, as the crystal periodicity extends about 20 times that in the original zinc-blende structure in (001) direction, the k-points folded to 1/20th in the reciprocal space results in overlap of the bands. When spin-orbit coupling is considered, the states both in conduction and valance band bearing the same symmetry split with the degeneracy left off. With incorporation of ordering

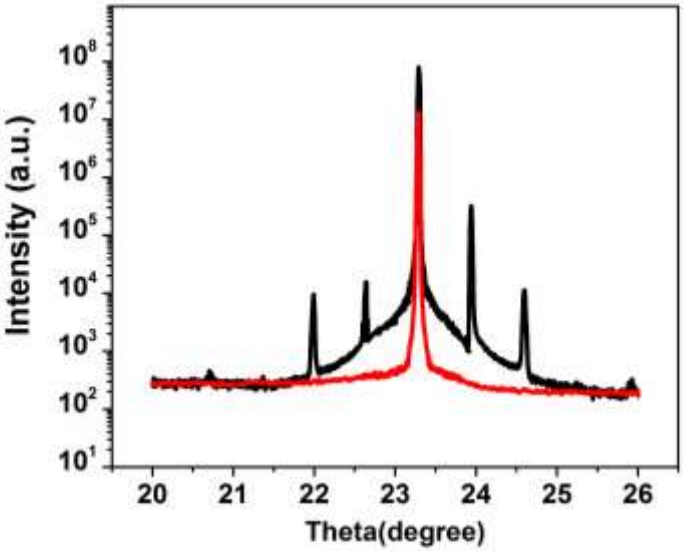

Fig. 6.3 (004) X-ray θ-2θ scans for the ordered as-grown (black) and the disordered 900 oC annealed sample showing loss of ordering while keeping the crystallinity intact

as a perturbation, the repulsion between these states causes the reduction of the bandgap in the ordered sample. The decay of photoluminescence intensity with temperature has been fitted with the modified Arrhenius equation for both the samples. The two excitonic binding energies come out to be 9.87, 43.09 and 6.07, 36.36 meV for the As-grown and the annealed sample respectively. Two binding energies suggest activation of the excitons through two different channels at lower and higher temperature regions. The higher binding energy is basically related to the confinement of the carriers in the superlattice layers which enhances the stability of the excitons in the superlattice channels compared to the disordered sample. In the absence of the proper theoretical knowledge on the modification of the PL peak energy and intensity due to such natural superlattice ordering, we are unable to draw any quantitative conclusion by matching the experimental and theoretical results. It would be an interesting study in the future. Experimentally, the same kind of enhancement of the optical quality (stronger photoluminescence signal) was reported earlier as a result of ordering in multiple monolayer length scales by Chin and his coworkers [154]. They have concluded the enhancement in the optical quality as an effect of the spontaneous formation of Al and Ga rich layers in the QW region although no proper theoretical background was discussed. In general, in quantum heterostructures such as quantum well, superlattice structures, there must be a certain amount of localization of the excitons that would lead to higher excitonic binding energy in comparison with the bulk material due to squeezing of the radius of the excitons in the quantum heterostructures.

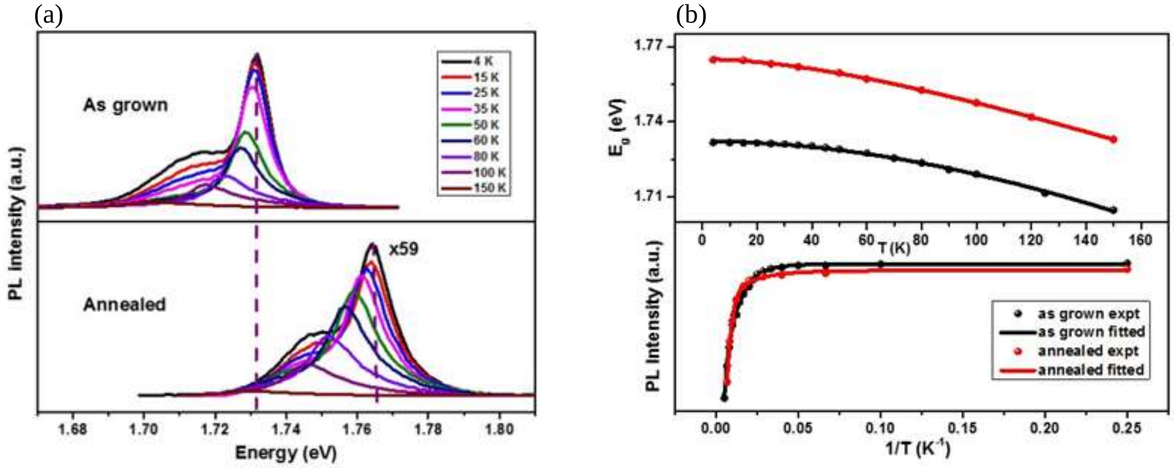

Fig. 6.4 Temperature dependent PL spectra of the as-grown (upper panel) and the annealed sample (lower panel) and (b) Peak energy as a function of temperature (upper panel) whereas the integrated PL intensity vs 1/T (lower panel) for both the samples

6.3 Device fabrication

We have developed Au-Ge/AlGaAs/Ni planar type metal semiconductor metal (MSM) structure with a simple geometry for photodetector application in the vis to near IR regime. Our motivation was to fabricate the device based on the spontaneous superlattice structures and further study the effect of ordering on the device performance through electrical characterization. Three devices with the as-grown (A), the 700 ^{o}C annealed (B), and the 900 ^{o}C annealed (C) sample as the semiconducting active layer were fabricated with the thermal evaporation technique having the same coplanar junctions on the front face as shown in Fig. 6.6. In general, MSM PDs have two comb-like electrodes with 1 μm spacing. In the absence of photolithographic technique in our laboratory to form such electrodes within the time limit of completion of the thesis work, we have fabricated simple back to back connected Schottky diode photodetector with two asymmetric metal contacts on the front face of the semiconductor. The dimension of the electrodes are 1.5×3 mm^2 and the spacing between them is about 4 mm. Gold-Germanium alloy (Au88%Ge12%) and Nickel

(Ni), selected for the two metal contacts of the MSM structure, were deposited by thermal evaporation on the front face of the sample using appropriate masks. Starting with the as-grown sample, the structure retains its periodic nature with certain amount of inter-diffusion up to 700 ^{o}C of annealing but results in a bulk AlGaAs layer with uniform Al composition after annealing at 900 ^{o}C. The current voltage (I-V) characteristics of the structure were analyzed in dark and under illumination conditions with the wavelength ranging from 400 to 900 nm. The variations of the extracted parameters from the electrical equivalent model were discussed in details. The superiority of the device based on the superlattice structures in comparison with that based on the bulk one was described in terms of the figure of merits such as the detectivity (D), responsivity (R) and photosensitivity (S). The temporal response of the devices for the switching applications was also tested with the application of square pulsed light signals in a certain range of frequency of the input.

6.4 Theory and simulation

Considering the device with the superlattice structures as in case of A and B, we used a three diode model with two parallel and a series resistance as shown in Fig. 6.5 for the simulation of the I-V characteristic curves [160]. We considered two back to back connected Schottky diodes for the two terminals, and a third diode in the second sub-circuit corresponding to the heterojunctions due to compositional modulation in the epilayer as the electrical equivalent for both the devices. Taking the major contribution of thermionic emission to current with the presence of the recombination effect, the terminal voltage could be expressed as,

$$V = V_R + V_1 + V_2 \tag{6.3}$$

Where V_R is the voltage drop across the series resistance R_S and V_1, V_2 are the voltage drop across the diodes. The terminal current was taken the same through the sub-circuits and can be given as

$$I = \frac{V_R}{R_S} \tag{6.4a}$$

$$I = I_{01}\left(e^{\frac{V_1}{\eta_1 v_t}} - 1\right) + \frac{V_1}{R_{p1}} \tag{6.4b}$$

$$I = -I_{02}\left(e^{\frac{V_2}{\eta_2 v_t}} - 1\right) + I_{03}\left(e^{\frac{-V_2}{\eta_2 v_t}} - 1\right) - \frac{V_2}{R_{p2}} \tag{6.4c}$$

Where I_{01}, I_{02} and I_{03}, the reverse saturation currents for the three diodes, η_1, η_2, the diode ideality factors, R_{p1}, R_{p2}, the parallel resistances taking the recombination of the carriers into account and v_t, the thermal potential expressed as k_BT/q. The two diodes with opposite polarity in the sub-circuit 2 were considered to have the same value of the ideality factor for simplicity of calculations. The thermionic emission dominant carrier transport gives the reverse saturation current as follows

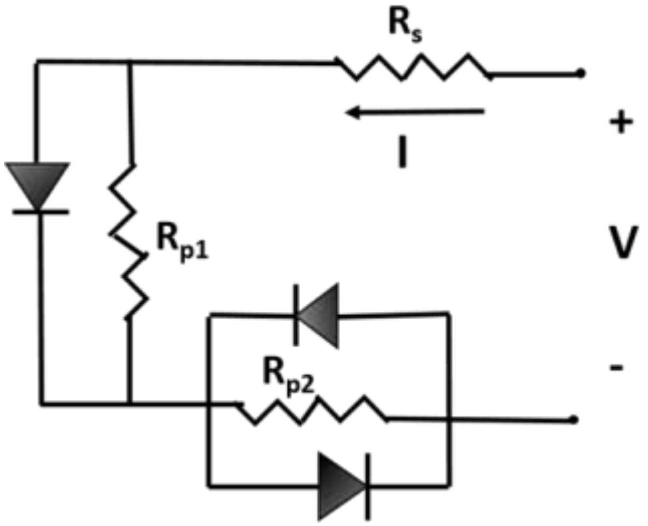

Fig. 6.5 Three diode model for simulation of the I-V curves of the superlattice based devices

$$I_{0i} = A^* A_i T^2 e^{\left(-\frac{q\phi_{Bi}}{k_B T}\right)} \tag{6.5}$$

A^* is the Richardson constant given by $A^*=4\pi q m_e^* k_B^2/h^3$, A_i represents the area of the i-th junction and φ_{Bi} is the barrier height at the i-th junction, T is the temperature of operation. Implementation of Lambert W transformation in Eq. 6.4b and 6.4c could lead us to expressions for V_1 and V_2

respectively as a function of the terminal current [161]. Then from Eq. 6.3, we arrived at the desired form of the terminal voltage,

$$V = R_{p1}(I + I_{01}) - \eta_1 v_t W\left(\frac{I_{01}R_{p1}}{\eta_1 v_t} e^{\left[\frac{(I+I_{01})R_{p1}}{\eta_1 v_t}\right]}\right) - R_{p2}(-I + I_{02} - I_{03}) +$$
$$\eta_2 v_t W\left(\frac{(I_{02}-I_{03})R_{p2}}{\eta_2 v_t} e^{\left[\frac{(-I+I_{02}-I_{03})R_{p2}}{\eta_2 v_t}\right]}\right) + IR_s \qquad 6.6$$

The parameters to be extracted from fitting the experimental data using the described model were φ_{B1}, φ_{B2}, φ_{B3}, η_1, η_2, R_s, R_{p1}, R_{p2}.

Since there was no superlattice ordering in the semiconductor layer of the device C, we used a double diode model (same as Fig. 6.5 without D_3) with two parallel and a series resistance for the simulation of the I-V curves. The two diodes connected back to back correspond to the two schottky contacts. So for such an electrical equivalent the current in the subcircuit 2 (6.4c) modifies as

$$I = -I_{02}\left(e^{\frac{V_2}{\eta_2 v_t}} - 1\right) - \frac{V_2}{R_{p2}}$$

Thus the voltage drop in subcircuit 2 reads as

$$V_2 = R_{p2}(I_{02} - I) + \eta_2 v_t W\left(\frac{I_{02}R_{p2}}{\eta_2 v_t} e^{\left[\frac{(-I+I_{02})R_{p2}}{\eta_2 v_t}\right]}\right)$$

So, the terminal voltage as a function of the total current leads to

$$V = R_{P1}(I + I_{01}) - \frac{\eta_1 kT}{q} W\left[\frac{R_{P1}I_{01}}{\eta_1 kT} exp\left\{\frac{R_{p1}}{\eta_1 kT}(I + I_{01})\right\}\right] + R_{P2}(I - I_{02}) +$$
$$\frac{\eta_2 kT}{q} W\left[\frac{R_{P2}I_{02}}{\eta_2 kT} exp\left\{\frac{R_{p2}}{\eta_2 kT}(I_{02} - I)\right\}\right] + IR_s \qquad 6.7$$

Similar to the case of the devices with superlattice structures here the parameters to be extracted are φ_{B1}, φ_{B2}, R_s, η_1, η_2, R_{p1}, R_{p2}.

Therefore, Eq. 6.6 and 6.7 would describe the terminal voltage as an explicit function of the total current through the device. However, to find an analytical solution for the terminal current as a function of the terminal voltage is much more difficult. Despite this, the expression is very useful to find the I-V relationship avoiding approximations or iterative numerical procedures. For simulation in presence of light, the same equations have been used with the parameters modified accordingly. Furthermore, we analyzed the three figure of merits viz. responsivity (R), detectivity (D) and photosensitivity (S). The responsivity is expressed as [26,162]

$$R = \frac{I_{ph}}{PA} = \frac{I_l - I_d}{PA} \qquad 6.8$$

In general, detectivity is defined as D = $(AB)^{1/2}$/NEP. A, B are the effective area and the bandwidth of the detector, respectively. NEP is the noise equivalent power given by i_n/R where in is the noise current and R, responsivity. However, it is customary to express D taking the bandwidth as unity and i_n as the dark current i_d [162], then

$$D = \sqrt{\frac{I_{ph}^2}{2qAP^2 I_d}} = R\sqrt{\frac{A}{2qI_d}} \qquad 6.9$$

The photosensitivity or simply sensitivity is another important parameter expressed as

$$S = \frac{I_{ph}}{PI_d} = \frac{RA}{I_d} \qquad 6.10$$

where, I_l is the total current under illumination, I_d is the dark current, P is the power of the incident radiation per unit area, and A is the effective area of illumination, q is the electronic charge. It is to be noted that higher the value of the above quantities (R, D and S), higher will be the performance of the photodetector. The variation of the figure of merits with wavelength as well as applied bias were studied. Another important parameter for a photodetector is the temporal response. The time elapsed for rise and decay in photocurrent with application of a pulsed optical signal under proper biasing condition indicates how fast the photodetector responds to optical signals. The frequency range of the input signal, the detector can detect, is also important for the application of the device. The rise and decay time of a photodiode is defined as the time for the signal to rise or fall from 10% to 90% or vice versa of the final value respectively. The time response can also be expressed as frequency response, defined by the frequency (f_{3dB}) at which the photodiode output decreases by 3 dB which can be roughly approximated by [163],

$$f_{3dB} \cong \frac{0.35}{\tau_r} \qquad 6.11$$

Where τ_r is the rise time of the photodetector.

6.5 Electrical properties and device performance

For the implementation of the device for photodetector application based on the superlattice structures and investigation of the device performance over the bulk AlGaAs, we fabricated three devices with the as-grown (A), 700 °C (B), and 900 °C (C) annealed sample. The configuration for

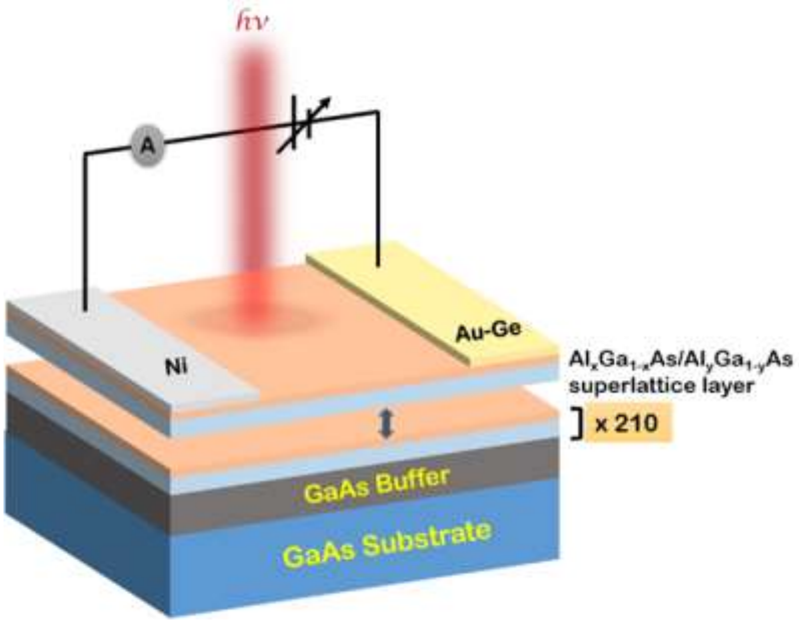

Fig. 6.6 Schematic representation of the device structure with Au-Ge and Ni contacts

the three devices remained same with one Au-Ge and another Ni contacts on the front face. The device structure with the two nonsymmetrical front contacts is shown in Fig. 6.6. It was evident from the measured I-V characteristics under dark that for the device with 900 ^{o}C annealed homogeneous AlGaAs, the dark current increased more rapidly with bias rather than that for the other samples as evident from Fig. 6.7. Presence of the periodically modulated superlattice structures acted to block the carriers in device A causing the dark current to decrease significantly, the dark current is relatively higher for device B could be due to the lowering of the compositional contrast as a result of annealing and the highest value of the dark current for device C is attributed to the absence of the superlattice barriers. Among the three devices, the device A possessed the lowest, followed a higher value for device B and the device C got the highest value of the dark current at any biasing voltage in the rage we studied. For any photodetector, the dark current should be lower for better performance. The experimental I-V curves along with their respective fitted ones using the corresponding models under dark for the three different devices for a sweeping voltage between

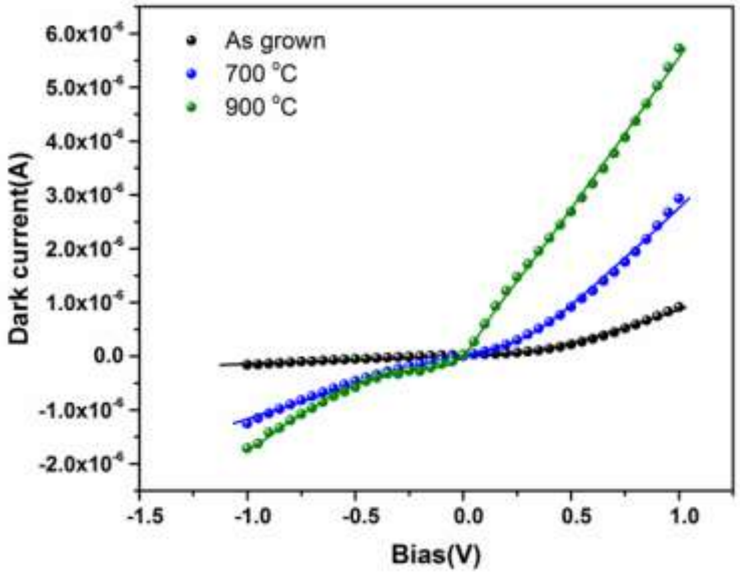

Fig. 6.7 Experimental (dotted) and fitted (solid line) I-V curves for the three devices i.e. the device A (black), B (blue) and C (green)

-1 to +1 V were shown in Fig. 6.7. The lowering of the dark current can be explained more elaborately by looking at the extracted parameters enlisted in Table 6.1.

Table 6.1 Extracted parameters from fitting of I-V curves under dark using the three diode model

Device	φ_{B1} (V)	φ_{B2} (V)	φ_{B3} (V)	η_1	η_2	R_s (Ω)	R_{p1} (Ω)	R_{p2} (Ω)
A	0.67	0.75	0.79	1.4	1.2	33.10	2.12×10^6	1.68×10^5
B	0.65	0.72	0.71	1.5	1.3	28.43	6.40×10^6	219×10^5
C	0.64	0.7	______	1.8	1.5	3.22×10^4	7.32×10^6	7.91×10^5

It is clear that the barrier heights at the two contacts (φ_{B1}, φ_{B2}) remain high, 0.67 and 0.75 V respectively, for the device A relative to the others because of the lowering of the bandgap due to the effect of the spontaneous ordering. The values of the barrier heights at the two contacts (φ_{B1},

$\varphi_{B2})$ were found to be (0.65, 0.72V) and (0.64 V, 0.7) for the devices B and C respectively. The barrier height φ_{B3} represents the net effect of the heterojunctions formed inside the semiconductor layer due to the superlattice structures which decreased from the as-grown to the annealed sample with increasing temperature as the compositional contrast was gradually decreasing due to interdiffusion in the epilayer. The intrinsic barrier height φ_{B3} takes the values 0.79 and 0.71 V for device A, and B respectively. Three devices were tested for photodetector application under illumination in a range of 400-900 nm from visible to near-infrared regime. The experimental as well as the corresponding fitted I-V curves for the three devices under illumination were shown in Fig. 6.8(a)-(c). For the device A, as shown in Fig. 6.8(a), the I-V curves showed a maximum enhancement of current near about 750 nm of illumination. For the devices B and C, shown in Fig. 6.8(b) and (c) respectively, the enhancement in photocurrent was maximum at 700 nm near the bandgap. The decrease in photocurrent beyond the wavelength correspond to the bandgap of the respective devices could be stated as follows. The photocurrent derived mainly form the electron–hole pairs excited by incident light having energy above the bandgap, indicating the sub-bandgap states make little contribution to the photocurrent [164]. Under light, the current enhancement was maximum for A which is nearly about 2 times higher than that of B. Although for C, the current enhancement was the lowest relative to the other two devices, it showed almost similar enhancement in photocurrent under both forward and reverse bias. The reason might be that the net effect was from two terminals and the contribution from the third diode was neglected due to the vanishing barrier (φ_{B3}) as a result of annealing. For the other samples, the enhancement was quite significant in the forward bias only. The extracted parameters by fitting the I-V curves under light of different wavelengths were analyzed to explain the device characteristics. Decrease in barrier heights, increase in ideality factors with wavelength up to a certain value and thereafter change in its nature indicated the contribution of only the excitonic transition related carriers to the photocurrent [164]. The variation of the extracted parameters with wavelength of the incident radiation were shown in Fig. 6.9(a)-(f). The barrier heights at the two contacts reached their minima at 750 nm for the device A and near about 700 nm for the other two devices. The change in φ_{B3} from 0.79 under dark to 0.6 under illumination of 750 nm was significant for the device with the as-grown sample. In presence of light, as the barrier heights started to decrease, carriers found parallel way through superlattice channels to flow smoothly between the terminals which were inactive, prevented flow of carriers under dark. This might be the reason for the sharp rise in current with applied voltage for the device A. The change in φ_{B3} was relatively less for the device B, from 0.71 under dark to 0.65 under 700 nm of illumination. Application of light resulted in a change in the two barrier heights possessing minima of 0.6 and 0.62 V for the Au-Ge and Ni junctions, respectively near 700 nm of wavelength for the device C. The change in barrier height at the contacts could be attributed to the presence of more number of interfacial traps in case of the device C [26]. On the contrary, as there existed no extra channel activated under illumination, current enhancement remains the lowest of all. The ideality factors increased with increasing wavelength, attained the maximum at 750 nm and decreased again for the device A. For both the

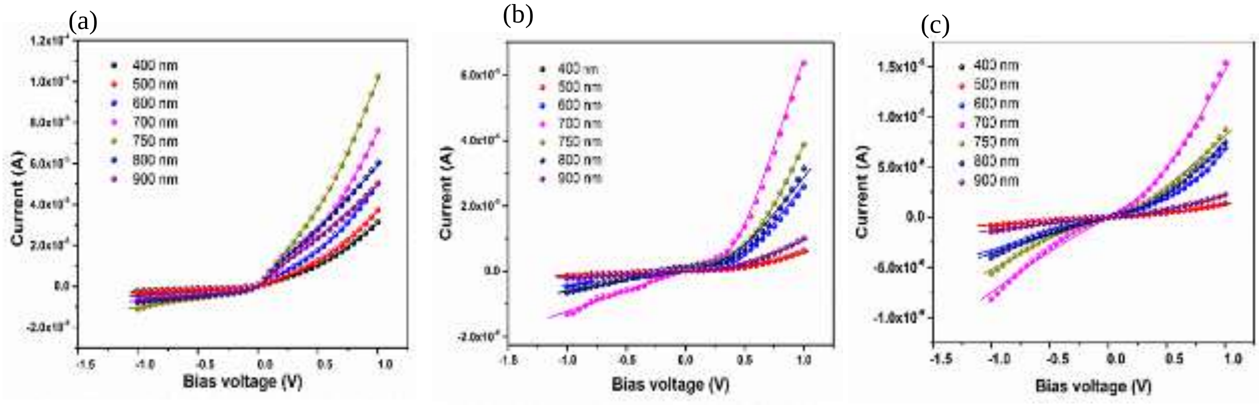

Fig. 6.8 (a), (b), (c) Experimental (dotted) and fitted (solid line) I-V curves at different wavelengths for device A, B and C respectively

devices B and C, the barrier heights and the ideality factors showed almost same nature as those for device A, except the fact that the minima of the barrier heights and maxima of the ideality factors were at about 700 nm. Under illumination, during the separation process, the

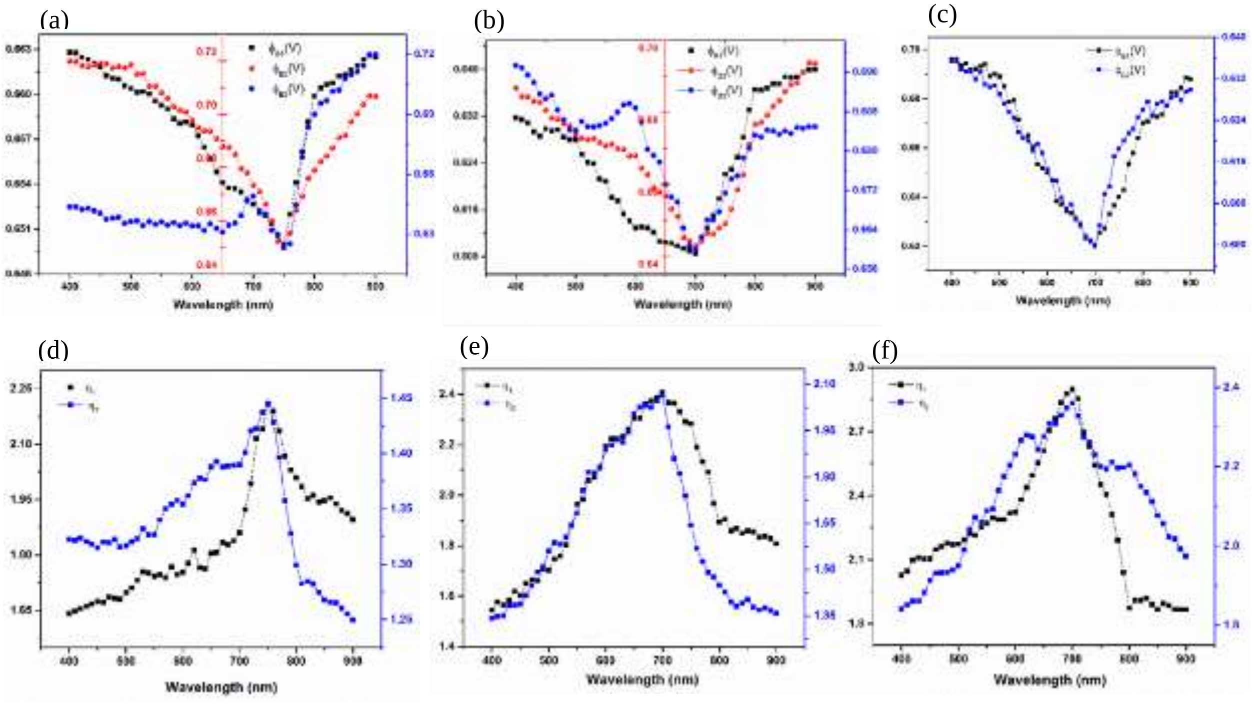

Fig. 6.9 (a), (b), (c) Variation of the extracted barrier heights and (d), (e), (f) variation of the ideality factors with wavelength of the incident radiation for device A, B and C respectively

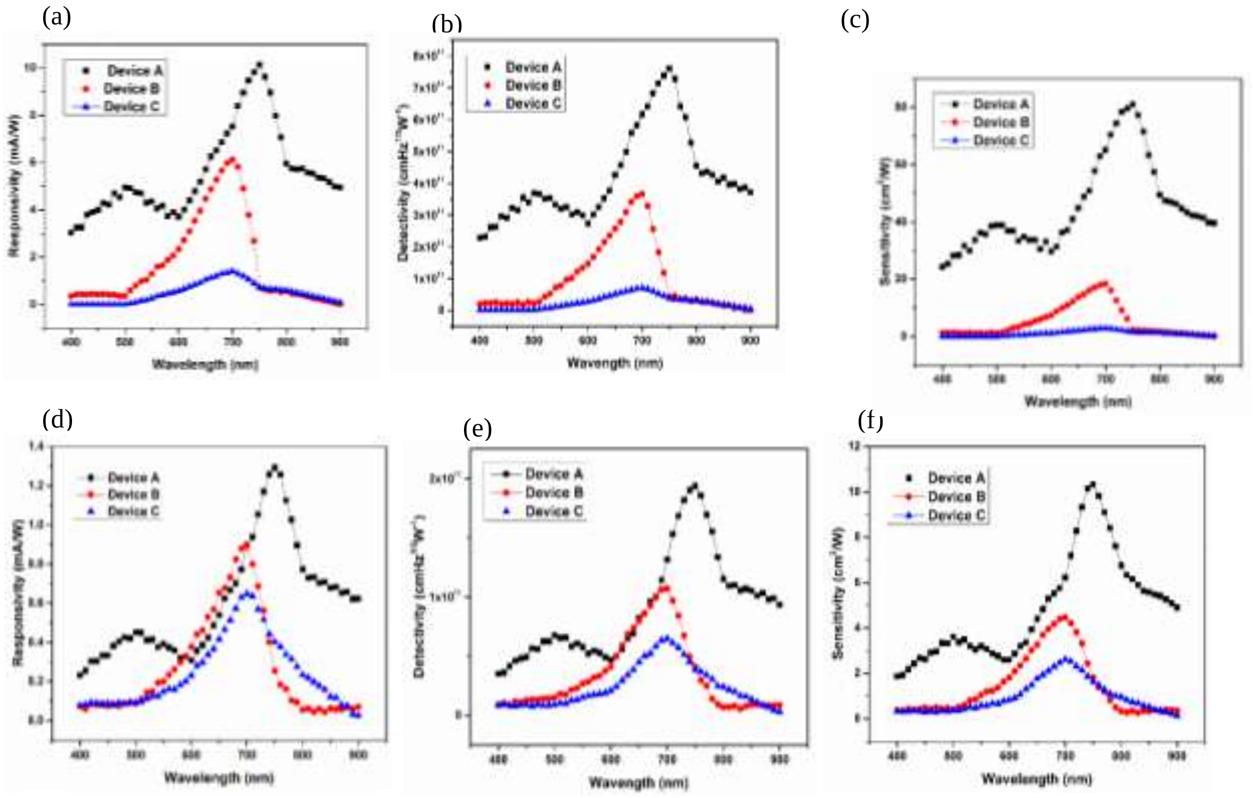

Fig. 6.10 (a) Responsivity (R), (b) Detectivity (D), (c) Sensitivity (S) with illumination wavelength (λ) under 1 V and (d), (e), (f) under -1 V, respectively, for the devices A (black), B (red) and C (blue)

photogenerated carriers eventually recombined via the deep level trap states to make them empty resulting in effective increase of the defect states. These increased vacant states were responsible for effective lowering of barrier heights and further increase of ideality factors [165]. To understand the performance of the photodetectors, we evaluated the three figure of merits from the I-V measurements. The variation of the photoresponsivity, detectivity and the sensitivity at fixed applied bias of 1 V and -1 V for all the three devices are shown in Fig 6.10(a)-(f). The photoresponsivity spectrum showed that the photodetector could detect signal efficiently in the visible-NIR (600-800 nm) regime of the electromagnetic spectrum. All the three figure of merits peaked at 750 nm for device A and near about 700 nm for both B and C. Under 1 V of forward bias, the peak values were 10.13, 6.12 and 1.14 mA/W for A, B and C respectively. The peak responsivity was maximum for the device A due to significant enhancement of photocurrent under light. The device B, annealed at 700 ^{o}C, a comparatively poor distorted superlattice sample due to the effect of interdiffusion, showed a relatively poor responsivity. The device C, annealed at 900 ^{o}C, showed very poor responsivity with a peak which was blue shifted due to bandgap shrinkage caused by ordering. Under reverse voltage of 1 V, the peak values of responsivity were 1.29, 0.89 and 0.64 mA/W for A, B and C respectively, almost one order lower in magnitude than in case of forward bias. The other two figures of merit showed similar behavior as a function of wavelength for all the devices. The peak values of detectivities were found to be 7.6×10^{11}, $3.6\times10^{11}$and 7.05×10^{10} cmHz$^{1/2}$W^{-1} under 1 V of forward bias and 1.93×10^{11}, 1.07×10^{11} and 6.48×10^{10} cmHz$^{1/2}$W^{-1}under 1 V of reverse bias for A, B and C, respectively. Similarly, the peak sensitivities were 81.06, 18.37 and 2.82 cm^{2}/W under forward bias and 10.33, 4.46, 2.59 cm^{2}/W under reverse biased conditions. So, device A showed better performance than B and C under both forward and reverse biased conditions. Although not much change in responsivity, but a significant degradation in detectivity as an effect of thermal treatment for InGaAs/GaAs quantum dots has been reported previously by Fu *et al.* [166]. One noticeable thing is that for the devices with superlattice structures (A and B) showed better performance under forward bias but device C showed similar performance under both forward and reverse bias. This could be due to the fact that the two terminal diodes played dominating role over the third diode here under light. Three figures of merit were also plotted against the applied bias for a fixed wavelength of 750 nm for the device A and 700 nm for the devices B and C as shown in Fig. 6.11(a)-(c). As we increased the bias in both the directions, the photoresponsivity increased with applied bias following the behavior of the photocurrent. The detectivity, which is basically a combination of both the current under the photon flux and the dark current, increased with the applied bias but at a slower rate than the responsivity. The sensitivity increased initially and then decreased in the total range of the applied bias. This could be the effect of saturation of the photocurrent owing to a finite number of the photogenerated carriers but increase in the dark current with the applied bias. The external quantum efficiency (EQE) was also calculated for the three samples using the relation

$$e_{\lambda}=Rhc/q\lambda \qquad 6.12$$

where R is the responsivity defined earlier, h is the Planck's constant, 6.63×10^{-34} Js, c is the speed of light in free space, 3×10^{8} m/s, q is the electronic charge, $1.6\times10\text{-}10^{-19}$ C and λ is the wavelength of the incident light. The peak values were 0.016 for the device A at 750 nm and 0.01, 0.002 for sample B and C respectively, at 700 nm. Since there was no evidence of any degradation of the crystalline quality or desorption from the surface due to the heat treatment, we can conclude that the enhancement in the device performance is purely due to the superlattice ordering in the material [28].

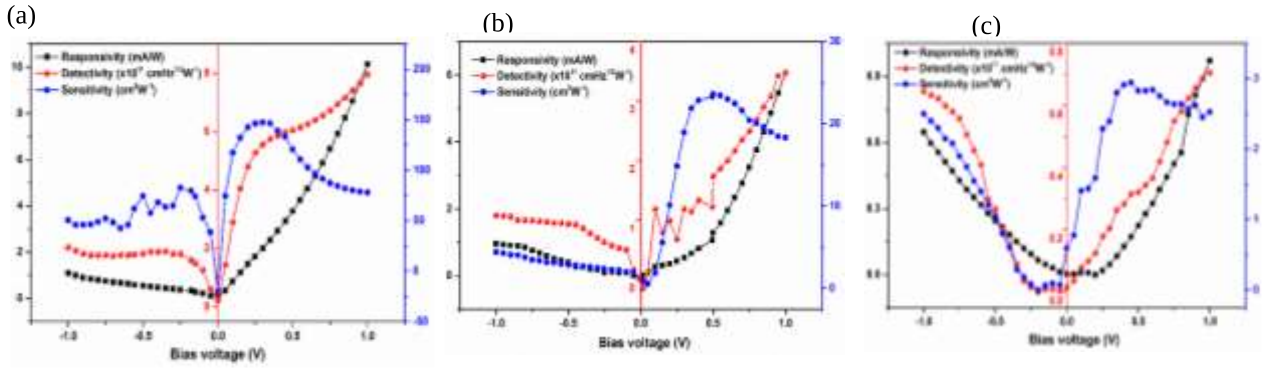

Fig. 6.11 Responsivity (R), Detectivity (D) and Sensitivity (S) with bias for devices (a) A, (b) B and (c) C under the illumination of their respective peak response

The time response of a photodetector to switching frequency determines its capability to follow a fast-varying optical signal, which is particularly important in light-wave communication and optical switching applications. We focused our attention on the ordering induced enhancement in the response of a superlattice photodetector relative to the bulk. So, the device A (as-grown superlattice structure) has been compared with the device C (homogeneous composition) to have an idea of the effect of the order-disorder transition on the device response. Fig. 6.12(a) showed the reversible switching of the two devices between the low and the high conductance states when light was turned off and on, respectively. The ideal photocurrent for the light signal fed by a square pulsed signal of frequency 50 Hz with a duty cycle of 50 % was also shown in the figure for reference. The rise time and decay time for the device A has come out to be 560 μs and 1 ms respectively, whereas those for the device C were obtained as 2 ms and 7 ms. A comparative study of response time with respect to different photodetectors fabricated using various materials is enlisted in Table 6.2. Here, we have compared the response speed of our device with those made of other materials working on nearly the same range of the electromagnetic spectra. Sometimes the geometry of the devices may differ. Sometimes, the area of illumination may differ. The absolute value of the photocurrent level between the "ON" and the "OFF" state may also differ depending on the semiconductor material and the metals used as the electrodes, although the "OFF" and the "ON" states are scaled to 0 and 1, respectively. It is true that for exact comparison all the device parameters must be exactly same. However, our device could be a simple but effective one because of the spontaneously formed superlattice layers. The AlGaAs photodetector based on the natural superlattice has the potential to complete the available devices with different materials for Vis-NIR photodetection. The output waveform of current of the Au-Ge/AlGaAs/Ni photodetectors remained almost unaltered after several cycles, indicating the excellent stability of the photodetector. The frequency response expressed in terms of f_{3dB} were evaluated to be 625 and 175 Hz for the devices A and C, respectively. Furthermore, the photodetector based on the

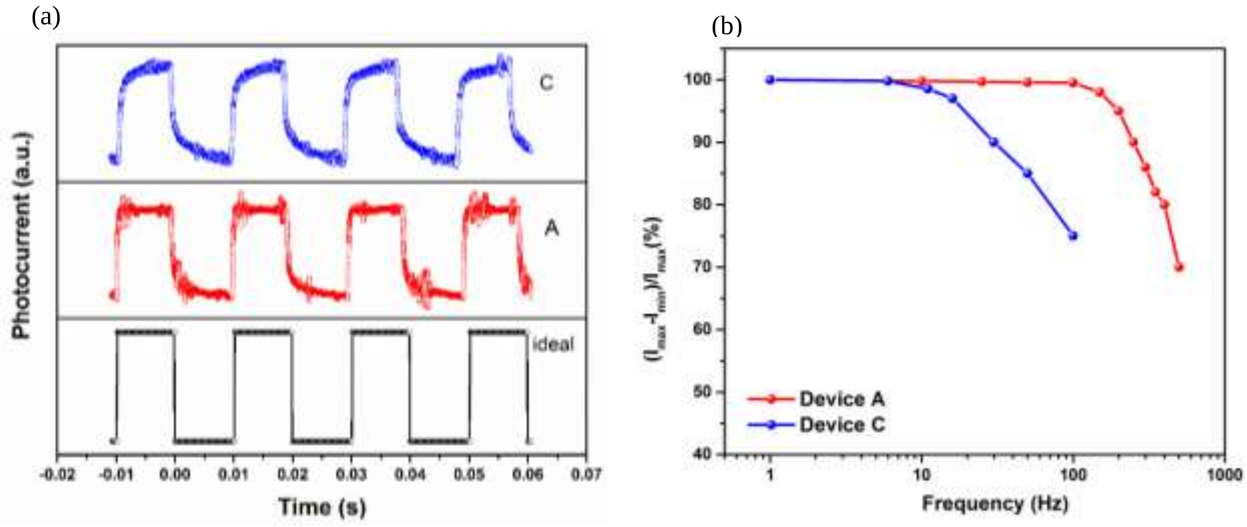

Fig. 6.12 (a) Ideal step photocurrent and the time response of device A and C under application of square pulsed illumination (b) relative balance ((I_{max}-I_{min})/I_{max}) vs switching frequency of device A (black) and C (red) showing a much better response for the device A up to a higher frequency

superlattice structure was found to work with excellent stability and reproducibility in a wide range from 1 to 200 Hz. The device C worked well in a relatively shorter frequency ranging from 1 to 30 Hz. The measure of the reproducibility could also be expressed by the relative balance ((I_{max}-I_{min})/I_{max} in %) vs switching frequency plot as given in Fig. 6.12(b) which showed that the relative balance dropped below 80% (below which the device lost reliability) after 400 Hz and 50 Hz for devices A and C respectively. A photodetector will be more reliable as it shows the relative balance stable up to a higher frequency of operation [164]. As the photodetector based on the superlattice structures shows a fast response in comparison with that with homogeneous AlGaAs to the pulsed light, it is reasonable that the former shows the stability of the relative balance value up to a higher frequency of operation. This could be attributed to the high quality of the interfaces between the superlattice layers in the as-grown sample. The activation and deactivation of the superlattice channels in presence and absence of light, respectively, improve the reproducibility and reliability of the photodetector up to higher frequency.

Table 6.2 Comparison of the response time of photodetectors with different materials

Sample name	Time of rise	Time of decay	f_{3dB} (Hz)	Reference
AlGaAs superlattice	560 μs	1 ms	625	[28]
AlGaAs bulk	2 ms	7 ms	175	[28]
CZTS	391 ms	221 ms	0.895	[167]
Na doped CZTS	1.02 ms	29.8 ms	343	[167]
Au/ZnO/Au	100 ms	1 s	3.5	[168]
SnO_2 nano-particle thin film /SiO_2/p-Si	100 ms	70 ms	3.5	[169]
WS_2/Si van der Waals Heterojunction	670 μs	998 μs	522.3	[170]
	330 ms	0.986 ms	1.06	[171]
$Cu_2ZnSn(S, Se)_4$	208 ms	178 ms	1.68	[172]
Cu_2ZnSnS_4	681 ms	778 ms	0.51	

6.6 Summary

We have established that the difference observed in the material properties could be solely attributed to the superlattice ordering, based on the study of the surface through scanning electron microscopy (SEM) and structural studies through elemental mapping in XTEM and XRD measurements of the ordered and the disordered samples [28]. The shift in the transition energy and the enhancement in the PL intensity has been solely attributed to the natural superlattice ordering. The change in the electrical properties can be explained by considering the effect of the superlattice layers on the carriers as follows. During the formation of superlattice structure with periodic variation of Al concentration, the electrons move from the side with higher Fermi level to the other and as a result, an electric field was produced at interfaces between the layers with periodically modulated Al content. Thus, the extended intrinsic electric field existing inside the semiconducting region at the bilayer interfaces, although very weak due to low compositional contrast, somehow was able to help the carriers to be swept out as soon as they are generated there under the illumination for the MSM devices with the superlattice structures. Presence of internal electric field inside results in smaller timescale for the rise of photocurrent compared to C where there was no intrinsic electric field. The photocarriers generated in the semiconductor region of device C take more time to diffuse to the metal-semiconductor contacts which results in the rise for a relatively longer time. Similarly, when the light was switched off, the motion of the carriers hindered by the intrinsic barriers in the semiconductor region junction results in a relatively faster decay for device A whereas the current needs much longer time to fall to its minima for device C. The fast rise of photocurrent of both the devices followed by a relatively slow decay which could be understood by looking at the trapping-detrapping process of the carriers. As soon as the device is illuminated with light having a sufficient amount of energy, electron-hole pairs are generated in the semiconductor region. These photocarriers are then separated by the built-in electric field and partly contribute to the photocurrent. For simplicity, we have considered the trap-centers at two metal-semiconductor interfaces with a higher probability of electrons to be captured rather than

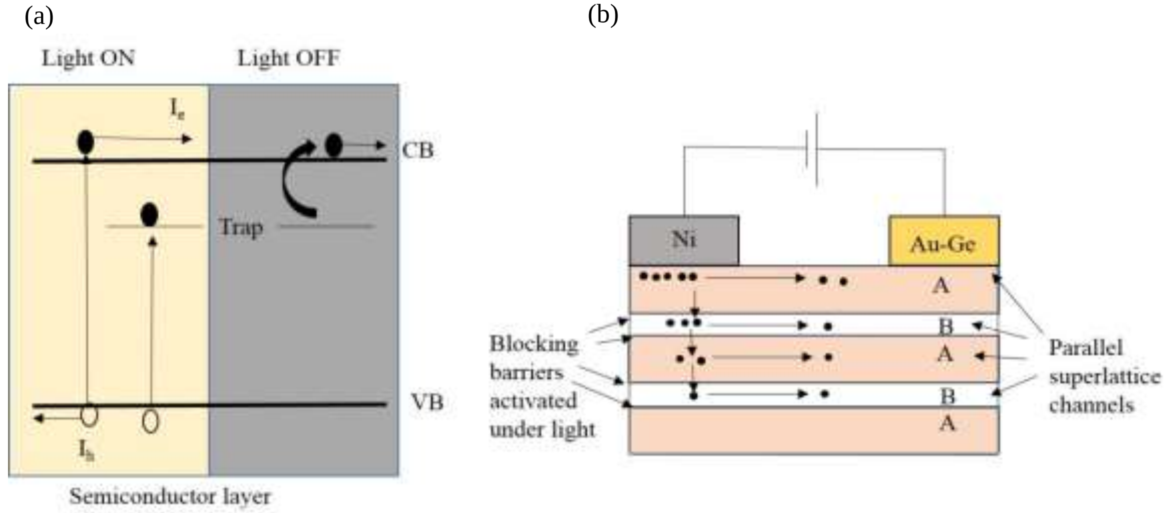

Fig. 6.13 (a) Schematic representation of the trap assisted switching process (b) Motion of the carriers through the superlattice channels

holes due to the Schottky barriers. Some of the electrons in the conduction band (CB) might be captured by the electronic traps. When the light is switched off, the part of the trapped photoelectrons would be gradually released to the conduction band and contribute to the electrical conduction and then are finally recombined with the photogenerated holes. Thus, the trap-states associated decay of photocurrent is slower than the rise. A model representing the trap-assisted carrier dynamics for light "ON" and "OFF" conditions is shown in Fig. 6.13(a). The entire region can be divided into three parts of which two correspond to the band bending regions at Au-Ge and Ni junctions, whereas the third one represents the net effect due to the periodic structures in the AlGaAs epilayer. The mismatch in Fermi level at the AlGaAs/AlGaAs heterojunctions with different Al composition is responsible for an intrinsic electric field. These barriers restrict the current flow under the dark condition giving a low value of the dark current. As soon as light falls on the semiconducting material region, the sweeping of the photogenerated carriers get easy pathways owing to the intrinsic electric field at the superlattice junctions under proper biasing conditions. After the light is turned off, the carriers get localized inside the superlattice channels due to the barriers that in turn makes the current to decay to its minimum within a small interval. A schematic representation for the motion of the carriers is shown in Fig. 6.13(b). This makes the photodetector based on the superlattice structure performance better by significant enhancement of photocurrent, and at the same time, faster too although during the separation process, the loss of photo generated electron-hole pair due to recombination at the two junctions, limited the photodetector performance to some extent.

Chapter 7

Conclusion

7.1 Summary of the work

The results of the work we have done so far through this tenure have been covered mainly in chapters 4, 5 and 6 of the thesis. In this work, we have concentrated on the natural superlattice ordering, its thermal stability, and the utilization of it in device fabrication, for the particular Al compositions of 0.3 and 0.15. As our idea was to utilize the material for the optoelectronic application, we look for the material with a direct bandgap. We have concentrated to grow AlGaAs with nominal Al content below 0.4 not only for the direct bandgap but also for the negligible lattice strain looking at the suitability of the material for optoelectronic device application. We have grown GaAs/AlGaAs MQW structures on GaAs (100) substrate for optoelectronic device applications using MOCVD technique [28]. We had observed a periodic compositional modulation in the AlGaAs barrier layer with a nominal Al fraction of 0.3 whose repetition length was about 5.4 nm, i.e., nearly around 20 monolayers of the material. To confirm the occurrence of such structures in the bulk, we have grown about 1132 nm thick AlGaAs epilayer with a targeted Al fraction of 0.15 on the conventional (100) GaAs substrate. Similar type of superlattice ordering was found in the bulk epilayer from TEM and X-ray analyses. The TEM and X-ray results were matched to confirm the periodicity. X-ray results were used to get the electron density and lattice parameter profile of the superlattice structure. Finally, we obtained the in-depth profile of composition through a combinatorial approach involving low angle XRR and high angle (004) XRD simulations. So, in the regime of our interest, the stability of ordering has been investigated for a low concentration as well as a high concentration under the similar growth conditions. Then we looked for the structural stability of such natural superlattice ordering for device application. We have studied the stability under thermal treatment by heating the as-grown sample up to a temperature of 900 ^{o}C. For temperature till 800 ^{o}C, the structures remained stable and showed a transformation into the disordered phase retaining its crystallinity intact at 900 ^{o}C of annealing, as confirmed by the high temperature (004) XRD measurements. Since the interface between the superlattice layers always plays an important role in the device characteristics, thermal diffusion in the spontaneously grown ultra-nanoscale ordered structures has been studied in detail. In absence of suitable direct experimental tools due to the physical resolution limit, we relied on the theoretical analysis of x-ray diffraction simulations coupled with a virtual diffusion experiment to arrive at the interdiffusion characteristics across the interfaces of spontaneously grown $Al_xGa_{1-x}As/Al_yGa_{1-y}As$ superlattice structures. The simulation approach presented here is a combination of an interdiffusion code and a code on x-ray diffraction around the (004) Bragg peak based on Born approximation. We have obtained the variation in the actual diffusion coefficient as a function of time at different temperatures from the decay rates of the integrated intensity of the first order satellite peak. We found the diffusion coefficient across the interface to be highly nonlinear and also composition dependent. The satellite decay equation could fit the experimental data taking the maximum Al composition alone at each time step. The pre exponential factor (D^o) and the activation enthalpy (H) values for interdiffusion were found out to be 0.17-0.25 cm^2/s and 0.5-0.6 eV for Al diffusion whereas 0.01-0.11 cm^2/s and 3.45-3.5 eV for Ga diffusion, respectively in the studied temperature range of 500 ^{o}C to 700 ^{o}C. The interdiffusivity increased with temperature from 500 ^{o}C to 625 ^{o}C and decreased for further rise in temperature as the compositional contrast between the two layers decreased significantly (reached a certain critical value) at higher temperatures. After studying the fundamental properties of the structures, we studied the effect of the natural superlattice ordering in such length scale on the optical and electrical properties of the material. Our aim was a systematic investigation of the effect of annealing on the microscopic structures of the spontaneous superlattice and also the optical properties and the device performance and to establish the correlation between the structural and the optical and electrical properties of the natural superlattice ordering. Besides, at the same time, we have done a comparative study using the ordered and thermally annealed disordered sample to understand the effect of the superlattice ordering on the optical and electrical properties of the material. Normally, high-temperature annealing can significantly modify the morphology of the materials and defects may be incorporated unintentionally. Keeping such possibilities in mind, we have examined the as-grown and the annealed samples through SEM, XTEM and XRD measurements to comment on their structural quality. The structural analyses for the as-grown and the annealed samples have shown no significant evidence of the surface damage, degradation of the crystalline quality or incorporation of unnecessary defects. Therefore, the modified optical and electrical characteristics could solely be attributed to the natural superlattice ordering. Temperature dependent photoluminescence showed a redshift of 34 meV in the transition energy for the ordered structures with respect to the bulk material with the same composition, due to repulsion between the states in valance and conduction band as a result of the overlap of k-points for the increased periodicity of the crystal lattice in real space. The bandgap reduction as a result of ordering was found to be very similar to the case of atomic ordering reported previously in different compound semiconductor materials during epitaxial growth from vapor phase [173]. The decay of photoluminescence intensities with temperature were fitted with the modified Arrhenius equation for both the samples. The two excitonic binding energies come out to be 9.87, 43.09 and 5.07, 35.36 meV for the As-grown and the annealed samples, respectively. Two binding energies suggest activation of the excitons through two different channels at lower and higher temperature regions. The higher values of the binding energy in case of the ordered sample is basically showing the effect of confinement of the carriers in the superlattice layers which enhances the stability of the excitons in the superlattice channels as compared to the disordered sample. As a part of device application, we developed photodetector for working in the NIR regime of the electromagnetic spectrum, based on the spontaneously grown superlattice structures. In general, MSM PDs have two comb-like electrodes with 1 μm spacing. In the absence of photolithographic technique in our laboratory to form such electrodes, we have concentrated on the fabrication of co-planar metal-semiconductor-metal back to back Schottky diode photodetector with natural superlattice ordering in the active semiconductor layer, due to its geometrical simplicity and high response. For comparison on the basis of the device performance regarding the spectral and temporal response, we developed other devices with the same geometry of the contacts with the 700 ^{o}C annealed superlattice and also 900 ^{o}C homogeneous AlGaAs as the active layer. Device parameters were extracted using electrical equivalent Schottky diode model using an extra diode representing the superlattice layer. By employing Lambert W function for fitting the experimental I-V measurements with the help of the diode models, we evaluated three figures of merit such as responsivity, detectivity and sensivity for all the devices. In this dissertation, for fitting of the experimentally obtained data with the calculated ones using several theoretical models as discussed in the respective sections, we have employed standard nonlinear curve fitting algorithm and found the $\chi 2$ value reliable within 1%, which seems very much appreciable. The extracted parameters, most importantly, the Schottky barrier heights showed the reason for the device based on the superlattice structures to perform better. Under a forward applied voltage of 1 V, the peak values of responsivity, detectivity and sensitivity were 10.13 mA/W, 7.6×10^{11} cmHz$^{1/2}$W^{-1}, 81.06 cm^{2}/W and 1.14 mA/W, 7.05×10^{10} cmHz$^{1/2}$W^{-1}, 2.82 cm^{2}/W for the device based on the as-grown natural superlattice and homogeneous AlGaAs, respectively. Furthermore, the as-grown device also showed superiority in the temporal response also with the application of a pulsed optical signal. The device with natural superlattice ordering showed much faster response to the square wave pulsed light with rise and decay time of 560 μs and 1 ms as compared to 2 and 7 ms, respectively, for the device with homogeneous AlGaAs. The superior spectral and temporal characteristics of the devices are explained by the model based on a third diode representing the net effect due to the superlattice modulations along with two Schottky diodes at the metal-semiconductor junctions. The third barrier, which is basically due to the periodic modulation in aluminium composition, plays a vital role in enhancement of the photocurrent as a result of the activation of superlattice channels under light while keeping the dark current small by blocking the carriers without light. The fast sweeping of the photo-carries by the intrinsic small but effective electric field at the compositionally modulated interfaces in the active semiconducting layer makes the characteristic times of the device much smaller than one with homogeneous AlGaAs. Degradation in photoresponse and speed is attributed to decrease in the compositional contrast and the increase in the interfacial width due to the interdiffusion as an effect of thermal annealing. Besides, a range of wavelength for photodetection could be covered by using the superlattice structures annealed at different temperatures, with reasonable efficiency also. A comparative study shows that our device could be a simple but effective one because of the spontaneously formed superlattice layers. The AlGaAs photodetector based on the natural superlattice has the potential to complete the available devices with different materials for Vis-NIR photodetection.

7.2 Conclusion and future outlook

Spontaneous ordering in AlGaAs in such multiple monolayer length scale was observed on conventional (100) GaAs substrate grown by MOCVD in the barrier layer of MQW and bulk material despite the small bond length difference between the constituent binaries. The well observed and previously reported CuAu type monolayer ordering could be explained by the surface reconstruction to minimize the surface free energy. Although the origin of the of the ordering is not very clear at the present time, the existence of such spontaneously grown structures in the bulk material could depend on the surface thermodynamics for the formation, whereas the growth temperature inside the reactor and the growth rate decided the stability of the ordering inside the bulk. Since we have observed such a new kind of partial ordering in AlGaAs on the conventional GaAs substrates, the existence of the structures could be studied with various growth parameters like growth temperature, substrate orientation and flow rate for better understanding the origin and nature and stability of such ordering in future. It will be interesting to study how the atomically ordered layers can be changed to layers with random alloying with homogeneous concentration throughout by changing the growth parameters, and also whether there is a limit of nominal Al content to form such ordering in the full composition range of our interest. Furthermore, it would be interesting to study whether such natural superlattice ordering could form with other elements also for some particular growth condition such as flow rates of the precursors, temperature, substrate orientation etc. MOCVD, being a vapor phase epitaxial technique, has always an important role in the formation of such ordered structures and stabilize it well inside the material. It might be possible that such ordering could also form during the MBE growth but that needs further study. As the structure showed reduction in the bandgap similar to the case of monolayer ordering, the structure could be used to develop quantum heterostructures such as quantum well by growing order and disorder phase sequentially on the same material, just changing the growth parameters. The stability of such structures after thermal treatment is very important as most device applications need high temperature treatment. We have developed a model to thoroughly study the inter-diffusion characteristics in superlattice structures by employing high temperature X-ray scattering. We deduced the behavior of the diffusion coefficient at five different temperatures and showed concentration dependence of the diffusion coefficient in the material. The model can also be used to explain the interdiffusion process in various artificial superlattice structures of different length scales. Photoluminescence can also be employed to extract the interdiffusion characteristics as it shows significant modification in the transition energy. Then, the results from the XRD and PL can be compared in regard to the diffusion in the natural superlattice. The optical characteristics of the natural superlattice has also revealed a significant enhancement in the intensity of the transition. The intensity of the photoluminescence which depends on the carrier density and the radiative recombination rate depends on the degree of ordering. Theoretical background of the enhancement of the photoluminescence intensity i.e. the optical gain as an effect of ordering is still an open field for research. The polarization dependence of the emitted radiation for such newly observed natural ordering could also be interesting to study. The effect of ordering on the carrier concentration due to the zone folding and consequent splitting of the band energy can also be investigated in the future. From the device perspective, the implication of the superlattice structures in the metal-semiconductor-metal photodetector device showed a betterment in the device performance. The main advantage is that the natural superlattice constrained the dark current through the heterointerfacial barriers between the compositionally modulated structures, and on the other hand enhanced the overall gain by increasing the photocurrent through the activation of the superlattice parallel channels for the photogenerated carriers in presence of light. The response speed of the device also showed superiority by getting influenced due to the development of the intrinsic electric field at the heterointerfaces. The superlattice and such ordered-disordered structures mentioned above could also be used in various optoelectronic devices such as intermediate band solar cells, broad band photodetectors, quantum cascade lasers due to its better optical and electrical quality relative to bulk.

Bibliography

[1] Fowler A 1997 On some modern uses of the electron in logic and memory *Phys. Today* **50** 50–4

[2] Mokkapati S and Jagadish C 2009 III-V compound SC for optoelectronic devices *Mater. Today* **12** 22–32

[3] Konstantatos G and Sargent E H 2010 Nanostructured materials for photon detection *Nat. Nanotechnol.* **5** 391–400

[4] Stringfellow G B 1982 Epitaxy *Reports Prog. Phys.* **45** 469–525

[5] Beuchet G 1985 Semiconductors and Semimetals *Academic Press, Orlando* ed W T Tsang (Academic Press, Orlando) pp 261–98

[6] Foxton C T 1994 Handbook of Crystal Growth *Elsevier, Amsterdam* pp 155–81

[7] Manasevit H M and Simpson W I 1969 The Use of Metalorganics in the Preparation of Semiconductor Materials *J. Electrochem. Soc.* **116** 1725–32

[8] Razeghi M 2010 *Technology of Quantum Devices* (Springer, Boston)

[9] Fukuda M 1999 *Optical Semiconductor Devices* (John Wiley and Sons, Newyork)

[10] Adachi S 1994 *GaAs and Related Materials: Bulk Semiconducting and Superlarttice Properties* (World Scientific)

[11] Adachi S 1993 *Properties of Aluminium Gallium Arsenide*

[12] Tsui D, Stormer H and Gossard A 1982 Zero-resistance state of two dimensional electrons in a quantizing magnetic field *Phys. Rev. B* **25** 1405–7

[13] Sirtori C, Kruck P, Barbieri S, Collot P, Nagle J, Beck M, Faist J and Oesterle U 1998 GaAs/AlxGa1-xAs quantum cascade lasers *Appl. Phys. Lett.* **73** 3486–8

[14] Peters M, Thibeault B, Young D, Scott J, Peters F, Gossard A and Coldren L 1993 Band-gap engineered digital alloy interfaces for lower resistance vertical-cavity surface-emitting lasers *Appl. Phys. Lett.* **63** 3411–3

[15] Andersson J Y and Lundqvist L 1991 Near-unity quantum efficiency of AlGaAs/GaAs quantum well infrared detectors using a waveguide with a doubly periodic grating coupler *Appl. Phys. Lett.* **59** 857–9

[16] Nakagawa T, Imamoto H, Kojima T and Ohta K 1986 Observation of resonant tunneling in AlGaAs/GaAs triple barrier diodes *Appl. Phys. Lett.* **49** 73–5

[17] Suzuki T Basic Aspects of Atomic Ordering in III–V Semiconductor Alloys ed A Mascarenhas

[18] Kuan T S 1989 Encyclopedia of Physical Science and Technology *Academic Press Inc. San Diego* ed R A Meyers (Academic Press Inc. San Diego)

[19] T.S.Kuan, T.F.Kuech, W.I.Wang, and E.W.Wilkie, 201(1985) 1985 Long-range order in AlxGa1-xAs *Phys. Rev. Lett.* **54** 201–4

[20] Kuan T S, Kuech T F, Wang W I and Wjlk E L 1985 Long Range Order in AlxGa1-xAs *Phys. Rev. Lett.* **54** 201–4

[21] Pradhan A, Maitra T, Mukherjee S, Mukherjee S, Nayak A, Satpati B and Bhunia S 2018 Spontaneous superlattice structures in AlxGa1−xAs/GaAs (1 0 0) grown by metalorganic vapor phase epitaxy *Mater. Lett.* **210**

[22] Sharma M, Sanyal M K, Mukhopadhyay M K, Bera M K, Saha B and Chakraborty P 2011 Structural and morphological characterization of molecular beam epitaxy grown Si/Ge multilayer using x-ray scattering techniques *J. Appl. Phys.* **110** 0–5

[23] Maitra T, Pradhan A, Mukherjee S, Mukherjee S, Nayak A and Bhunia S 2019

Evaluation of spontaneous superlattice ordering in MOCVD grown AlxGa1-xAs epilayer on GaAs (100) using X-ray re fl ectivity and rocking curve analysis *Phys. E Low-dimensional Syst. Nanostructures* **106** 357–62

[24] Fatah J M, Harrison P, Stirner T, Hogg J H C, Hagston W E, Fatah J M, Harrison P, Stirner T, Hogg J H C and Hagston W E 2003 Double crystal x-ray diffraction simulations of diffusion in semiconductor microstructures Double crystal x-ray diffraction simulations of diffusion in semiconductor microstructures **4037** 10–5

[25] Pradhan A, Mukherjee S, Maitra T, Nayak A and Bhunia S 2019 Interface intermixing and interdiffusion characteristics in MOVPE grown spontaneous AlxGa1-xAs/GaAs (100) superlattice structures using high resolution X-ray diffraction *Superlattices Microstruct.* **126**

[26] Mukherjee S, Maitra T, Pradhan A, Mukherjee S, Manna G, Bhunia S and Nayak A 2019 Rapid responsive Mg/ZnSnP2/Sn photodetector for visible to near-infrared application *Sol. Energy Mater. Sol. Cells* **189**

[27] Dai X, Zhang S, Wang Z, Adamo G, Liu H, Huang Y, Couteau C and Soci C 2014 GaAs/AlGaAs Nanowire Photodetector

[28] Pradhan A, Mukherjee S, Maitra T, Nayak A and Bhunia S 2019 Improved spectral and temporal response of MSM photodetectors fabricated on MOCVD grown spontaneous AlGaAs superlattice *Sensors Actuators, A Phys.* **297**

[29] Bernard J E, Dandrea R G, Ferreira L G, Froyen S, Wei S H and Zunger A 1990 Ordering in semiconductor alloys *Appl. Phys. Lett.* **56** 731–3

[30] Teng D, Shen J, Newman K E and Gu B L 1991 Effects of ordering on the band structure of III-V semiconductors *J. Phys. Chem. Solids* **52** 1109–28

[31] Suzuki T, Norman A G and Stringfellow G B 2002 *Spontaneous Ordering in Semiconductor Alloys* ed A Mascarenhas (Springer Science + Business Media)

[32] Launois H, Quillic M, Glas F and Treacy M 1983 No Title *Inst. Phys. Conf. Ser.* 537

[33] Suzuki T, Hino I, Gomyo A and Nishida K 1982 MOCVD-Grown Al0 . 5In0 . 5P – Ga0 . 5In0 . 5P Double Heterostructure Lasers Optically Pumped at 90 K *Jpn. J. Appl. Phys.* **21** L731–3

[34] Asai H and Oe K 1995 Ga x In1−x P liquid phase epitaxial growth on (100) GaAs substrates **6849** 10–3

[35] Gomyo A, Suzuki T and Iijima S 1988 Observation of strong ordering in GaxIn1-xP alloy semiconductors *Phys. Rev. Lett.* **60** 2645–8

[36] Nakayama H and Fujita H 1986 No Title *Inst. Phys. Conf Ser.* 289

[37] Jen H R, Cherng M J and Stringfellow G B 1986 Ordered structures in GaAs0.5Sb0.5 alloys grown by organometallic vapor phase epitaxy *Appl. Phys. Lett.* **48** 1603–5

[38] Gomyo Akiko , Makita Kikuo , Hino Isao S T 1994 Observation of a New Ordered Phase in Al Int —As Alloy and Relation between Ordering Structure and Surface Reconstruction During Molecular-Beam-Epitaxial Growth *Phys. Rev. Lett.* **72** 673–6

[39] Gomyo Akiko , Masayoshi Sumino , Hino Isao S T 1995 Observation of a New CuPt-Type Ordered-Phase with Orientation in the [111] A Direction in *Jpn. J. Appl. Phys.* **34** L469–72

[40] Zhang S . B, Wei S H, Zunger A and Yoshida H K 1998 Defect physics of the CuInSe2 chalcopyrite semiconductor *Phys. Rev. B* **57** 9643–56

[41] Jinghua Z, Xiaohong T and Jinghua T 2009 Atomic ordering of AlInP grown by MOVPE at different temperatures in pure ambient N2 *CrystEngComm* **11** 1068–72

[42] Hisatsune K, Tanaka Y, Udoh K and Yasuda K 1995 Three stages of ordering in CuAu *Intermetallics* **3** 335–9

[43] Mikkelsen J C and Boyce J B 1982 Atomic-Scale Structure of Random Solid Solutions: Extended X-Ray-Absorption Fine-Structure Study ofGa1−xInxAs *Phys. Rev. Lett.* **49** 1412–5

[44] Suzuki T, Gomyo A, Iijima S, Kobayashi K, Kawata S, Hinon I and Yu T 1988 Band-Gap energy anomaly and sublattice ordering in GalnP and AlGalnP grown by metalorganic vapor phase epitaxy *Jpn. J. Appl. Phys.* **27** 2098–106

[45] Hildebrand J H 1929 Solubility. XII. Regular solutions *J. Am. Chem. Soc.* **51** 66–80

[46] Suzuki T, Gomyo A, Iijima S, Kobayashi K, Kawata S, Hinon I and Yu T 1988 Band-Gap energy anomaly and sublattice ordering in GalnP and AlGalnP grown by metalorganic vapor phase epitaxy *Jpn. J. Appl. Phys.* **27** 2098–106

[47] Song J D, Ok Y W, Kim J M, Lee Y T and Seong T Y 2001 Occurrence of CuPt-A and CuPt-B type ordering in GaInP layers grown by solid source molecular beam epitaxy *Appl. Surf. Sci.* **183** 33–8

[48] Ueda O, Hoshino M, Takechi M, Ozeki M, Kato T and Matsumoto T 1990 Comparative study of atomic ordering and alloy clustering in InGaP crystals grown by metalorganic vapor phase epitaxy, chloride-vapor phase epitaxy, and liquid phase epitaxy *J. Appl. Phys.* **68** 4268–71

[49] Norman A, Mallard R, Murgatroyd I, Booker R, Moore A and Scott M 1987 TED, TEM and HREM studies of atomic ordering in AlxIn1-xAs (x ~0.5) epitaxial layers grown by organometallic vapor phase epitaxy *Inst. Phys. Conf. Ser.* **87** 77–82

[50] Ueda O, Fujii T, Nakada Y, Yamada H and I. Y 1989 Tem Investigation of Modulated

Structures and Ordered Structures *J. Cryst. Growth* **95** 38–42

[51] Arent D J, Bode M, Bertness K A, Kurtz S R and Olson J M 1993 Band-gap narrowing in ordered Ga0.47In0.53As *Appl. Phys. Lett.* **62** 1806–8

[52] Shahid M A, Mahajan S and Laughlin D E 1987 Atomic ordering in Ga 0.47 In 0.53 As and Ga x In 1 − x As y P 1 − y alloy semiconductors **58**

[53] Ueda O, Nakata Y, Nakamura T and Fujii T 1991 TEM investigation of CuAu-I type ordered structures in MBE-grown InGaAs crystals on (110) InP substrates *J. Cryst. Growth* **115** 375–80

[54] Suzuki T, Ichihashi T and Tsuji M 2000 TRIPLE-PERIOD (TP)-A AND CuPt-A TYPE ORDERING IN AIo.51n0.5As GROWN BY METALORGANIC-VAPOR-PHASE-EPITAXY *Mat. Res. Soc. Symp. Proc.* **583** 267–70

[55] Shahid M A and Mahajan S 1988 Long-range atomic order in Ga x In 1 − x As y P 1 − y epitaxial layers [(x,y)=(0.47,1), (0.37,0.82), (0.34,0.71), and (0.27,0.64)] *Phys. Rev. B* **38** 1344–50

[56] Stringfellow G B 1974 Calculation of ternary and quaternary III–V phase diagrams *J. Cryst. Growth* **27** 21–34

[57] Chen A B and Sher A 1985 Semiconductor pseudobinary alloys: Bond-length relaxation and mixing enthalpies *Phys. Rev. B* **32** 3695–711

[58] Muto T and Takagi Y 1955 The Theory of Order-Disorder Transitions in Alloys *Solid State Phys. - Adv. Res. Appl.* **1** 193–282

[59] Foster L M 1974 A Lattice Parameter Criterion for Miscibility Gaps in the III-V and II-VI Pseudobinary Solid Solutions *J. Electrochem. Soc.* **121** 1662–5

[60] Chen G S, Jaw D H and Stringfellow G B 1991 Atomic ordering in GaAsP *J. Appl. Phys.*

69 4263–72

[61] Adachi S 2009 *Properties of Semiconductor Alloys: Group-IV, III–V and II–VI*

[62] Zunger A 1997 Spontaneous Atomic Ordering in Semiconductor Alloys: Causes, Carriers, and Consequences *MRS Bull.* **22** 20–6

[63] Suzuki T 1997 Bandgap anomaly, atomic ordering, and their applications *MRS Bull.* **22** 33–7

[64] Suzuki T, Ichihashi T and Nakayama T 1998 Observation of CuPt-A type atomic ordering in AlxIn1-xAs alloys *Appl. Phys. Lett.* **73** 2588–90

[65] Tirtowidjojo M and Pollard R 1988 Elementary processes and rate-limiting factors in MOVPE of GaAs *J. Cryst. Growth* **93** 108–14

[66] Jen H R, Jou M J, Cherng Y T and Stringfellow G B 1987 The kinetic aspects of ordering in GaAs1-xSbx grown by organometallic vapor phase epitaxy *J. Cryst. Growth* **85** 175–81

[67] Gomyo A, Suzuki T, Iijima S, Hotta H, Fujii H, Kawata S, Kobayashi K, Ueno Y and Hino I 1988 Nonexistence of Long-Range Order in Ga0 . 5In0 . 5P Epitaxial Layers Grown on (111) B and (110) GaAs Substrates *Jpn. J. Appl. Phys.* **27** L2370–2

[68] Stringfellow G B and Chen G S 1991 Atomic ordering in III/V semiconductor alloys *J. Vac. Sci. Technol. B Microelectron. Nanom. Struct.* **9** 2182–8

[69] Forrest R, Golding T, Moss S, Zhang Y, Geisz J, Olson J and Mascarenhas A 1998 X-ray diffraction and excitation photoluminescence analysis of ordered GaInP *Phys. Rev. B - Condens. Matter Mater. Phys.* **58** 15355–8

[70] Ernst P, Geng C, Scholz F, Schweizer H, Zhang Y and Mascarenhas A 1995 Band-gap reduction and valence-band splitting of ordered GaInP2 *Appl. Phys. Lett.* **67** 2347

[71] Wu M, Luna E, Puustinen J, Guina M and Trampert A 2014 Observation of atomic

ordering of triple-period-A and -B type in GaAsBi *Appl. Phys. Lett.* **105**

[72] Wei S H and Zunger A 1994 Optical properties of zinc-blende semiconductor alloys: Effects of epitaxial strain and atomic ordering *Phys. Rev. B* **49** 14337–51

[73] Ernst P, Geng C, Scholz F, Schweizer H, Zhang Y and Mascarenhas A 1995 Band-gap reduction and valence-band splitting of ordered GaInP2 *Appl. Phys. Lett.* **67** 2347

[74] Takanohashi T and Ozeki M 1991 Exciton-transition energies and band structure of (Gap)n(gaas)n/gaas atomic-layer superlattices *Jpn. J. Appl. Phys.* **30** 956–8

[75] Seong T Y 1991 Microstructural characterization of heteroepitaxial layers of III-V compound semiconductors *Oxford Univ. Res. Arch.*

[76] Schneider R P, Jones E D and Follstaedt D M 1994 Growth and characterization of GaInP unicompositional disorder-order- disorder quantum wells *Appl. Phys. Lett.* **65** 587–9

[77] Franceschetti A, Wei S H and Zunger A 1995 Prediction of New Fingerprints of Ordering in GaInP2 Alloys *MRS online Proc.* **417**

[78] Zhang Y and Mascarenhas A 1995 Conduction- and valence-band effective masses in spontaneously ordered GaInP2 *Phys. Rev. B* **51** 13162–73

[79] Thomas R J, Chandrasekhar H R, Chandrasekhar M, Jones E D and Schneider R P 1995 POLARIZED PHOTOMODULATED REFLECTIVITY AND PHOTOLUMINESCENCE STUDIES OF ORDERED InGaP, UNDER PRESSURE **56** 357–62

[80] Ernst P, Geng C ., Scholz F and Schweizer H 1996 Ordering in GaInP2 Studied by Optical Spectroscopy *phys. stat. sol.* **193** 213–29

[81] Driessen F A J M 1995 High-efficiency energy up-conversion at GaAs-GaInP2 interfaces *Appl. Phys. Lett.* **67** 2813

[82] Christensen N E, Wei S and Zunger A 1989 First-principles calculation of the formation energies of ordered and disordered phases of AlAs-GaAs *Phys. Rev. B* **40**

[83] Chin A, Hsieh K Y and Lin H Y 1994 Spontaneous formation of Al rich and Ga rich AlxGa1-xAs/AlyGa1-yAs superlattice and strong enhancement of optical properties *Appl. Phys. Lett.* **65** 1921–3

[84] P. M. Petroff, A. Y. Cho, F. K. Reinhart, A. C. Gossard and W W 1982 Alloy Clustering in Gal1-xAlxAsCompound Semiconductors Grown by Molecular Beam Epitaxy **48** 170–3

[85] Rudolph D, Funk S, Döblinger M, Morkötter S, Hertenberger S, Schweickert L, Becker J, Matich S, Bichler M, Spirkoska D, Zardo I, Finley J J, Abstreiter G and Koblmüller G 2013 Spontaneous alloy composition ordering in GaAs-AlGaAs core-shell nanowires *Nano Lett.* **13** 1522–7

[86] Maitra T, Pradhan A, Mukherjee S, Mukherjee S, Nayak A and Bhunia S 2019 Evaluation of spontaneous superlattice ordering in MOCVD grown AlxGa1-xAs epilayer on GaAs (100) using X-ray reflectivity and rocking curve analysis *Phys. E Low-Dimensional Syst. Nanostructures* **106**

[87] van Ijzendoorn L J, van de Walle G F A, van Gorkum A A, Theunissen A M L, van den Heuvel R A and Barrett J H 1990 Diffusion and strain relaxation in Si/Si1-xGex/Si structures studied with Rutherford backscattering spectrometry *Nucl. Inst. Methods Phys. Res. B* **50** 127–30

[88] Singh R N and Koch E F 1986 TEM Study of Interdiffusion and Interfaces in Mo/Pd/Si Thin Films *J. Electrochem. Soc.* **133** 1191–4

[89] Whitlow S J and Wool R P 1991 Diffusion of Polymers at Interfaces: A Secondary Ion Mass Spectroscopy Study *Macromolecules* **24** 5926–38

[90] Chang L L and Koma A 1976 Interdiffusion between GaAs and AlAs *Appl. Phys. Lett.* **29** 138–41

[91] Camras M D, Holonyak N, Burnham R D, Streifer W, Scifres D R, Paoli T L and Lindström C 1983 Wavelength modification of AlxGa1-xAs quantum well heterostructure lasers by layer interdiffusion *J. Appl. Phys.* **54** 5637–41

[92] Cibert J, Petroff P M, Dolan G J, Pearton S J, Gossard A C and English J H 1986 Optically detected carrier confinement to one and zero dimension in GaAs quantum well wires and boxes *Appl. Phys. Lett.* **49** 1275–7

[93] Gonzalez-Debs M, Cederberg J G, Biefeld R M and Kuech T F 2005 Photoluminescence studies on Al and Ga interdiffusion across (Al,Ga)Sb/ GaSb quantum well interfaces *J. Appl. Phys.* **97** 1–8

[94] Fleming R M, McWhan D B, Gossard A C, Wiegmann W and Logan R A 1980 X-ray diffraction study of interdiffusion and growth in (GaAs) n(AlAs)m multilayers *J. Appl. Phys.* **51** 357–63

[95] Arch D K, Faurie J P, Staudenmann J L, Hibbsbrenner M, Chow P and Zanio K 2014 Interdiffusion in HgTe–CdTe superlattices **2101**

[96] Prokes S M and Wang K L 1990 Interdiffusion measurements in asymmetrically strained SiGe/Si superlattices *Appl. Phys. Lett.* **56** 2628–30

[97] Fatah J M, Harrison P, Stirner T, Hogg J H C and Hagston W E 1998 Double crystal x-ray diffraction simulations of diffusion in semiconductor microstructures *J. Appl. Phys.* **83** 4037–41

[98] Elhadidy H, Sikula J and Franc J 2012 Symmetrical current-voltage characteristic of a metal-semiconductor-metal structure of Schottky contacts and parameter retrieval of a

CdTe structure *Semicond. Sci. Technol.* **27**

[99] Yu L S, Wang Y H, Li S S and Ho P 1992 Low dark current step-bound-to-miniband transition InGaAs/GaAs/AlGaAs multiquantum-well infrared detector *Appl. Phys. Lett.* **60** 992–4

[100] Sirtori C, Page H, Becker C and Ortiz V 2002 GaAs-AlGaAs quantum cascade lasers: Physics, technology, and prospects *IEEE J. Quantum Electron.* **38** 547–58

[101] Dhillon S S, Sirtori C, Barbieri S, De Rossi A, Calligaro M, Beere H E and Ritchie D A 2005 THz sideband generation at telecom wavelengths in a GaAs-based quantum cascade laser *Appl. Phys. Lett.* **87** 6–9

[102] Levine B F, Bethea C G, Hasnain G, Walker J and Malik R J 1988 High-detectivity D*=1.0×1010 cm √H̄ z̄/W GaAs/AlGaAs multiquantum well λ=8.3 μm infrared detector *Appl. Phys. Lett.* **53** 296–8

[103] Adachi S 1985 GaAs, AlAs, and AlxGa1−xAs: Material parameters for use in research and device applications *J. Appl. Phys.* **58**

[104] Rogalski A 2011 Recent progress in infrared detector technologies *Infrared Phys. Technol.* **54** 136–54

[105] Manasevit H M 1972 The use of metalorganics in the preparation of semiconductor materials: Growth on insulating substrates *J. Cryst. Growth* **13–14** 306–14

[106] Saxena R R, Cooper C B, Ludowise M J, Hikido S, Sardi V M and Borden P G 1981 Studies of GaAs and AlGaAs layers grown by OM-VPE *J. Cryst. Growth* **55** 58–63

[107] Leys M R and Veenvliet H 1981 A study of the growth mechanism of epitaxial GaAs as grown by the technique of metal organic vapour phase epitaxy *J. Cryst. Growth* **55** 145–53

[108] Plass C, Heinecke H, Kayser o., Luth H and BALK P 1988 A COMPARATIVE STUDY OF Ga(CH3)3, Ga(C2H5)3 AND Ga(C4H9)3 IN THE LOW PRESSURE MOCVD OF GaAs *J. Cryst. Growth* **88** 455–64

[109] Shaw D W 1975 Kinetic aspects in the vapour phase epitaxy of III-V compounds *J. Cryst. Growth* **31** 130–41

[110] Tiku S K and Biswas D 2016 *III-V integrated circuit fabrication technology* (oca Raton, Florida : CRC Press)

[111] Skinner H A 1964 Advances in Organometallic Chemistry *Advances in Organometallic Chemistry* ed F G A Stone and R West (Academic Press, New York) pp 49–114

[112] Skinner H A 1964 *in Advances in Organometallic Chemistry* ed F. Stone and R West (Academic Press, New York)

[113] Hoke W E, Lemonias P J and Korenstein R 1988 An examination of organometallic thermal stability and its relevance to low-temperature mocvd growth of hgcdte *J. Mater. Res.* **3** 329–34

[114] Donkor E 2001 *Gallium arsenide heterostructures* vol 73

[115] Furr A K 2000 *CRC Handbook of Laboratory Safety* (CRC Press)

[116] Rossnagel S M 2003 Thin film deposition with physical vapor deposition and related technologies *J. Vac. Sci. Technol. A Vacuum, Surfaces, Film.* **21** S74–87

[117] Agarwal D C, Chauhan R S, Kumar A, Kabiraj D, Singh F, Khan S A, Avasthi D K, Pivin J C, Kumar M, Ghatak J and Satyam P V. 2006 Synthesis and characterization of ZnO thin film grown by electron beam evaporation *J. Appl. Phys.* **99**

[118] Benyahia K, Benhaya A and Aida M S 2015 ZnS thin films deposition by thermal evaporation for photovoltaic applications *J. Semicond.* **36**

[119] Leng Y *Materials Characterization-Introduction to microscopic and spectroscopic methods*

[120] Nan Yao Z L W 2005 *Handbook of Microscopy for Nanotechnology*

[121] Cazaux J 2012 From the physics of secondary electron emission to image contrasts in scanning electron microscopy *J. Electron Microsc. (Tokyo).* **61** 261–84

[122] Knoll M and Ruska E 1932 Das Elektronenmikroskop.(The electron microscope.) *Z. Phys.* **78** 318–39

[123] Sanyal M K 1998 X-ray scattering studies of surfaces and interfaces *Radiat. Phys. Chem.* **51** 487–95

[124] Jenkins R and Snyder R L 1996 *Introduction to X-ray powder diffractometry* vol 138, ed J D WINEFORDNER

[125] Sternbach G and Varon J 1993 Wilhelm Konrad Roentgen: A new kind of rays *J. Emerg. Med.* **11** 743–5

[126] Pełka J B 2008 Synchrotron radiation in biology and medicine *Acta Phys. Pol. A* **114** 309–29

[127] Ansaldo E J 1977 Uses of synchrotron radiation *Contemp. Phys.* **18** 527–46

[128] Deutsch M, Förster E, Hölzer G, Härtwig J, Hämäläinen K, Kao C C, Huotari S and Diamant R 2004 X-ray spectrometry of copper: New results on an old subject *J. Res. Natl. Inst. Stand. Technol.* **109** 75–98

[129] Del Alamo J A 2011 Nanometre-scale electronics with III-V compound semiconductors *Nature* **479** 317–23

[130] Liang D, Kang Y, Huo Y, Chen Y, Cui Y and Harris J S 2013 High-efficiency nanostructured window GaAs solar cells *Nano Lett.* **13** 4850–6

[131] Spagnolo V, Scamarcio G, Schrenk W and Strasser G 2004 Influence of the band-offset on the electronic temperature of GaAs/Al(Ga)As superlattice quantum cascade lasers *Semicond. Sci. Technol.* **19**

[132] Becker C, Sirtori C, Page H, Glastre G, Ortiz V, Marcadet X, Stellmacher M and Nagle J 2000 AlAs / GaAs quantum cascade lasers based on large direct conduction band discontinuity *Appl. Phys. Lett.* **77** 463–5

[133] Vigliante A, Homma H, Zborowski J T, Golding T D and Moss S C 1999 High-resolution x-ray diffraction study of In0.25Ga0.75Sb/InAs superlattice *J Mater Res.* **14** 1744–51

[134] Sinha S K, Sirota E B, Garoff S and Stanley H B 1988 X-ray and neutron scattering from rough surfaces *Phys. Rev. B* **38** 2297–311

[135] Bartels W J, Hornstra J and Lobeek D J W 1986 X-ray diffraction of multilayers and superlattices *Acta Crystallogr. Sect. A* **42** 539–45

[136] Li J H, Stokes D W, Wickett J C, Caha O, Bassler K E, Moss S C, Li J H, Stokes D W, Wickett J C, Caha O and Bassler K E 2010 Effect of strain on the growth of InAs / GaSb superlattices : An x-ray diffraction study *J. Appl. Phys.* **107**

[137] Su D S, Neumann W, Hunger R, Schubert-Bischoff P, Giersig M, Lewerenz H J, Scheer R and Zeitler E 1998 CuAu-type ordering in epitaxial CuInS2 films *Appl. Phys. Lett.* **73** 785–7

[138] Froyen S and Zunger A 1991 Surface-induced ordering in GaInP *Phys. Rev. Lett.* **66** 2132–5

[139] Dong Y 2014 A Systematic Study of Silicon Germanium Interdiffusion for Next Generation Semiconductor Devices

[140] Shaw D 1973 *Diffusion in Semiconductors*

[141] Schick J T and Morgan C G 2011 Gallium interstitial contributions to diffusion in gallium arsenide *AIP Adv.* **1**

[142] Shaw D and Capper P 2000 Conductivity type conversion in Hg1-xCdxTe *J. Mater. Sci. Mater. Electron.* **11** 169–77

[143] Takeuchi H, Ranade P, Subramanian V and King T J 2002 Observation of dopant-mediated intermixing at Ge/Si Interface *Appl. Phys. Lett.* **80** 3706–8

[144] Rothman S J 1984 The Measurement of Tracer Diffusion Coefficients in Solids *Diffusion in Crystalline Solids* ed G E MURCH and A S NOWICK (Academic Press) pp 1–56

[145] Hüger E, Kube R, Bracht H, Stahn J, Geue T and Schmidt H 2012 A neutron reflectometry study on silicon self-diffusion at 900°C *Phys. Status Solidi Basic Res.* **249** 2108–12

[146] Fatah J M, Harrison P, Stimer T, Hogg J H C and Hagston W E 1998 Double crystal x-ray diffraction simulations of diffusion in semiconductor microstructures *J. Appl. Phys.* **83** 4037–41

[147] Strohm A, Voss T, Frank W, Laitinen P and Ra J 2002 Self-diffusion of 71 Ge and 31 Si in Si-Ge alloys *Zeitschrift für Met.* **93** 737–44

[148] Aubertine D B, Mander M A, Ozguven N, Marshall A F, McIntyre P C, Chu J O and Mooney P M 2002 Observation and modeling of the initial fast interdiffusion regime in Si/SiGe multilayers *J. Appl. Phys.* **92** 5027–35

[149] Bracht H, Haller E E, Eberl K and Cardona M 1999 Self- and interdiffusion in AlXGa1-XAs/GaAs isotope heterostructures *Appl. Phys. Lett.* **74** 49–51

[150] Warren B E 1990 *X-ray diffraction* (Dover, New York)

[151] Greer A L and Spaepen F 1985 Diffusion *Synthetic modulated structures* ed L L Chang

and B C Giesen (Academic Press, Orlando) pp 419–86

[152] Moustakas T D, Iii-nitride I, Qws A and Leds U V 2013 pss **174** 169–74

[153] Wei S H and Zunger A 1990 Band-gap narrowing in ordered and disordered semiconductor alloys *Appl. Phys. Lett.* **56** 662–4

[154] Chin A, Martin P, Ballingall J, Yu T H and Mazurowski J 1991 Comparison of high quality (111)B and (100) AlGaAs grown by molecular beam epitaxy *Appl. Phys. Lett.* **59** 2394–6

[155] Johnson J L, Samoska L A, Gossard A C, Merz J L, Jack M D, Chapman G R, Baumgratz B A, Kosai K and Johnson S M 1996 Electrical and optical properties of infrared photodiodes using the InAs/Ga1-xInxSb superlattice in heterojunctions with GaSb *J. Appl. Phys.* **80** 1116–27

[156] Yang W, Zhang F, Liu Z and Wu Z 2009 Materials Science in Semiconductor Processing Effects of annealing on the performance of 4H-SiC metal – semiconductor – metal ultraviolet photodetectors **11** 59–62

[157] Heilman R and Oelgart G 1990 Ionization energy of the carbon acceptor in AlxGa 1-xAs *Semicond. Sci. Technol.* **5** 1040–5

[158] Varshni Y P 1967 Temperature dependence of the energy gap in semiconductors *Physica* **34** 149–54

[159] Fang Y, Wang L, Sun Q, Lu T, Deng Z, Ma Z, Jiang Y, Jia H, Wang W, Zhou J and Chen H 2015 Investigation of temperature-dependent photoluminescence in multi-quantum wells *Sci. Rep.* **5** 1–7

[160] García-Sánchez F J, Lugo-Muñoz D, Muci J and Ortiz-Conde A 2013 Lumped parameter modeling of organic solar cells' S-shaped I-V characteristics *IEEE J. Photovoltaics* **3**

330–5

[161] Jain A and Kapoor A 2005 A new approach to study organic solar cell using Lambert W-function *Sol. Energy Mater. Sol. Cells* **86** 197–205

[162] Zhang H, Zhang X, Liu C, Lee S T and Jie J 2016 High-Responsivity, High-Detectivity, Ultrafast Topological Insulator Bi2Se3/Silicon Heterostructure Broadband Photodetectors *ACS Nano* **10** 5113–22

[163] Liu J M 2005 *Photonic devices* (Cambridge University Press)

[164] Jiang Y, Zhang W J, Jie J S, Meng X M, Fan X and Lee S T 2007 Photoresponse properties of CdSe single-nanoribbon photodetectors *Adv. Funct. Mater.* **17** 1795–800

[165] Katz O, Bahir G and Salzman J 2004 Persistent photocurrent and surface trapping in GaN Schottky ultraviolet detectors *Appl. Phys. Lett.* **84** 4092–4

[166] Fu L, Tan H H, McKerracher I, Wong-Leung J, Jagadish C, Vukmirović N and Harrison P 2006 Effects of rapid thermal annealing on device characteristics of InGaAs/ GaAs quantum dot infrared photodetectors *J. Appl. Phys.* **99** 1–8

[167] Singh O P, Sharma A, Gour K S, Husale S and Singh V N 2016 Fast switching response of Na-doped CZTS photodetector from visible to NIR range *Sol. Energy Mater. Sol. Cells* **157** 28–34

[168] Jin Y, Wang J, Sun B, Blakesley J C and Greenham N C 2008 Solution-processed ultraviolet photodetectors based on colloidal ZnO nanoparticles *Nano Lett.* **8** 1649–53

[169] Ling C, Guo T, Lu W, Xiong Y, Zhu L and Xue Q 2017 Ultrahigh broadband photoresponse of SnO2 nanoparticle thin film/SiO2/p-Si heterojunction *Nanoscale* **9** 8848–57

[170] Lan C, Li C, Wang S, He T, Jiao T, Wei D, Jing W, Li L and Liu Y 2016 Zener

Tunneling and Photoresponse of a WS2/Si van der Waals Heterojunction *ACS Appl. Mater. Interfaces* **8** 18375–82

[171] Gour K S, Singh O P, Bhattacharyya B, Parmar R, Husale S, Senguttuvan T D and Singh V N 2017 Enhanced photoresponse of Cu2ZnSn(S, Se)4based photodetector in visible range *J. Alloys Compd.* **694** 119–23

[172] Gour K S, Bhattacharyya B, Singh O P, Yadav A K, Husale S and Singh V N 2018 Nanostructured Cu2ZnSnS4 (CZTS) thin film for self-powered broadband photodetection *J. Alloys Compd.* **735** 285–90

[173] Stringfellow G B 2002 Effects of the Surface on CuPt Ordering During OMVPE Growth *Spontaneous Ordering in Semiconductor Alloys* ed A Mascarenhas (Springer Science + Business Media) pp 99–115

Anway_Pradhan_PHYS05201404003

By Anway Pradhan

WORD COUNT	35432	TIME SUBMITTED	25-FEB-2020 11:44AM
		PAPER ID	55863174

Study of MOCVD grown AlGaAs/GaAs (100) spontaneous superlattice and its application for optoelectronic devices

By

ANWAY PRADHAN
Enrolment No- PHYS05201404003

Saha Institute of Nuclear Physics, Kolkata

A thesis submitted to the

Board of Studies in Physical Sciences

In partial fulfillment of requirements

for the Degree of

DOCTOR OF PHILOSOPHY

of

HOMI BHABHA NATIONAL INSTITUTE

February, 2020

Anway_Pradhan_PHYS05201404003

ORIGINALITY REPORT

6%

SIMILARITY INDEX

PRIMARY SOURCES

1	sll.mntl.illinois.edu Internet	613 words — 2%
2	www.imsc.res.in Internet	238 words — 1%
3	onlinelibrary.wiley.com Internet	147 words — < 1%
4	www.formatex.info Internet	138 words — < 1%
5	www.advanced-energy.com Internet	133 words — < 1%
6	www.scribd.com Internet	124 words — < 1%
7	tel.archives-ouvertes.fr Internet	85 words — < 1%
8	cnx.org Internet	82 words — < 1%
9	repository.ntu.edu.sg Internet	68 words — < 1%
10	www.hbni.ac.in Internet	58 words — < 1%
11	archiv.ub.uni-heidelberg.de Internet	50 words — < 1%

12	phoenix.repo.nii.ac.jp Internet	42 words — < 1%
13	s3.amazonaws.com Internet	36 words — < 1%
14	wrap.warwick.ac.uk Internet	35 words — < 1%
15	www.coursehero.com Internet	33 words — < 1%
16	www.issp.ac.ru Internet	28 words — < 1%
17	core.ac.uk Internet	24 words — < 1%
18	www.strtrade.com Internet	22 words — < 1%
19	ncmn.unl.edu Internet	21 words — < 1%
20	espace.library.uq.edu.au Internet	17 words — < 1%

EXCLUDE QUOTES	ON	EXCLUDE MATCHES	OFF
EXCLUDE BIBLIOGRAPHY	ON		

Thesis Highlight

Name of the Student: Anway Pradhan

Name of the CI/OCC: Saha Institute of Nuclear Physics

Enrolment No.: PHYS05201404003

Thesis Title: Study of MOCVD grown AlGaAs/GaAs (100) spontaneous superlattice and its application for optoelectronic devices

Discipline: Physical sciences **Sub-Area of Discipline: Surface Physics and Material science**

Date of viva voce: 14.07.2020

Compound semiconductor alloys possess a wide range of optical and electronic properties and are thus important for a variety of devices with a huge scope for strain engineering also. Spontaneous atomic ordering during the epitaxial growth in III-V ternary or quaternary materials leading to a change in optical and electronic properties has attracted much attention in the last few decades. natural superlattice ordering due to periodic compositional modulation in the AlGaAs barrier layer with nominal Al fraction of 0.3 of GaAs/AlGaAs multi-quantum well (MQW) structure and AlGaAs epilayer with targeted concentration of 0.15 on (100) GaAs substrate grown by MOCVD despite the small bond length difference between AlAs and GaAs. A combination of low angle X-ray reflectivity (XRR) and high angle X-ray diffraction (XRD) measurements based on distorted-wave Born approximation (DWBA) and kinematical theory, respectively, have been employed to extract the composition and lattice parameter profile. Thermal diffusion in conjunction with real-time high-temperature XRD is employed to get the evolution of the modulated composition profile with annealing time as well as temperature. We have found the diffusion coefficient across the interface to be highly nonlinear and concentration dependent. The extracted interdiffusivity increases with temperature from 500 °C to 625 °C and decreases for further rise in temperature as the compositional contrast between the two layers reaches a critical value at higher temperatures beyond 625 °C. Furthermore, we have developed an MSM photodetector device based on the superlattice structures and showed an enhancement in performance as compared with homogeneous AlGaAs, regarding the spectral and temporal response. Under a forward bias of 1 V, maximum value of responsivity, detectivity and sensitivity, 10.133 mA/W, 7.6×1011 cmHz1/2W-1, 81.06 cm2/W, and a fast response time of 560 µs, were obtained for the device based on the superlattice structures. The presence of the superlattice barriers reduces the dark current whereas activation of the channels under illumination plays important role to enhance the photoresponse. The device based on the superlattice structures showed fast switching up to a relatively higher frequency which could be attributed to the intrinsic electric field due to the junctions formed between the consecutive layers.

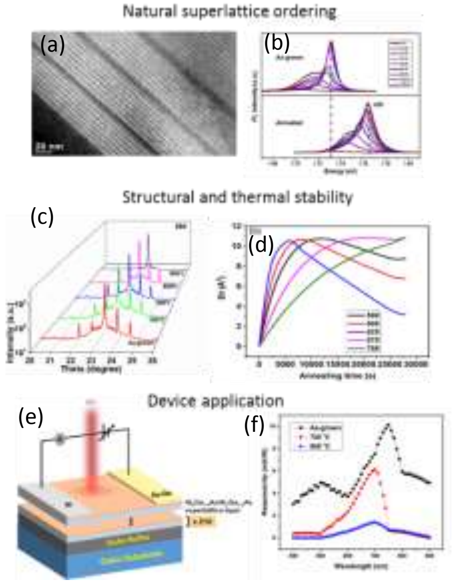

Figure 1. (a) natural superlattice ordering in AlGaAs/GaAs MQW (b) temperature dependent PL spectra for the as-grown and annealed sample (c) thermal stability of the superlattice (d) interdiffusion characteristics at five different temperatures (e) device structure (f) spectral response of the three devices